

# Analysis of Outgoing Particle Kinematics from Monte Carlo Simulations of Neutron Interactions on Hydrocarbon

A Dissertation Presented

by

**Kuunal Kelash Mahtani**

to

The Department of Physics & Astronomy

in Partial Fulfillment of the Requirements

for the Degree of

**Master of Arts**

in

**Physics**



**Stony Brook**  
**University**

May 2023

**Stony Brook University**

The Department of Physics and Astronomy

**Kuunal Kelash Mahtani<sup>1</sup>**

Thesis Defense Committee:

Chang Kee Jung<sup>2</sup> – Advisor

SUNY Distinguished Professor and Chair, Department of Physics and Astronomy

Ciro Riccio<sup>3</sup> – Advisor

Post-Doctorate Researcher, Department of Physics and Astronomy

Cyrus Dreyer<sup>4</sup> – Chairperson of Defense

Professor, Department of Physics and Astronomy

Clark McGrew<sup>5</sup>

Professor, Department of Physics and Astronomy

---

<sup>1</sup>kuunal.mahtani@stonybrook.edu

<sup>2</sup>chang.jung@stonybrook.edu

<sup>3</sup>ciro.riccio@stonybrook.edu

<sup>4</sup>cyrus.dreyer@stonybrook.edu

<sup>5</sup>clark.mcgrew@stonybrook.edu

# Abstract

Improvements of (anti-)neutrino energy reconstruction are imperative towards a deeper understanding of neutrino oscillations investigated by long-baseline (LBL) neutrino oscillation experiments. Currently, detectors of LBL experiments miss neutrons (products of anti-neutrino interactions with protons), therefore to better understand (anti-)neutrino energy reconstruction, we need to better understand neutron energy reconstruction. We present an investigation into understanding kinematics of outgoing particles from simulations of neutron interactions on a detector prototype comprised of hydrocarbon material, using analyses on a hydrogen and carbon target separately to better understand features of neutron interactions on hydrocarbon. We show that our analyses on these targets reflect expected theory-motivated features. We show a purity analysis of single-track events selected from simulations and illustrate that protons from hadronic interactions dominantly contribute to maximum energy deposition for single-track events. Conclusions and future work are discussed as well.

# Contents

|          |   |           |
|----------|---|-----------|
| <b>1</b> | <b>Introduction</b>                               | <b>7</b>  |
| <b>2</b> | <b>Experimental Setup</b>                         | <b>12</b> |
| 2.1      | SuperFGD Prototype . . . . .                      | 12        |
| 2.2      | LANL Beam Test . . . . .                          | 12        |
| <b>3</b> | <b>Neutron Interactions with Matter</b>           | <b>15</b> |
| 3.1      | Neutron Interactions on Hydrogen . . . . .        | 15        |
| 3.1.1    | Elastic Scattering . . . . .                      | 15        |
| 3.1.2    | Theoretical Cross Section Distributions . . . . . | 16        |
| 3.1.3    | Inelastic Scattering . . . . .                    | 18        |
| 3.1.4    | Theoretical Cross Section Distributions . . . . . | 19        |
| 3.2      | Neutron Interactions on Carbon . . . . .          | 20        |
| 3.2.1    | Elastic Scattering . . . . .                      | 20        |
| 3.2.2    | Theoretical Cross Section Distributions . . . . . | 20        |
| 3.2.3    | Inelastic Scattering . . . . .                    | 21        |
| 3.2.4    | Theoretical Cross Section Distributions . . . . . | 21        |
| <b>4</b> | <b>Monte Carlo Studies</b>                        | <b>23</b> |
| 4.1      | Monte Carlo Simulation . . . . .                  | 23        |
| 4.2      | Event Selection . . . . .                         | 24        |
| 4.3      | Elastic Scattering . . . . .                      | 27        |
| 4.4      | Inelastic Scattering . . . . .                    | 36        |
| 4.5      | Model Comparisons . . . . .                       | 52        |
| <b>5</b> | <b>Single-Track Event Selection</b>               | <b>67</b> |
| 5.1      | LANL Software . . . . .                           | 67        |
| 5.1.1    | Monte Carlo Reduction . . . . .                   | 67        |
| 5.1.2    | Monte Carlo Restructure . . . . .                 | 68        |
| 5.2      | Single-Track Event Selection . . . . .            | 69        |
| 5.3      | Purity Analysis . . . . .                         | 71        |
| <b>6</b> | <b>Future Work &amp; Conclusions</b>              | <b>74</b> |
| 6.1      | Improvements to Methodology . . . . .             | 74        |
| 6.2      | Comparisons to Data . . . . .                     | 74        |
| 6.3      | Code Robustness . . . . .                         | 75        |
| 6.4      | Final Remarks . . . . .                           | 76        |

## Appendices

---

|  |           |
|--|-----------|
| <b>A Additional Tables</b>   | <b>79</b> |
| <b>B Proofs</b>  | <b>81</b> |
| B.1 Classical calculation for angle between two masses of similar masses               | 81        |
| B.2 Maximum angle between carbon and neutron from elastic neutron scattering . . . . . | 82        |
| <b>C Additional Plots</b>  | <b>84</b> |
| <b>Bibliography</b>  | <b>97</b> |

# Acknowledgements

I would like to thank Professor Chang Kee Jung and Dr. Ciro Riccio, for providing me with endless opportunity to grow and to learn. I could not have been any luckier than to have had the privilege of working with the Neutrino and Nucleon (NN) group under their guidance, and have grown tremendously as a researcher and as a person over the last year thanks to their mentorship. Being able to work on the SuperFGD assembly as a masters student has been a once-in-a-lifetime opportunity and was one of the greatest experiences I have ever been a part of. I am excited to continue my academic career in high energy experimental particle physics research with the NN group for my PhD, and can't wait to improve even further beyond where I have already reached.

I would like to thank all the members of my dissertation committee (Professor Chang Kee Jung, Dr. Ciro Riccio, Professor Cyrus Dreyer, and Professor Clark McGrew) for taking time to serve on my committee and assess my thesis defense.

I would like to thank all the members of the T2K collaboration and of the NN group for helping me develop as a physicist, for answering my questions with eagerness to share knowledge, and for sharing laughs at soccer matches and barbeques.

I would like to especially thank my family; my parents - Kelash Harkishindas Mahtani and Meena Kelash Mahtani - who have given their entire lives to see their children succeed, and my sisters - Nashin Kelash Mahtani and Chandni Kelash Mahtani - who have inspired me to work hard, to chase my dreams, and to never give up. You made me the person I am today, and I will do everything in my power to use the unrelenting torrent of love you have poured into me to be the best physicist and the best person I can be.

I would like to thank Alex Goutsev, Kaitlyn Liang, Jin Sing Sia, Jack Schnieders, Lili Zong, Anna Xiang, and Tresa LeBlanc-Doucet for their constant support and love. You have brought me out of my darkest hours and have celebrated with me in the light, and I hope to someday be able to repay the kindness you have extended to me. I would also like to thank these people for helping me proofread my emails. I would like to thank my friends, too many of whom are to name, for their continued support of my dreams and ambitions.

I would like to thank my previous research advisors, Professor Robert Orr, Professor Pekka Sinervo, Professor Ue-Li Pen, and Dr. Jing Luo for introducing me to the wonders and joys of experimental HEP research, and for fostering my interest in the pursuit of an academic career.

I would like to thank Yugo Kanno, Yuriko Mori, and Kenshi Yonezu for their excellent musical compositions which have given me the strength to power through

tireless nights of data analysis and thesis writing.

I would like to humbly thank the unshakable pillars of support from all the people who made me into the person I am today. I'm never gonna give you up, never gonna let you down.

# Chapter 1

## Introduction

The T2K (Tokai to Kamioka) experiment is a long-baseline neutrino oscillation experiment based in Japan [1]. Its goal is to measure the parameters of the Pontecorvo-Maki-Nakagawa-Sakata (PMNS) matrix, in particular the mixing angles  $\theta_{23}$ ,  $\theta_{13}$  and the Charge-Parity (CP) phase  $\delta_{CP}$ , and the mass square splitting entering neutrino oscillation probabilities. The T2K neutrino beam is produced from protons of 30 GeV that impinge on a graphite target. The charged hadrons are deflected by three magnetic horns in order to select hadrons of the desired charge to make a neutrino or antineutrino beam. The properties of the beam are studied by a near detector complex located 280 m away from the target that consists of two detectors: INGRID and ND280. INGRID measures the beam direction and profile, while ND280 measures the flux and cross-sections. The far detector is Super-Kamiokande which is located 295 km from the beam source [2]. Given that neutrino oscillations depend on neutrino energy, it is very important to precisely measure the latter. There are two ways to estimate the neutrino energy: first, we can sum the final state energy of all products of neutrino interactions, however we are unable to do this as we have particles that are hard to reconstruct and we do not detect some outgoing products. Second, we can reconstruct the energy using the kinematics of the outgoing particles. The latter is the method used in the T2K experiment given that the far detector uses the Cherenkov effect to reconstruct and identify particles. At T2K energies the main interaction channel is the Charged-Current Quasi-Elastic (CCQE) interaction, where a neutrino exchanges a  $W^\pm$  boson with a neutron giving a muon and a proton in the final state, as shown in Fig. 1.1.



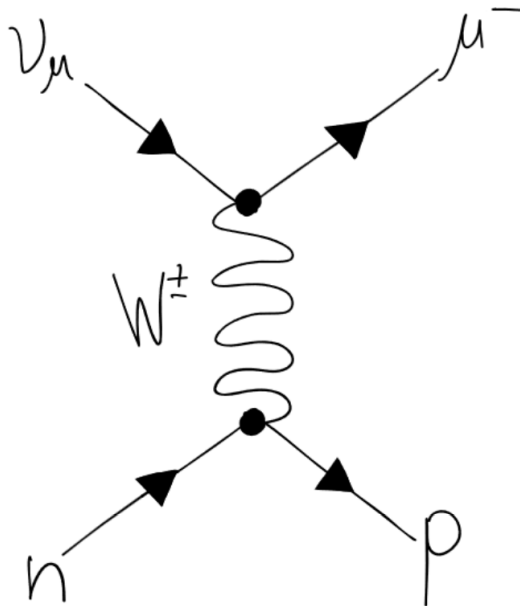


Figure 1.1. Feynman diagram of neutrino Charged-Current Quasi-Elastic interactions (CCQE); a neutrino interacts with a proton via the  $W^\pm$  to produce an outgoing negatively charged muon and neutron.

In antineutrino CCQE interactions with a proton there is a  $\mu^+$  and a neutron in the final state. Currently, understanding of antineutrino energy reconstruction at T2K is limited since our detectors do not detect neutrons nor measure their kinematics. Outgoing neutrons of CCQE interactions travel through the detector material and can interact with the detector material via hadronic interactions. In principle, we could detect outgoing charged particles from these hadronic interactions using a detector with fine granularity. A good timing resolution could allow for the measurement of neutron kinematics using the Time-of-Flight (ToF) technique.

The Super Fine Grain Detector (SuperFGD) is a 3D-projection scintillator tracker introduced to improve our knowledge on neutrino interactions. It improves reconstruction capabilities over its predecessor: the Fine Grain Detector (FGD), as the FGD was constructed using scintillation bars, and therefore it is possible to miss particles that move entirely within one bar. It will be installed in the upgraded ND280. It comprises of  $1 \text{ cm}^3$  cubes of scintillation material (1.5% PTP and 0.001% POPOP doped polystyrene), an illustration of which can be seen in Fig. 1.2. It contains a  $192 \times 56 \times 184$  (width  $\times$  height  $\times$  length) arrangement of cubes. The scintillation material is entirely comprised of hydrocarbon, and each cube is optically isolated and has 3 orthogonal wavelength shifting fibers (WLS) passing through holes of 1.5 mm on each face<sup>1</sup>. An image of the assembled SuperFGD detector is presented in Fig. 1.3. Each time a charged particle passes through a cube, scintillation light is emitted and trapped within the cube due to the optical isolation, until it hits a WLS fiber - at which point the light signal travels down the WLS fiber to Multi-Pixel Photon Counters (MPPC), wherein the signal is sent to readout electronics and converted into an electrical signal. MPPCs are located on 3 faces of the detector.

<sup>1</sup>It is possible for particles to interact with air molecules inside the cavities through which the WLS fibers are fed, and in fact we include some air into our simulations.

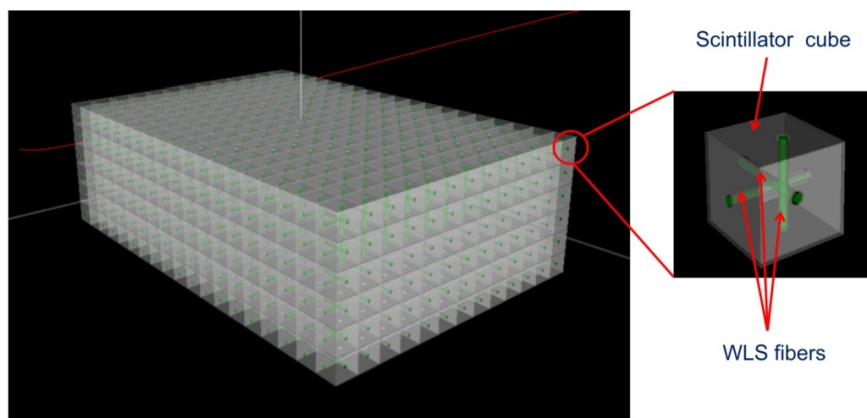


Figure 1.2. Diagram of SuperFGD, constructed from  $1\text{ cm}^3$  cubes of scintillator material with orthogonal wavelength shifting fibers going through each cube. Each hole is 1.5mm in diameter, and each WLS fiber is 1mm in diameter.

SuperFGD construction proceeded at JPARC in collaboration with members from multiple institutions including Stony Brook University starting from end of October 2022. Fishing lines with diameters of 1.0-1.4 mm were threaded through the cubes in place of WLS fibers for cube assembly, in order to hold the cubes in place and ensure proper alignment. Fishing lines were threaded through both horizontal directions first, creating 56 layers of  $192 \times 184$  cubes as seen in Fig. 1.4, stacked on top of each other one at a time. In between the installation of every 2 layers, metal rods were placed through the holes of the cubes in the vertical direction to ensure cube alignment as can be seen in Fig. 1.3. The WLS fibers were installed into the detector after cube assembly and alignment had been completed, and the detector closed in its mechanical box. Afterward, the WLS fibers, MPPC boards, calibration system, and black foam to reduce light leak were installed as well. Currently, tests on the data acquisition system are ongoing.

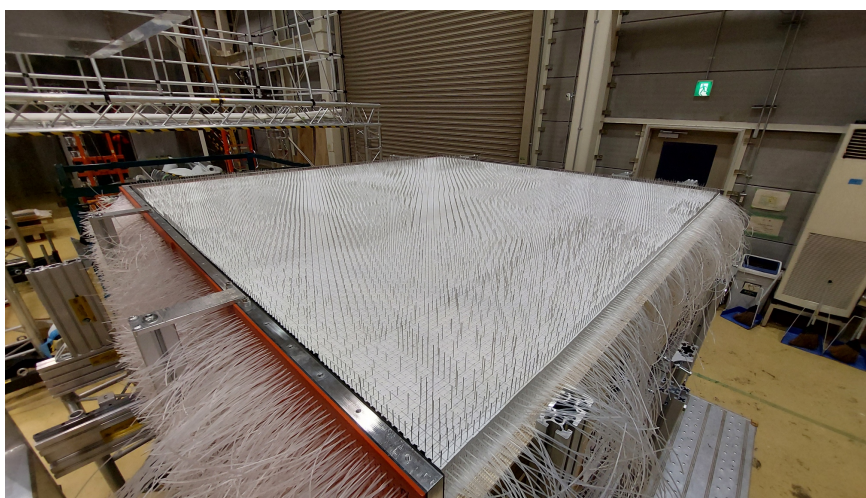


Figure 1.3. Photo of the constructed SuperFGD prior to fiber insertion. Constructed from 2 million  $1\text{ cm}^3$  cubes of scintillator material.

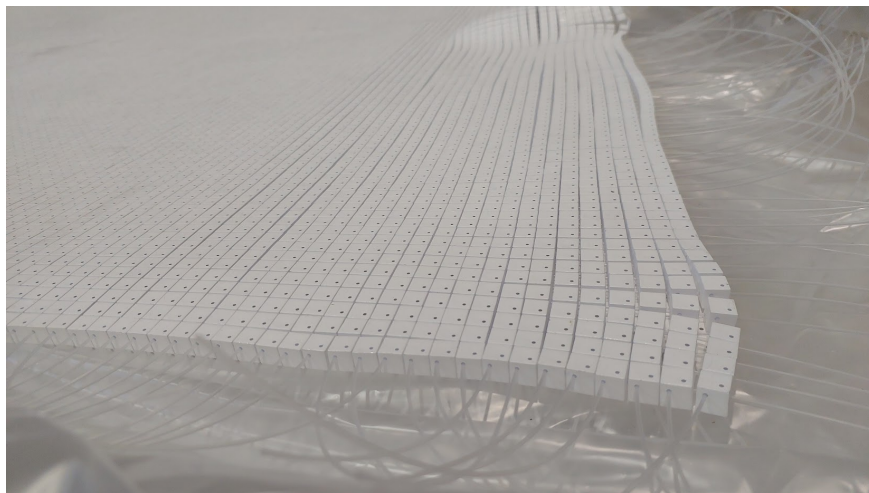


Figure 1.4. Photo of one layer of scintillation cubes with fishing line threaded through holes on the horizontal axis.

Two prototypes have been constructed to prove SuperFGD technology and study the detector performances: the SuperFGD and the US-Japan (US-JP) prototypes. This thesis will focus on the SuperFGD prototype and in particular its capabilities to detect neutrons. In this work we show the analysis on simulations of neutron interactions on hydrocarbon (CH), as was experimentally set up. Kinematics analysis for outgoing particles from hadronic interactions of a neutron beam on a CH target were conducted on simulations constructed using different cascade models (referred to as the BERTINI, BERTINI HP, and INCLXX physics lists). In particular, our focus was on the first hadronic inelastic and elastic interactions of neutrons on the CH target and the subsequent outgoing particles from the vertex of interaction. The kinetic energy, momentum,  $\cos \theta$ ,  $\theta$  (angle relative to beam), and multiplicity were constructed for all outgoing particles and organized by particle type: protons, neutrons, carbons ( $^{12}\text{C}$ ) and others for outgoing particles from elastic collisions and protons, neutrons, gammas ( $\gamma$ ), charged pions ( $\pi^+$  and  $\pi^-$ ), alphas ( $\alpha$ ), deuterons ( $D$ ), Helium 3 ( $He3$ ), isotopes of carbon ( $C^8, \dots, C^{13}$ ) and others for outgoing particles from inelastic collisions. Moreover, these distributions were constructed and organized for outgoing particles by interaction type as well. Stacked histograms of the results are presented in Section 4.2.

The SuperFGD prototype and the total neutron cross-section measurement are presented in Section 2.1. A detailed explanation of the experimental setup is presented in Section 2.2. As the motivation for studying neutron energy reconstruction has been discussed in Chapter 1, a theoretical background for predicted results from kinematics analyses of neutron interactions on CH are discussed in Chapter 3, focusing separately on features of kinematics from neutron scattering on hydrogen (Section 3.1) and carbon (Section 3.2).

We provide a thorough description of the simulations of neutron interactions in Chapter 4, after which Section 4.1 illustrates the results of the kinematic analyses. We discuss features present in analyses of neutron beams on a hydrogen and carbon target separately, and compare them to our expectations discussed in Chapter 3. We combine these analyses to understand the structures present

in outgoing particle kinematics from neutron interactions on CH. These analyses are conducted over simulations created using the BERTINI cascade model, and a comparison of analyses on simulations constructed using different cascade models are explored in Section 4.5.

Additionally, investigations into the selection of events containing a single track from simulations are explored in Chapter 5. Comparisons between single-track events from simulations and reconstructed single-track events are discussed. A purity analysis on the composition by particle type, interaction process, and interaction type of particles with highest energy deposition in single-track events are presented in Section 5.3. Further investigations, improvements of code robustness, and comparison of the simulation with data are suggested in Chapter 6. Conclusions are presented in Section 6.3, followed by references and an appendix containing tables and plots of interest to the thesis.

# Chapter 2

## Experimental Setup

### 2.1 SuperFGD Prototype

As mentioned in Chapter 1, two prototypes have been constructed to prove SuperFGD technology and study the detector performances: the SuperFGD prototype and the US-Japan (US-JP) prototype. The SuperFGD prototype consists of a  $24 \times 8 \times 48$  arrangement of cubes, and was assembled at CERN. WLS fibers throughout the cube sent signals to MPPCs to produce three orthogonal views in the  $XY$ ,  $XZ$  and  $YZ$  planes. The prototype is constructed similarly to the SuperFGD but at a smaller scale; each of the cubes used in the prototype are constructed identically to those used in the full-sized detector.

Information from 2 readout views can help determine each event (particle interaction in matter) with a precision relative to cube size, while information from a third view helps to resolve multiple track-caused ambiguities. Subsequently, the data is read out as 3 two-dimensional views, which when combined provide a pseudo 3D view of each event. As will be covered in the following section, exposing the detector prototype to a neutron and gamma beam allows us to measure the kinetic energy of outgoing neutrons by using the ToF technique.

### 2.2 LANL Beam Test

Measurements of the total neutron cross section were conducted at the Los Alamos National Lab (LANL) Weapons Neutron Research (WNR) facility using the SuperFGD prototype in 2019 and 2020. Improvements to the measurements of neutron cross section were shown for energies between 500 MeV and 688 MeV. The total neutron cross section was obtained as a function of the neutron kinetic energy, where the energy-integrated cross section for 98-688 MeV was determined to be  $0.36 \pm 0.05$  barn with a  $\chi^2/\text{d.o.f.}$  of 22.03/38. This result is consistent with existing neutron-carbon total cross section measurements while showing some contribution from neutron-hydrogen interactions [3]. This work did not only prove the capability of SuperFGD to measure neutron kinematics using the ToF technique but was also the first physics result with this technology. More data was taken in a second campaign in 2020, employing also the US-JP prototype, and is currently being analyzed.

The beamline setup at LANL consists of several main parts and is illustrated in

Figure 2.1. The SuperFGD prototype was oriented such that the neutron beam was parallel to longest dimension of the detector (z-direction, 48 cm). Firstly, a proton beam impinges onto a tungsten target with a segmented beam structure: 675  $\mu\text{s}$  pulses of protons are sent 8.33 ms apart from each other, with each macropulse containing micropulses of  $7 \times 10^6$  protons width of the order of ns, separated by 1.8  $\mu\text{s}$ , each. Data acquisition starts at the beginning of each macropulse, though the amplitude ramps up to a maximum as the macropulse starts.

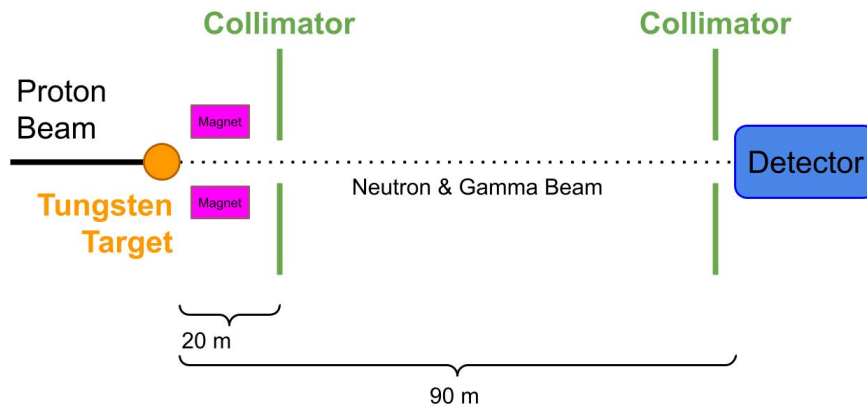


Figure 2.1. Diagram illustrating the beamline setup at LANL; a proton beam fires at a tungsten target to produce neutrons and gammas, which are sent to the detector.

Protons interact with the tungsten target at a time  $T_0$  and produce several outgoing particles, where all charged particles are deflected from the beam line using magnets and non-charged particles are fed through an aperture. As a result, the outgoing beam consists entirely of neutral particles such as neutrons and gammas which travel to the detector. Only neutrons and gammas arrive at the detector, as all other neutral particles decay before reaching the detector. The gammas will always arrive before the neutron and produce a sharp signal followed by a broader signal from the proceeding neutron, as can be seen in the event time distribution with respect to  $T_0$  in Fig. 2.2. Consequently, the arrival time of the neutron relative to the gamma is used to determine the neutron kinematics via the ToF technique. However, there are both low-energy and high-energy neutrons in each neutron and gamma, and low-energy neutrons can move slowly enough relative to succeeding neutrons and gammas such that high-energy neutrons can interfere with the signal of lagging low-energy neutrons.

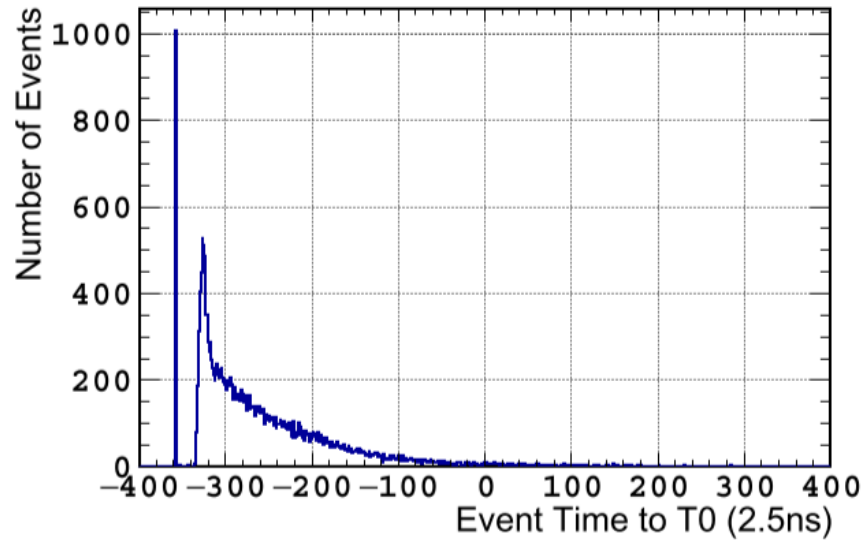


Figure 2.2. Time event distribution of detection. The sharp initial peak is the signal from the gamma, while the second, broader peak is the signal from the proceeding neutron. Figure taken from [3].

This interference was prevalent when the flight path length was set to 90m (the farthest distance from the tungsten target available at WNR) in order to improve the resolution of highest energy neutrons. Finally, two collimators are placed at distances of 20m downstream from the tungsten target and 1 m upstream of the detector to shape the neutron beam profile.

By selecting events in the neutron peak and measuring the neutron peak with respect to the gamma peak (also referred to as the gamma flash), one can determine the energy of the neutron. We require a minimum neutron energy of 13 MeV to be able to ignore the effects of low-energy neutrons interfering with high-energy neutrons.

# Chapter 3

## Neutron Interactions with Matter

There are two interaction mechanisms that can take place in neutron interactions on CH in the energy range of interest for this work: hadronic inelastic and elastic scattering. In order to understand results from analyses of neutron interactions on hydrocarbon, we will first consider separately neutron interactions on a target comprised entirely of hydrogen (free protons), and neutron interactions on a target comprised entirely of carbon. The features of the kinematics of neutron interactions on hydrocarbon will follow as the sum of the features of neutron interactions on carbon and hydrogen, naturally.

For the purposes of investigating neutron kinematics better, we will only be considering the outgoing particles from the first hadronic interaction of incoming neutrons with the target. In the data analysis Chapter 4, this means if we have an event where a given neutron does not interact with the target, we disregard this event. Non-hadronic neutron interactions on the target are not considered, though they do occur as can be seen in Fig. C.1 in the appendix.

### 3.1 Neutron Interactions on Hydrogen

#### 3.1.1 Elastic Scattering

Elastic scattering processes are more simple to follow, and hence will be considered first. The neutron mass is taken to be 939 MeV, while the proton mass is taken to be 938 MeV. If we recall classical kinematics, we recall using energy conservation that the angle between two bodies of similar mass colliding elastically is  $\phi \approx 90^\circ$  (as seen in Appendix B.1), given by the following relationship:

$$\phi = \arccos \left( \frac{|\vec{v}_2| \left( \frac{m_2}{m_1} - 1 \right)}{2|\vec{v}_1|} \right) \quad (3.1)$$

where  $m_2$  is the mass of the outgoing particle initially at rest (in this case a free proton),  $m_1$  is the mass of the incident particle (neutron) and  $\vec{v}_2$  and  $\vec{v}_1$  are the velocities of these outgoing particles, respectively. Therefore we should expect that angle between the outgoing proton and neutron should be  $\sim 90^\circ$ . This implies we should not observe either particle with a  $\theta$  (angle with respect to the beam) greater than  $90^\circ$ , since that would imply one of the outgoing particles is moving backwards as a result of the collision.



We can use classical kinematics to determine the fractional energy lost by neutron interaction with matter as seen in Reference [4], and from that deduce the maximum energy transfer from the neutron to the proton ( $Q_{Max}$ ). Eq. (3.2) shows that the fractional energy lost depends on the scattering angle of the recoil nucleus w.r.t. beam ( $\beta$ ).

$$Q = \frac{4m_1m_2}{(m_1 + m_2)^2} \cos^2(\beta) \quad (3.2)$$

where  $m_1$  and  $m_2$  are the masses of two particles involved in the scattering. We find  $Q_{Max}$  by setting  $\cos(\beta) = 1$  in Eq. (3.2).

$$Q_{Max} = \frac{4m_1m_2E}{(m_1 + m_2)^2} \quad (3.3)$$

We can see that for incoming neutrons with energy  $E$  elastically scattering off of free protons,  $Q_{Max} = 0.99E$ . Therefore, we expect to see protons with energies ranging from 0 MeV to near 800 MeV, and likewise for outgoing neutrons due to conservation of energy.

### 3.1.2 Theoretical Cross Section Distributions

By observing cross-section distributions as functions of different kinematics for elastic scattering of neutrons on free hydrogen, we may view some features we would expect to see later in our analyses. In example, Fig. 3.1 illustrates the cross section as a function of angle with respect to the beam ( $\theta$ ) for neutron elastic scattering on free hydrogen using data taken from the Evaluated Nuclear Data File (ENDF) Database [5]. Firstly, it is clear that the cross section as a function of angle changes as a function of energy, with each line on the plot in a different colour representing different energies of the incident neutrons. Notably, there is a dip in the cross section distribution which changes in magnitude and position depending on the energy of the incident neutron - i.e. the trough of the dip structure occurs at  $\sim 45^\circ$  with a cross section of  $\sim 10^{-2}$  barns for incident neutrons with 100 MeV, whereas for incident neutrons with 800 MeV the trough of the dip structure occurs at  $\sim 54^\circ$  with a cross section of about  $10^{-3}$  barns. Therefore, we should expect to see a similar dip between  $40^\circ - 60^\circ$  in  $\theta$  distributions of neutron interactions on free hydrogen. Note also that the cross sections at smaller angles are greater than they are at larger angles for all incoming neutron energies; hence we would expect to see more outgoing neutrons with smaller  $\theta$  than larger  $\theta$ .

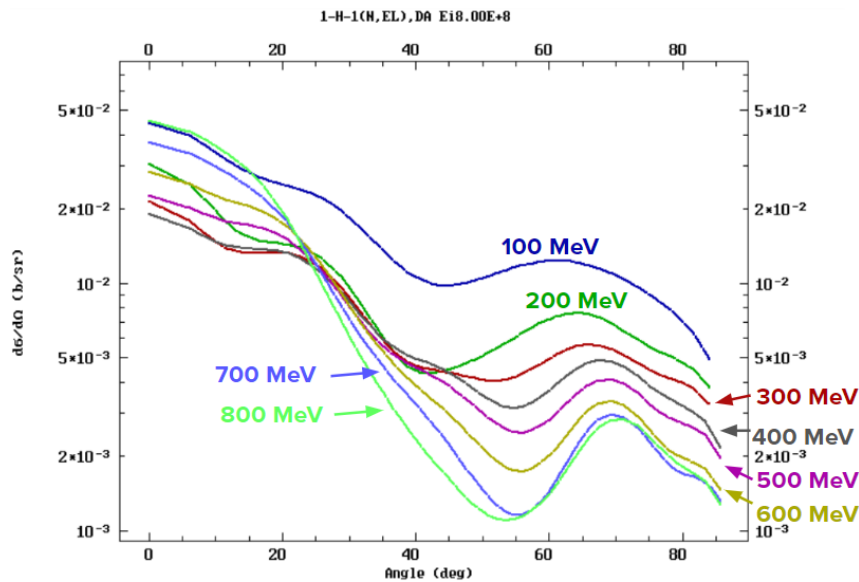


Figure 3.1. Cross section distribution of neutron interactions on free hydrogen as a function of angle [5].

If we consider the cross section as a function of energy for neutron elastic scattering with hydrogen between 1 MeV - 800 MeV as seen in Fig. 3.2<sup>1</sup>, we see a generally decreasing cross section as incident neutron energy increases. Note that this plot uses a logarithmic scale for both the x- and y- axes, and hence the slow decrease shows as a rather sharp drop when plotted on a linear scale. We would expect the distribution of the kinetic energy and momenta of outgoing neutrons to agree with this sharp drop in cross section at low MeV, followed by a steadily decreasing cross section for higher energies, approximately greater than 100 MeV.

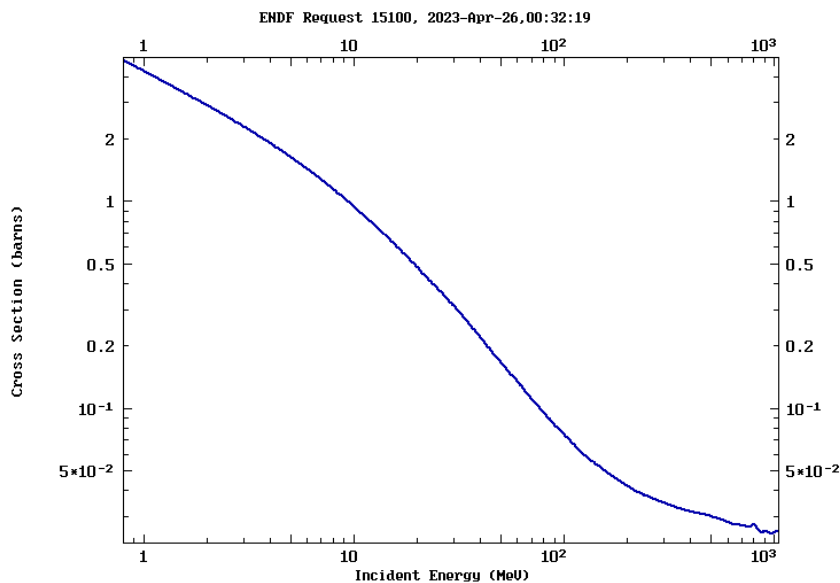


Figure 3.2. Cross section as a function of incident neutron kinetic energy for elastic scattering on free hydrogen [5]

<sup>1</sup>There is a massive collection of data from 0-1 MeV in the ENDF, which if included doesn't provide more information for how we see the cross section greater than 1 MeV, but rather takes away our attention, hence the 0-1 MeV range was not included in our consideration.

### 3.1.3 Inelastic Scattering

Inelastic scattering of neutrons on free protons is a source of pion production. Let us consider the following interaction channels:

1.  $n + p \rightarrow n + n + \pi^+$
2.  $n + p \rightarrow p + p + \pi^-$
3.  $n + p \rightarrow D + \pi^0$
4.  $n + p \rightarrow n + p + \pi^0$

We can compute the energy threshold required to produce the outgoing particles in these 4 interaction channels as follows:

$$E_{Threshold} = \frac{(\sum_{i=0} m_i c^2)^2 - (\sum_{j=0} m_j c^2)^2}{2m_n c^2} \quad (3.4)$$

where  $i \in$  incident particle & target,  $j \in$  products, and  $m_n$  is the neutron mass (incident particle). Using Eq. (3.4), we see that the aforementioned interaction channels have the following minimum energies for the incident neutron:

1.  $\approx 290$  MeV
2.  $\approx 286$  MeV
3.  $\approx 275$  MeV
4.  $\approx 279$  MeV

So, given that we have incoming neutron energies from 10 MeV - 800 MeV<sup>2</sup>, we should expect to see pion production from inelastic neutron scattering on free hydrogen, beginning at incident neutron energies of about 275 MeV. However, this assumes that the products are produced at rest and incident neutrons will require higher energies to produce products not at rest. This limits our ability to analyze some events, since the toolkit used to simulate particle interactions in matter requires the products have some minimum energy and not be at rest in order to track them. This will be expanded upon in Chapter 4.

Furthermore, we are able to use data from the ENDF to determine the integrated cross sections from 0-800 MeV for  $\pi^+$ ,  $\pi^-$  and  $\pi^0$  production from inelastic neutron collisions with hydrogen, as well as the integrated cross section for all inelastic collisions of neutrons on hydrogen for our energy range. These results are presented in Table I. Note that the sum of the total integrated cross sections from pion production is  $\sim 2.702$  barns, so we expect that these collisions will dominantly feature pion production. We also expect neutral pion production to be  $\sim 30\%$  greater than charged pion production. If we only have the interaction channels proposed above, we expect an equal number of outgoing neutrons and protons.

<sup>2</sup>The shape of the distribution in the 0-10MeV range provided by the ENDF is very different from the shape of the distribution from 10 MeV - 800 MeV. The shape of the 0-10MeV range is not significant for the exploration of this thesis, hence was not included in this section as it would distract from the shape of the distribution from 10 MeV - 800 MeV

TABLE I. Integrated cross section calculation from 0-800MeV for outgoing particles from inelastic neutron scattering on hydrogen.

| Particle Type | Integrated Cross Section for 0-800 MeV |
|---------------|--|
| $\pi^+$       | 0.511 barns                            |
| $\pi^-$       | 0.515 barns                            |
| $\pi^0$       | 1.676 barns                            |
| Total         | 2.709 barns                            |

### 3.1.4 Theoretical Cross Section Distributions

If we consider the cross section as a function of neutron incoming energy for inelastic scattering with hydrogen between 10-800 MeV<sup>3</sup> as seen in Fig. 3.3, we see a low and gradual decrease in cross section until  $\approx 275$  MeV, at which point we observe a dramatic increase. This is coherent with the minimum threshold energies calculated in the aforementioned interaction channels for inelastic scattering of neutrons on hydrogen, and we should expect a similarly shaped result on the analyses of the MC files. Note that the largest cross section value for Fig. 3.3 is on the order of  $\times 10^{-2}$  barns - about 2 orders of magnitude lower than the other cross sections we consider in this chapter. Hence, we expect that neutron inelastic scattering off hydrogen is not a significant contributor to inelastic interactions of neutron on CH.

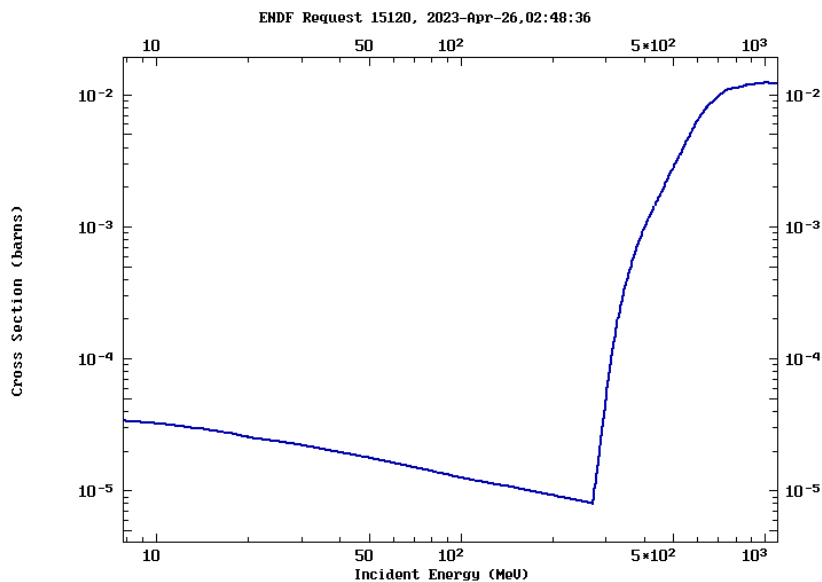


Figure 3.3. Cross section as a function of incident neutron kinetic energy for inelastic scattering on hydrogen [5].

<sup>3</sup>The shape of the distribution in the 0-10 MeV range provided by the ENDF is unremarkable and is not significant for the purpose of this investigation, hence was not included in this section as it would distract from the shape of the distribution from 10-800 MeV

## 3.2 Neutron Interactions on Carbon

### 3.2.1 Elastic Scattering

Using Eq. (3.4), we can determine that the maximum energy transfer from a neutron to  $^{12}\text{C}$  is  $Q_{Max} \approx 0.28E$ , meaning that since the highest energy of our incoming neutrons is 800 MeV, we should not expect to see outgoing carbons with kinetic energies higher than  $\sim 227$  MeV. If we use Eq. (3.1) and conservation of energy to determine the angle between the outgoing neutron and outgoing carbon from an inelastic collision of neutron on  $^{12}\text{C}$ , we see that the angle between the outgoing particles must be at least  $\sim 90^\circ$  and can be at most  $\phi \sim 148^\circ$ . These calculations are given in Appendix B.2, where we assume maximum energy transfer to the carbon. However, as we reduce the energy transferred from the neutron to the carbon we find that the range of possible angles approaches  $\phi \in [90, 180)$ . This calculation was performed using the mass of  $^{12}\text{C}$ , so we note that the maximum  $\phi$  obtainable (from 800 MeV incident neutron scattering and maximum energy transfer) is  $\sim 131^\circ$  for  $\text{C}^8$  and is  $\sim 151^\circ$  for  $\text{C}^{13}$ . This means we should not be surprised to see  $\theta \in [0^\circ, 180^\circ)$  (angle w.r.t. beam) in our analysis, and given the masses of  $^{12}\text{C}$  and a neutron are very different it makes sense that we have some of the outgoing neutrons moving backward after the collision.

### 3.2.2 Theoretical Cross Section Distributions

Similarly to the case of elastic scattering of neutrons off hydrogen, we can note that the cross section distribution for elastic scattering of neutrons off carbon as a function of angle relative to the beam changes as a function of energy. However, now we have  $\theta \in [0^\circ, 180^\circ]$  and no dip as we have seen before. We do however note the larger cross section at lower angles than at higher angles.

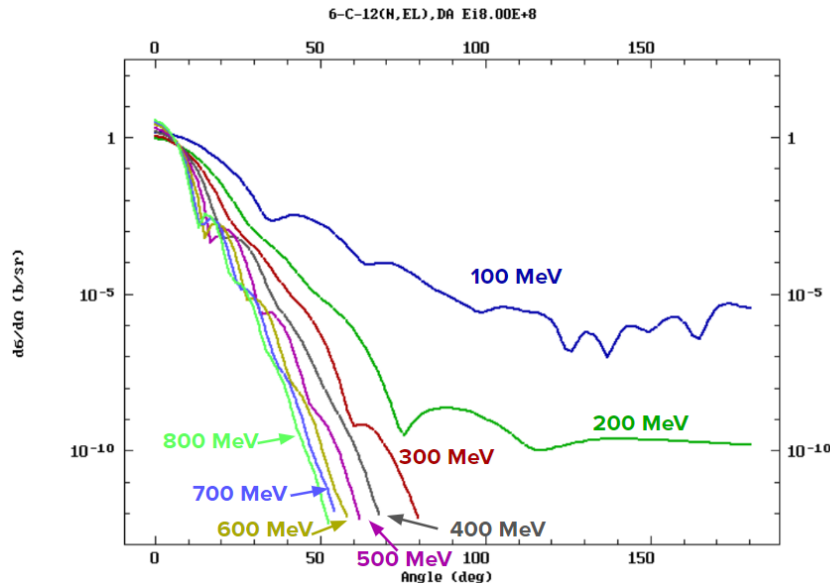


Figure 3.4. Cross section distribution of neutron interactions on carbon as a function of angle [5].

If we consider the cross section as a function of energy of neutron elastic scattering

with carbon between 10-800 MeV<sup>4</sup> as seen in Fig. 3.5, we see a generally decreasing cross section as incident neutron energy increases for incident neutron energies greater than 20 MeV. However, we note a faint dip structure centered around 500 MeV, after which the cross section slightly increases. We would expect the distribution of the kinetic energy and momenta of outgoing neutrons to agree with the overall shape of this distribution, showing a deeper dip structure around the same incident energy value on a linear scale.

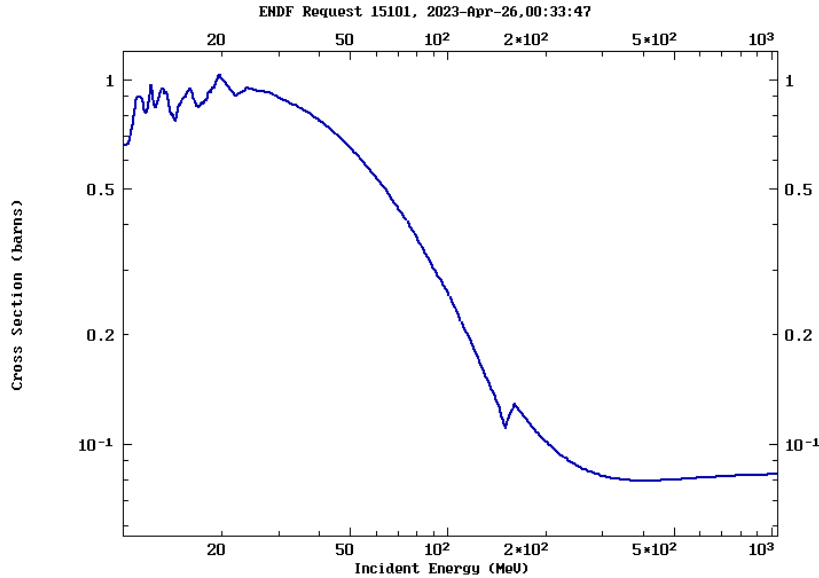


Figure 3.5. Cross section as a function of incident neutron kinetic energy for elastic scattering on carbon [5].

### 3.2.3 Inelastic Scattering

Inelastic scattering of neutrons on carbon causes production of many outgoing particles of different particle types. Interaction channels for  $\pi^0$  production of neutrons on carbon require threshold energies on the order of  $> 1\text{GeV}$ ; hence we should not expect to see  $\pi^0$  production as our incident neutrons have energies from 0-800 MeV.

### 3.2.4 Theoretical Cross Section Distributions

If we consider the cross section as a function of energy for neutron inelastic scattering with carbon between 5-800 MeV<sup>5</sup> as seen in Fig. 3.6, we see that the cross section increases as a function of incident energy until  $\sim 20$  MeV, at which point it decreases until it gradually flattens out. We observe a faint dip structure centered

<sup>4</sup>The shape of the distribution in the 0-10 MeV range provided by the ENDF is very different from the shape of the distribution from 10-800 MeV. The shape of the 0-10 MeV range is not significant for the exploration of this thesis, hence was not included in this section as it would distract from the shape of the distribution from 10-800 MeV

<sup>5</sup>The shape of the distribution in the 0-5 MeV range provided by the ENDF is very different from the shape of the distribution from 5-800 MeV. The shape of the 0-5 MeV range is not significant for the exploration of this thesis, hence was not included in this section as it would distract from the shape of the distribution from 5-800 MeV

at around 400 MeV, after which the cross section visibly increases for higher incoming neutron energies. We would expect the distribution of the kinetic energy and momenta of outgoing neutrons to agree with the overall shape of this distribution, possibly showing a similar dip structure around the same incident energy value on a linear scale.

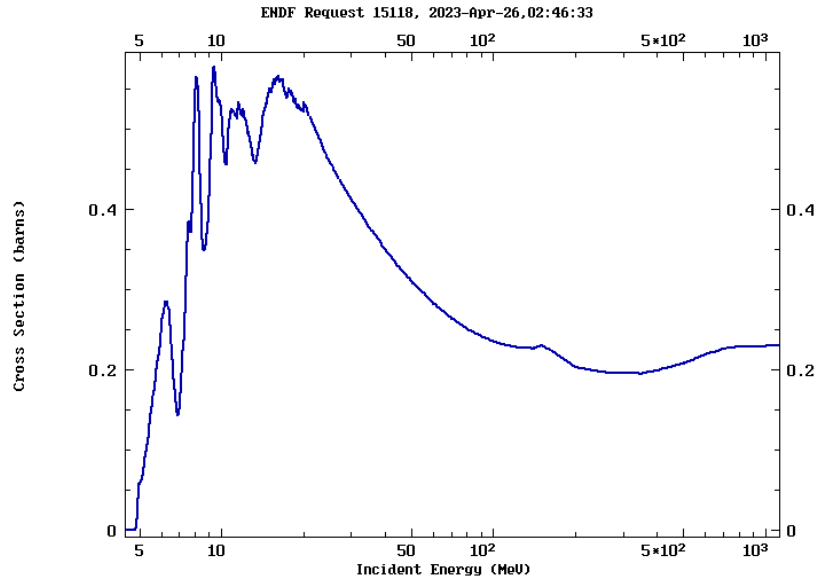


Figure 3.6. Cross section as a function of incident neutron kinetic energy for inelastic scattering on carbon [5].

We have used ENDF data to obtain the total neutron cross sections as a function of incident neutron kinetic energy for inelastic scattering on carbon, organized by produced particle type as seen in Fig. 3.7. The ENDF does not contain information for outgoing carbons from inelastic interactions, so these have been omitted from the following plot. Plots of individual cross sections as a function of energy have been provided in the appendix.

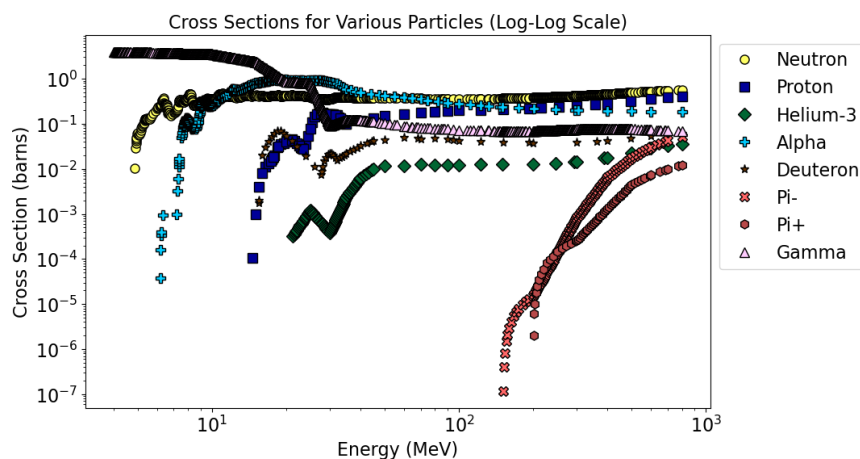


Figure 3.7. Cross section as a function of incident neutron kinetic energy for outgoing neutrons from inelastic scattering on carbon, organized by type of particles produced in these interactions, presented on a log-log scale [5].

# Chapter 4

## Monte Carlo Studies

### 4.1 Monte Carlo Simulation

Analyses were conducted over Monte Carlo (MC) simulation files created using 3 different physics lists based on a parameterised modelling for hadronic interactions for all particles [6]. MC simulations refer to computer-generated simulations which use stochastic (random) numbers to estimate the outcomes of processes, and are heavily used in modelling statistical mechanics. They are able to generate nonuniform distributions of random numbers for statistical modelling, making them ideal for simulating interaction probability and energy loss outcomes for particles in matter. This makes them ubiquitous in high energy particle physics. A more in-depth explanation of the methods used to generate the MC simulations is available in Ref. [7], though it is not required for this thesis.

Our MC simulations were created using Geant4 [8] [9] [10] (Geant is used interchangeably throughout the text) - a computational toolkit used to model particle interactions in matter. Geant tracks and categorizes particle events, allowing us to more easily identify parameters of interest such as particle type, interaction type, and energy deposition among others. There are a wide variety of different Geant releases which enable study into different particle interactions through the unique features available in each version, a link to all of them is provided in Ref. [11]. Our analyses focuses on the use of Geant version 4.10.6.

The MC files can be run over different parameters which apply different models for high energy interactions of particles with nuclei - such models are referred to as “physics lists” in the context of Geant-based simulations. Different physics lists can be used based on the research goals of the user. The majority of this thesis will focus on MC simulations created using the BERTINI Cascade Model, which is a widely used classical model for solving the Boltzmann equation for a particle moving through nucleons. The BERTINI Cascade Model assumes the medium through which the particle travels is a gas under the assumption that the nucleon size is small relative to the medium.<sup>1</sup> This model has been greatly improved and re-written by developers in its capability to model interactions at

---

<sup>1</sup>For completeness, the BERTINI Cascade Model also applies the quark gluon string model for high energy interactions of protons, neutrons, pions, and Kaons with nuclei above  $\sim 10$  GeV, which is relevant considering the nuclei of carbon is  $>11$  GeV; although this information is not necessary for a deeper understanding of the thesis.



greater energy ranges and to account for different particle types and cross sections since its inception. A comprehensive description to the features of this model can be found in Ref. [10].

Analyses on MC simulations created using different physics lists (BERTINI HIGH PRECISION (HP) and INCL (INCLXX)) is also explored in this thesis to verify the validity of the analysis conducted on MC simulations generated using the BERTINI physics list, and to investigate the effect of different particle-nuclei cascade models on the analyses. BERTINI HP is an extension of BERTINI to improve accuracy below the 20 MeV range, and INCLXX is a physics list that uses the Leige Intranuclear Cascade model for proton, neutron, and pion interactions interactions below  $\approx 3$  GeV instead of the BERTINI Cascade model, in addition to reactions induced by light nuclei [6]. Key features of INCLXX include the Woods-Saxon nuclear potential and charged pion ( $\pi^\pm$ ) cross sections, among others - a comprehensive description to the features of this model can be found in Ref. [12].

The following kinematics study was conducted over elastic and inelastic scattering of incoming neutrons on a hydrogen target, a carbon target, and a CH target. Analyses of neutron interactions on the hydrogen and carbon targets were conducted separately to better understand the features apparent in the analysis of neutron interactions on the CH target. Elastic scattering is defined as an interaction between particles in which there is conservation of kinetic energy in the Center-of-Mass (CoM) frame, while the kinetic energy is not conserved in the CoM Frame for inelastic scattering. Hydrogen, carbon and CH analyses (as they will be referred to henceforth, for brevity) were conducted on MC simulations generated using the BERTINI physics list, and using Geant version 4.10.6. Comparisons between analyses conducted on MC files created using the BERTINI, BERTINI HP and INCLXX physics lists are shown in 4.5.

A MC analysis on neutrons interacting with CH was conducted to investigate the interaction of the neutron beam on the SuperFGD prototype. The main goals of the MC studies were to investigate the kinetic energy, momentum, and  $\theta$  distributions for outgoing particles from both inelastic and elastic collisions of neutrons with CH. The results of these investigations are illustrated below.

## 4.2 Event Selection

Edep-sim (an energy deposition simulator based on Geant4, Ref [13]) was used to help simulate and analyze Geant4 output. Geant4 handles particle creation non-intuitively, therefore it is of key interest to understand the event selection process. A particle in the simulation is created with fixed points along its trajectory for its entire lifespan. Consider Figure 4.1, representing a neutron moving through space: each small dot represents a point in the simulation, and for each point we are able to extract the information of the particle's position relative to the origin (set as the center of the detector), momentum, kinetic energy, and other kinematics. Each point in a particle's trajectory is given a `ProcessID` and a `SubProcessID` value, representing the type of interaction the particle undergoes at that point. A table of `ProcessID` and `SubProcessID` values and what they refer to is provided in tables I and II in the Appendix. The `ProcessID` and `SubProcessID` values were sourced

from the [Geant4 Documentation Ref \[14\]](#). A comprehensive list of the particle numbering system can be viewed in the official Monte Carlo Particle Numbering Scheme Ref [15].

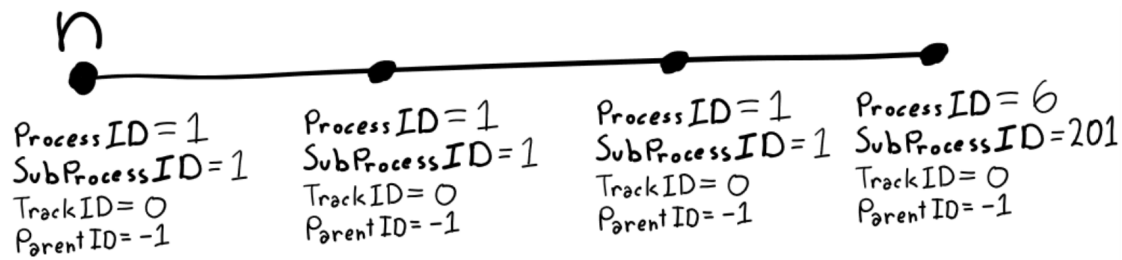
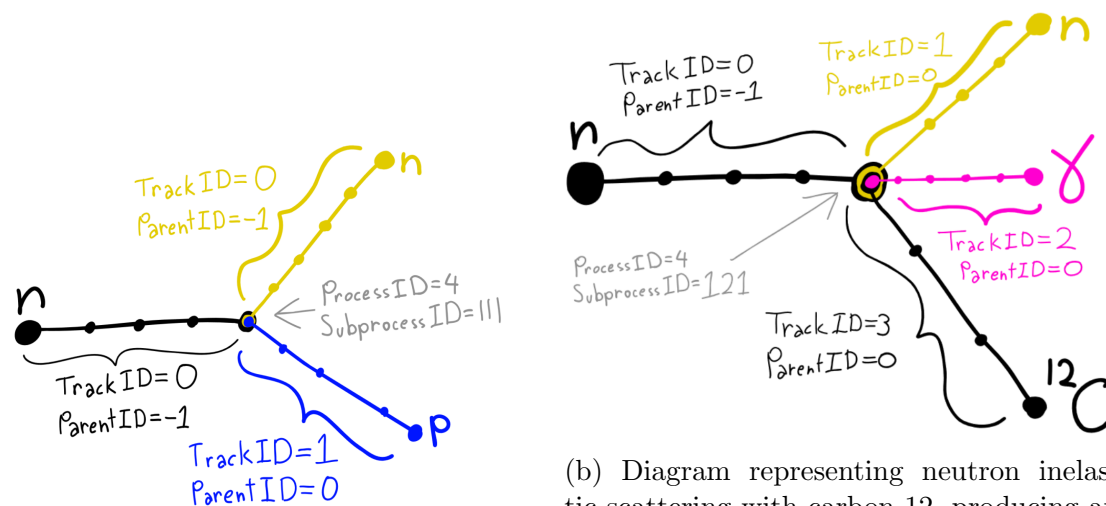


Figure 4.1. Diagram of how Geant4 tracks a neutron moving without interacting in matter. The neutron decays at the final point of its' trajectory, changing the ProcessID and SubprocessID at that point.



(a) Diagram of neutron elastic scattering off free hydrogen.

(b) Diagram representing neutron inelastic scattering with carbon-12, producing an outgoing neutron, outgoing carbon, and outgoing  $\gamma$ .

Figure 4.2. Diagrams of how Geant4 tracks particles interacting with matter.

Note that each particle's trajectory is labelled with a **TrackID** value (the track object index in the particle stack) which is (usually) useful for identifying each particle individually. Each particle also has a **ParentID** value, which refers to the **TrackID** of its' parent. **TrackID**'s are indexed from 0 and **ParentID**'s are indexed from  $-1$ . In Fig. 4.2a we observe an incoming neutron (black) interacting elastically with free hydrogen, resulting in an outgoing neutron (yellow) and outgoing proton (blue). We refer to the "outgoing" neutron(s) as the neutron(s) *immediately after the point of interaction*; so for Fig. 4.2a the incoming and outgoing neutrons are the same particle, but "incoming" refers to the neutron before elastic scattering, and "outgoing" refers to the neutron after elastic scattering. The **ProcessID** and **SubProcessID** values change at the point of interaction, which is why they have been pointed out on Fig. 4.2a. This can also be seen on Fig. 4.1. Consequently, the **ProcessID** and **SubProcessID** values for the last point of the incoming neutron are identical to the **ProcessID** and **SubProcessID** for the first point of the outgoing proton and neutron.

The Analysis code iterates over all events in a given list of MC files, and for each event it iterates over every point in each particles' trajectory. We search for the `ProcessID` of the particle at each point to identify a particle collision. If the particle is undergoing transportation (`ProcessID=1`) for a given point, we ignore the point and continue to the next point until we encounter a `ProcessID` indicative of a (hadronic) interaction (`ProcessID=4`). We ignore all interactions that are non-hadronic, and only focus on first hadronic interactions. For example, we may have a neutron that first interacts non-hadronically with CH and produces an outgoing particle which some number of points later interacts hadronically with CH; such an interaction is ignored, as only the first interaction of incident neutrons in each event is considered, and only if that first interaction is hadronic. The treatment of each particle is different depending on the particle type and interaction type. Moreover, we have placed a cut on the distance between the position of the first point in the produced particles' trajectory and the interaction vertex to ensure we consider only outgoing particles resulting from the first hadronic interaction of a neutron on the target. This cut was placed on both inelastic and elastic events and requires that the aforementioned points be less than  $1 \times 10^{-5}$  mm apart.

Determining the momentum of the outgoing particles from elastic collisions follows intuitively from how it is handled in Geant4. The outgoing proton is generated at the vertex after a collision occurs, hence the kinetic energy, momentum, and  $\theta$  values for the proton are obtained at the point which the proton was created, and a new `TrackID` is generated for the proton. Geant4 're-uses' the information from the incident neutron for the outgoing neutron for elastic scattering: a new particle is not created, hence no new `TrackID` is assigned to the outgoing neutron. Therefore, we must take the kinematics of the outgoing neutron as the kinematics of the neutron at the point of interaction.

However, determining the momentum of the outgoing neutron from inelastic collisions does not follow so intuitively. For inelastic collisions we can expect many types of outgoing particles including protons,  $\pi^{\pm}$ 's, neutrons,  $\gamma$ 's,  $\alpha$ 's,  $D$ 's,  ${}^3\text{He}$ 's, and isotopes of carbon in addition to other particles grouped as 'others'. Some of these include isotopes of Beryllium and Boron. For inelastic collisions we may have interactions within the nucleus of the carbon atom that are not tracked by Geant4, hence Geant4 does not preserve the programming object associated with the incoming neutron as an outgoing neutron - the `TrackID` of the outgoing neutron is changed from the `TrackID` of the incoming neutron, as is depicted in Fig. 4.2b. Therefore the kinematics of all particles are obtained as their initial values (from the vertex of interaction).

The event selection was conducted using a script called `neutrong4simulationanalysis`, which has been uploaded to [this gitlab](#) Ref [16] and is run over a set of MC simulation files. At the time of writing, pre-determined directories and file names for the MC simulations have been implemented as can be seen in the `RunAnalysis.cxx` script. Though these are hard-coded at the moment, progress is currently being made to make the analysis more robust with command line implementation as will be expanded upon in Chapter 6. A plotting script for the output `.root` file from the analysis is also provided in the gitlab, as well as a plotting script for the comparisons of different physics lists in Section 4.5.

### 4.3 Elastic Scattering

Once the first hadronic interactions are determined and the kinematics for each outgoing particle are stored, histograms are created to organize kinematics distributions by particle type and by collision type. In this section only notable histograms are shown, the rest being included in the appendix. In order to best understand the results of neutron interactions on a CH target, let us focus on neutron interactions on hydrogen and on carbon first. MC simulations were conducted for neutron interactions on a target comprised entirely of hydrogen and a target comprised entirely of carbon for comparison with the MC simulations of neutron interactions on CH for this purpose. The ratio of carbons to hydrogens in the CH MC simulations is approximately 1 1. All plots shown consider incoming neutrons with energies from 0-800 MeV, unless otherwise specified. Note that these MC simulations were conducted on targets with the same volume and total mass, hence targets with different material makeups had different numbers of nucleons. Therefore, the total number of neutron interactions with hydrogen and carbon differ between each file. For example, there are more neutrons interacting with hydrogen atoms on a hydrogen target than there are neutron interactions with hydrogen atoms on a CH target.

For elastic scattering of neutron on hydrogen target, figure Fig. 4.3 shows the distribution of the outgoing neutron's angle relative to the beam ( $\theta$ ) and illustrates distinct features discussed in Chapter 3. Note the sharp drop at  $90^\circ$ ; there are almost no outgoing neutrons which are going backwards (in the beam direction), which makes sense considering that the neutron and proton have very similar masses ( $\approx 939$  MeV for the neutron and  $\approx 938$  MeV for the proton) and from classical kinematics we know we should not expect an elastic collision between 2 objects with very similar masses to result in one of the objects moving backwards. Note that there are some events on this histogram which show neutrons with  $\theta > 90^\circ$ , however we can confidently conclude these are features of the simulation, considering there are less than 50 of these events compared to our total  $1.15 \times 10^7$  events. Additionally, we observe a dip structure for the outgoing neutrons, with one peak around small  $\theta \approx 15^\circ$  being much higher than the peak centered around  $\theta \approx 70^\circ$ . We know that we should expect this given the accepted result for the neutron cross section as a function of  $\theta$  from Section 3.1.2. We also note that, given the low  $\theta$  peak is higher for outgoing neutrons than the high  $\theta$  peak, we should expect a similar double peak and dip structure in the  $\theta$  distributions for outgoing protons from elastic scattering on free hydrogen. However, the peak at high  $\theta$  should be higher than the peak at low  $\theta$  for the proton distributions due to the  $\approx 90^\circ$  difference discussed in Section 3.1.1. In fact this is what we observe; Figure Fig. 4.4 shows a dip and double peak structure with the peak at high  $\theta$  being higher than the peak at low  $\theta$ .

The integrals of the histograms in figures Fig. 4.3 and Fig. 4.4 differ by  $\approx 0.09\%$  due to a feature of the Geant4 toolkit. We occasionally have incoming neutrons that interact elastically with free hydrogen, however the outgoing hydrogen may not have sufficient energy for Geant4 to track it and hence only the outgoing neutron is tracked.

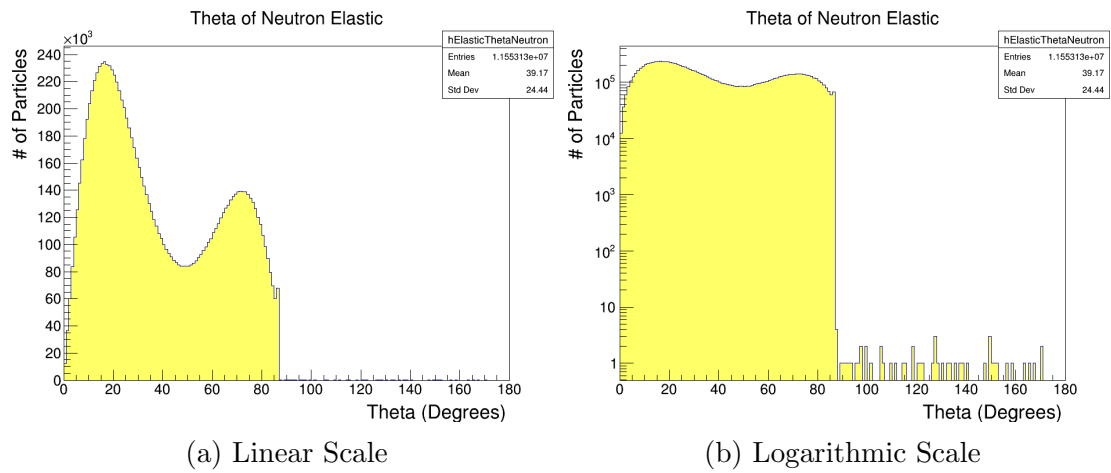


Figure 4.3. Angle relative to beam ( $\theta$ ) of outgoing neutrons from elastic scattering of neutrons on a hydrogen target.

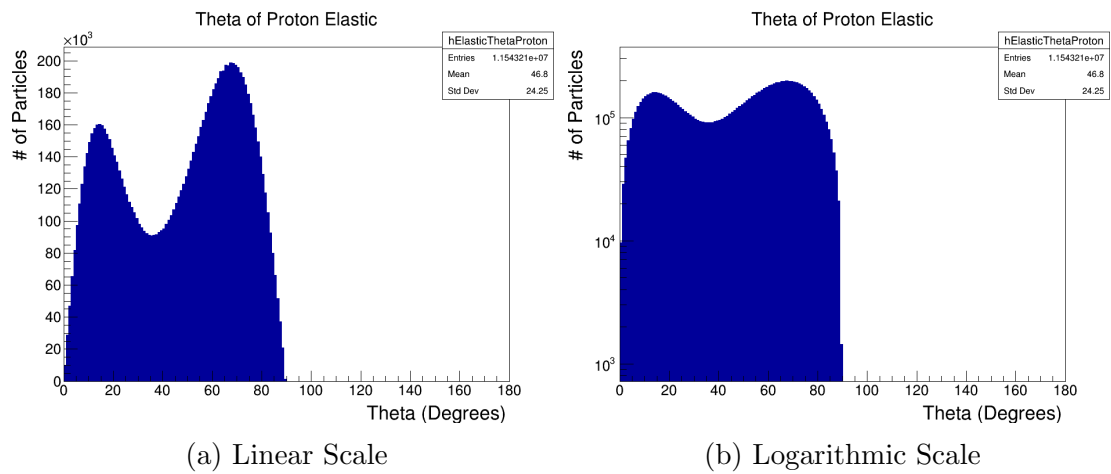


Figure 4.4. Angle relative to beam ( $\theta$ ) of outgoing protons from elastic scattering of neutrons on a hydrogen target.

In fact, we may plot the kinetic energy of the incoming neutron against the  $\theta$  of the outgoing proton in a 2D histogram in order to observe the position of the dip structure changing as a function of energy, as we have done in figure Fig. 4.5. Here we observe the 'dip' structure represented as an area of low density shifting as the kinetic energy of the incoming neutron increases. We also see there is a much lower density of  $\theta$  around the center of the dip for 800 MeV incoming neutrons when compared to 350 MeV incoming neutrons.

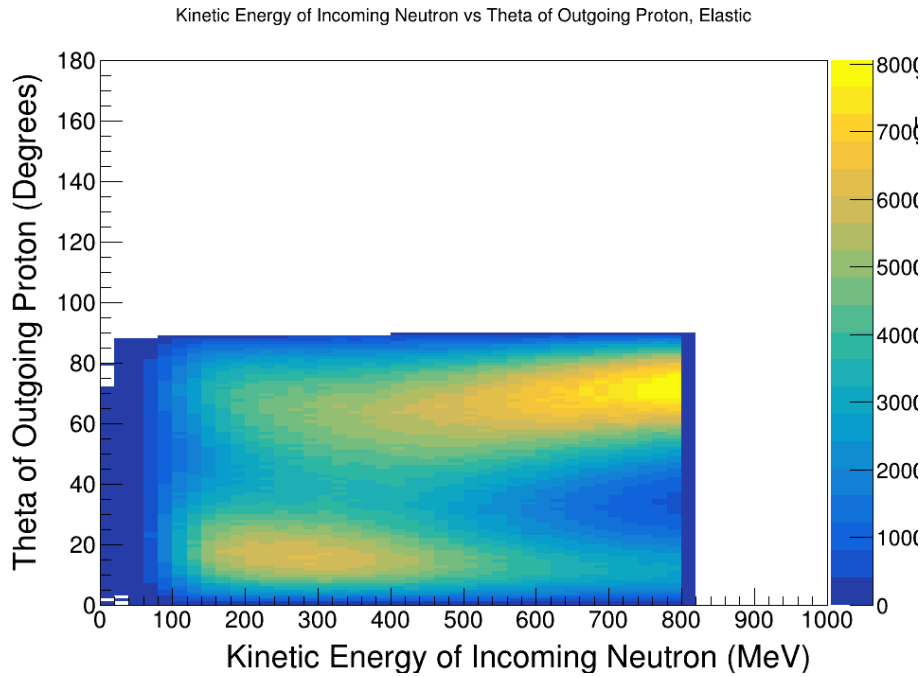


Figure 4.5. 2D plot of angle relative to beam ( $\theta$ ) of outgoing protons from elastic scattering of neutrons on free hydrogen against kinetic energy of incoming neutron.

Likewise, if we consider the  $\theta$  distributions for outgoing neutrons from elastic scattering of neutron on carbon, we note that we similarly see features present in Fig. 3.4. Fig. 4.6 illustrates that the majority of outgoing neutrons from elastic scattering of neutron on carbon is at low  $\theta$ , while we do see some non-negligible amount of neutrons being scattered off of carbons at angles  $> 90^\circ$ .

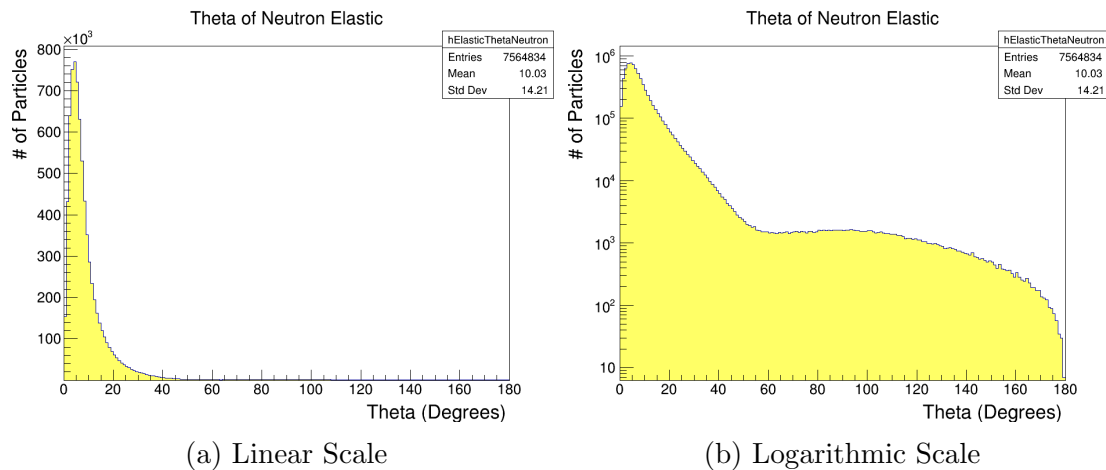


Figure 4.6. Angle relative to beam ( $\theta$ ) of outgoing neutrons from elastic scattering of neutrons on a carbon target.

Figure Fig. 4.7 illustrates that we have no carbons with  $\theta > 90^\circ$ , which agrees with our expectations given the relatively high mass difference between a neutron and a carbon nucleus; from classical mechanics if we have elastic scattering of  $m_2$  on  $m_1$  at rest, where  $m_1 \gg m_2$ , we do not expect  $m_1$  to move backwards due to conservation of energy, but we may have that  $m_2$  moves backwards. The majority of carbons

have  $\theta$  close to  $90^\circ$ , which makes sense since the majority of neutrons have low  $\theta$  values and given the expected angle between outgoing particles calculated in section 3.2.1.

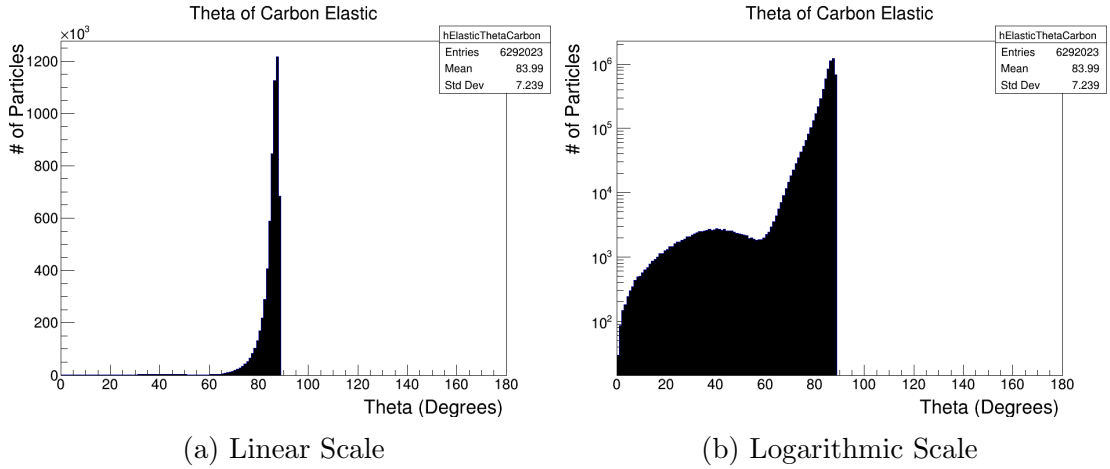


Figure 4.7. Angle relative to beam ( $\theta$ ) of outgoing carbons from elastic scattering of neutrons on a carbon target.

The integrals of the histograms in figures Fig. 4.6 and Fig. 4.7 differ by  $\approx 16\%$ , due to the aforementioned limitations of the Geant4 toolkit. Namely, we believe that there are significantly larger number of outgoing carbons that do not have sufficient energy to be tracked by Geant4 in figure Fig. 4.7 than there are number of outgoing hydrogens that do not have sufficient energy to be tracked by Geant4 in figure Fig. 4.4 since the mass of carbon is about 6 times the mass of the incoming neutron; whereas the mass of the proton is very similar to the mass of the incoming neutron. As determined in section 3.2.1 incoming neutrons cannot transfer as much energy to carbons as they can to free protons, therefore we would expect that there would be more carbons with energies too low for Geant4 to track as particles. Moreover, higher energy neutrons do not transfer as much energy to the carbons as lower energy neutrons, as neutrons with higher energies have higher momenta and therefore lower De Broglie wavelengths. As the De Broglie wavelength of an incoming neutron approaches the size of the nucleon-nucleon scale, the neutron is more likely to interact with a single nucleon in the carbon atom than with the entire carbon atom itself - resulting in an inelastic collision.

Combining the features we see from the studies of neutron interactions on free hydrogen and on carbon, we see that we have these features apparent in neutron interactions with CH. We observe the sharp drop at  $90^\circ$  in plot Fig. 4.8b, which we attribute to the sharp drop at  $90^\circ$  from neutron elastic scattering on hydrogen. Any neutrons with  $\theta > 90^\circ$  are due to neutron elastic scattering on carbon. Moreover, we attribute the dip structure in the neutron and proton distributions as a feature of the cross section as a function of angle as mentioned previously. There are less than 1300 outgoing “other” particles out of our  $6.4 \times 10^7$  events, so these are negligible and can be ignored.

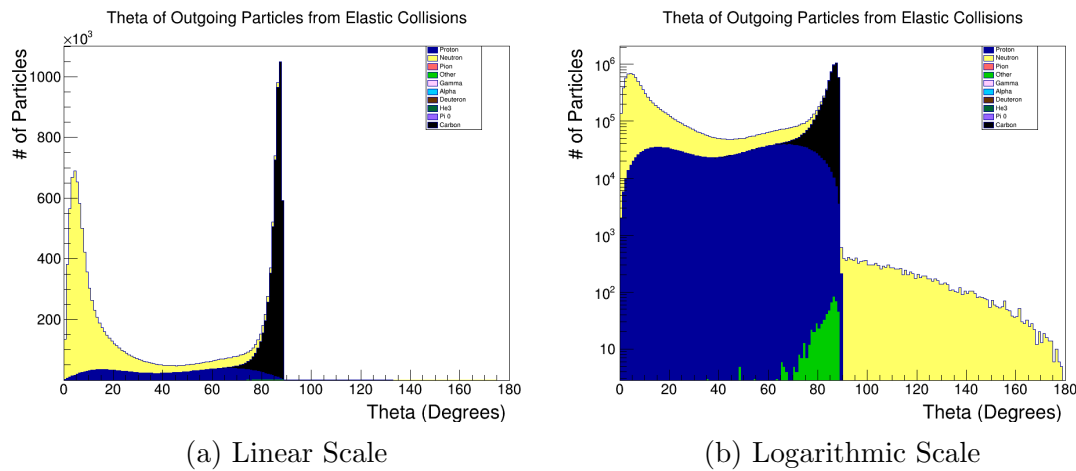


Figure 4.8. Stacked histogram of angle relative to beam ( $\theta$ ) of outgoing particles from elastic scattering of neutrons on a hydrocarbon target.

The angle  $\theta$  was determined using the momenta of the particles from the simulation following Eq. (4.1):

$$\theta = \arctan \left( \frac{\sqrt{P_x^2 + P_y^2}}{P_z} \right) \quad (4.1)$$

The distributions for Kinetic energy of outgoing neutrons from elastic scattering of neutron on hydrogen (Fig. 4.9) and on carbon (Fig. 4.11) mirror the features expected in the cross section distributions Fig. 3.2 and Fig. 3.5, respectively. The kinetic energy distributions of outgoing protons from elastic scattering of neutron on hydrogen in Fig. 4.10 closely follow the kinetic energy distributions of outgoing neutrons in Fig. 4.9. We have performed an energy balance calculation on the difference between the energy of the incoming neutron and the sum of the energies of the outgoing proton and neutron, and have found that in  $> 99\%$  of events we have an energy balance of 0.<sup>2</sup> Therefore, given that the distribution for the kinetic energy of the neutron agrees with expectations from theory we can conclude that the distribution for kinetic energy of outgoing protons follows as expected. There are more outgoing neutrons in Fig. 4.9 than there are outgoing protons in Fig. 4.10. Notably, this occurs more frequently at higher energies since high energy neutrons which glance the proton do not impart sufficient energy to the proton for it to be tracked by Geant4, as discussed earlier. Distributions for kinetic energy of outgoing carbons were not created since we calculate the kinetic energy by subtracting the mass of the carbon isotope from its' total energy, but under these carbons we also have all isotopes from  $C^8$  to  $C^{13}$ . We combine our understanding of the kinetic energy distributions for elastic collisions to note that these features are present in Fig. 4.12. It appears there are more outgoing neutrons than protons in Fig. 4.12 as neutrons in this histogram have interacted elastically with both proton and carbon, though distributions for the kinetic energy of outgoing carbon are not shown here.

<sup>2</sup>Technically speaking over  $> 99\%$  of events have an energy balance between 0-1 MeV, though this is due to computational limitations of difference calculations i.e.  $450-450=1 \times 10^{-3}$  on a computer.



We therefore conclude that the structures observed for outgoing neutrons and protons in Fig. 4.12 agree with what we expect from theory.

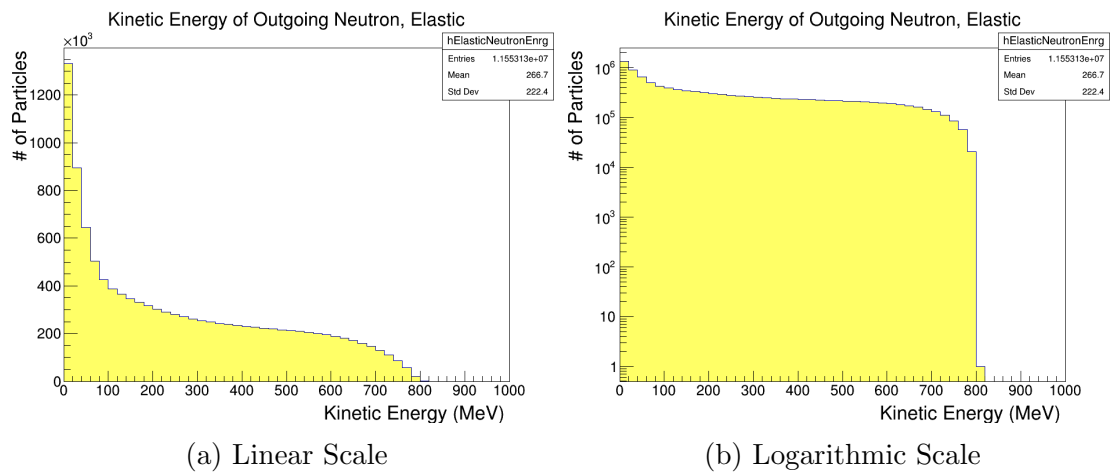


Figure 4.9. Kinetic energy of outgoing neutrons from elastic scattering of neutrons on a hydrogen target.

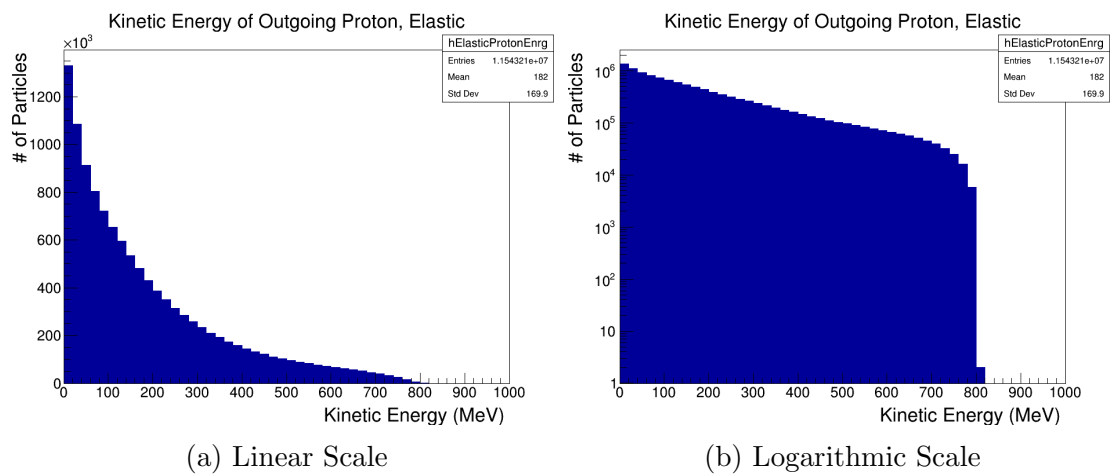


Figure 4.10. Kinetic energy of outgoing protons from elastic scattering of neutrons on a hydrogen target.

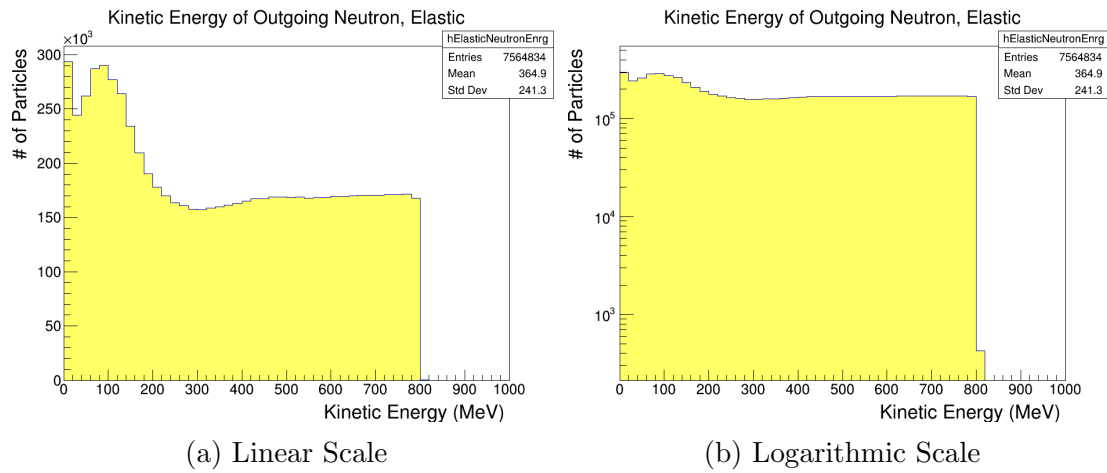


Figure 4.11. Kinetic energy of outgoing neutrons from elastic scattering of neutrons on a carbon target.

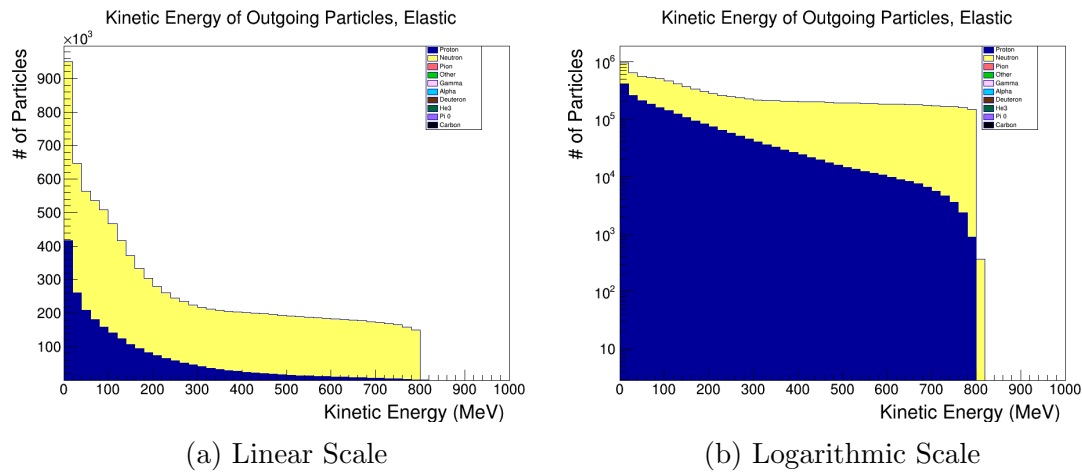


Figure 4.12. Stacked histograms for the kinetic energy of outgoing particles from elastic scattering of neutrons on a hydrocarbon target.

We are unable to determine what features we would expect for momentum distributions of outgoing particles from elastic interactions of neutrons on hydrogen and carbon from the respective cross section distributions as functions of incoming neutron energy. However, we note that due for relativistic particles,

$$E = \frac{P}{\beta\gamma} \quad (4.2)$$

where  $E$  is the particle's total energy,  $P$  is the magnitude of the particle's momentum, and  $\beta$  &  $\gamma$  are standard relativistic quantities proportional to the velocity of the particle. Hence, since we have verified that the kinetic energy distributions agree with expectations, and since we have determined the kinetic energy of outgoing particles by subtracting the mass from the total energy, we can conclude that the following distributions for the momenta of outgoing particles from elastic interactions are valid. Moreover, our analyses of  $\theta$  distributions for outgoing particles illustrate features which agree with accepted literature from the ENDF. Recalling the dependence of  $\theta$  on the particle's momentum given by Eq. (4.1), we

gain further confidence in the validity of our momentum distributions. Fig. 4.13 and Fig. 4.15 show the momenta of outgoing neutrons from elastic scattering on hydrogen and carbon targets, respectively. We observe a peak in the number of outgoing neutrons with momenta around 200-350 MeV followed by a steady decline in number of neutrons for higher momenta in Fig. 4.13a. We also see a dip structure in the number of outgoing neutrons with momenta around 600-900 MeV in Fig. 4.15a. The dip structure in Fig. 4.15a around 600-800 MeV agrees with the dip structure predicted by Fig. 3.5 (recall  $E^2 = p^2 + m^2$  for relativistic particles). We have a significantly higher number of outgoing neutrons in the 0-50 MeV bin than in the 50-100 MeV bin for Fig. 4.15; which is likely a feature of running the analyses on MC simulations created using the BERTINI cascade model which does not accurately model particle kinematics in the 0-20 MeV range as much as the BERTINI HP cascade model.

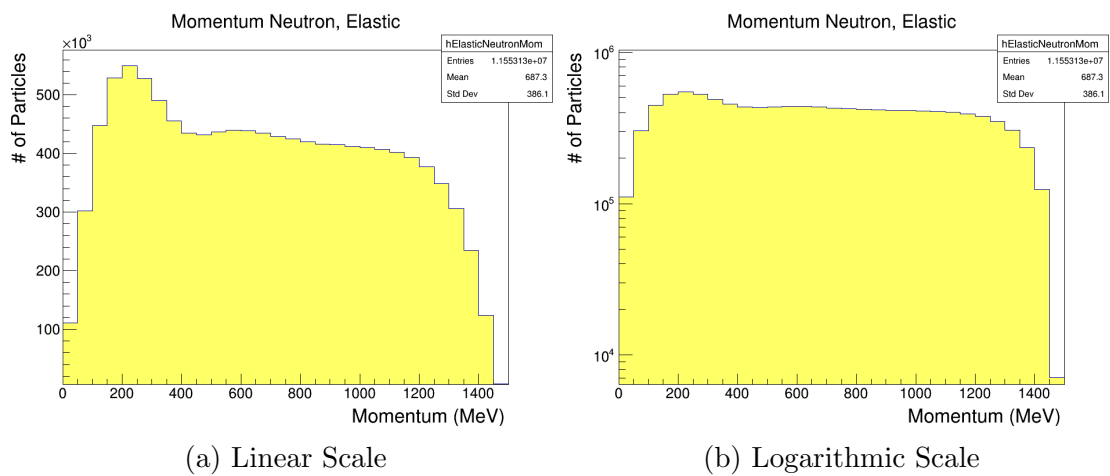


Figure 4.13. Momentum of outgoing neutrons from elastic scattering of neutrons on a hydrogen target.

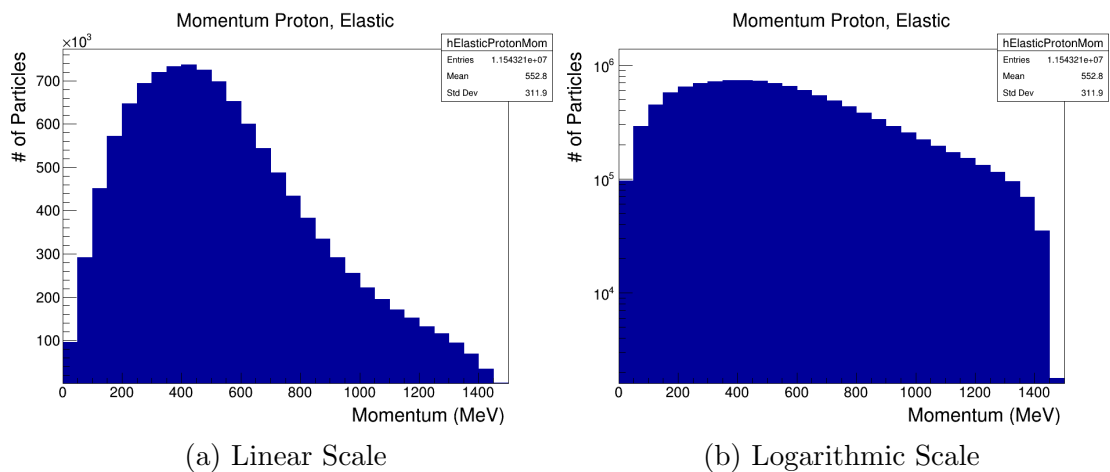


Figure 4.14. Momentum of outgoing protons from elastic scattering of neutrons on a hydrogen target.

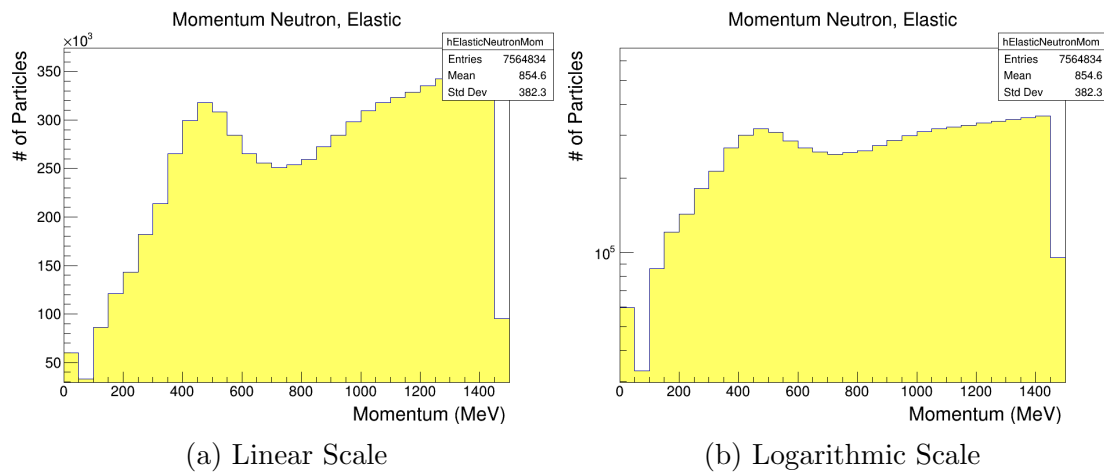


Figure 4.15. Momentum of outgoing neutrons from elastic scattering of neutrons on a carbon target.

Fig. 4.16 shows that the majority of outgoing carbons from neutron elastic scattering on carbon have momenta below 250 MeV, with no outgoing carbons with momenta above 900 MeV. The significantly larger mass of the carbon relative to the incident neutron limits the magnitude of the momentum transfer between the two particles, resulting in this highly populated low MeV region.

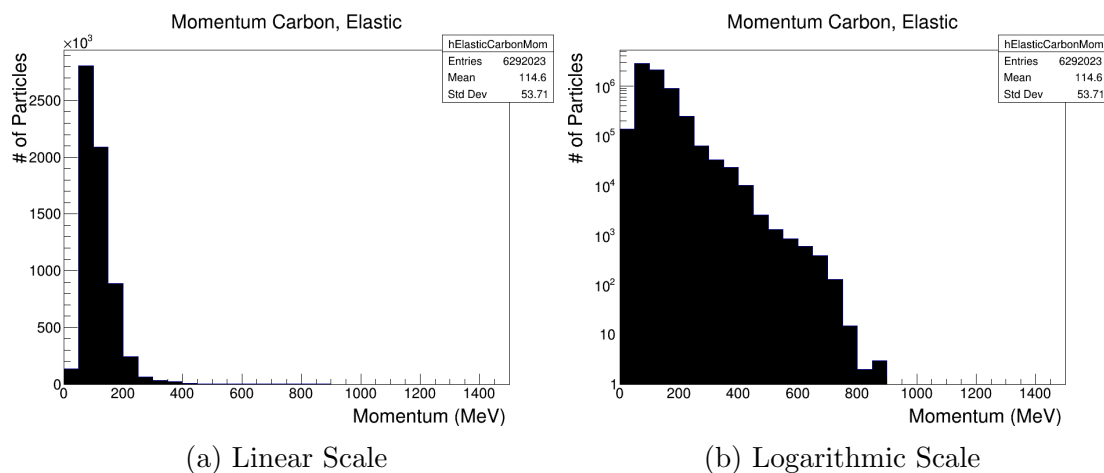


Figure 4.16. Momentum of outgoing carbons from elastic scattering of neutrons on a carbon target.

Therefore, we can identify the characteristics of Fig. 4.17 as the sum of the characteristics of the aforementioned momentum distributions. The high density of outgoing carbons at low MeV from elastic collisions of neutron on a CH target is due to the mass difference between the carbon and the neutron, and the validity of the overall shape and structure of the outgoing neutron and proton distributions is founded in the validity of the  $\theta$  and kinetic energy distributions. There are less than 1300 outgoing “other” particles out of our  $6.4 \times 10^7$  events, so these are negligible and can be ignored.

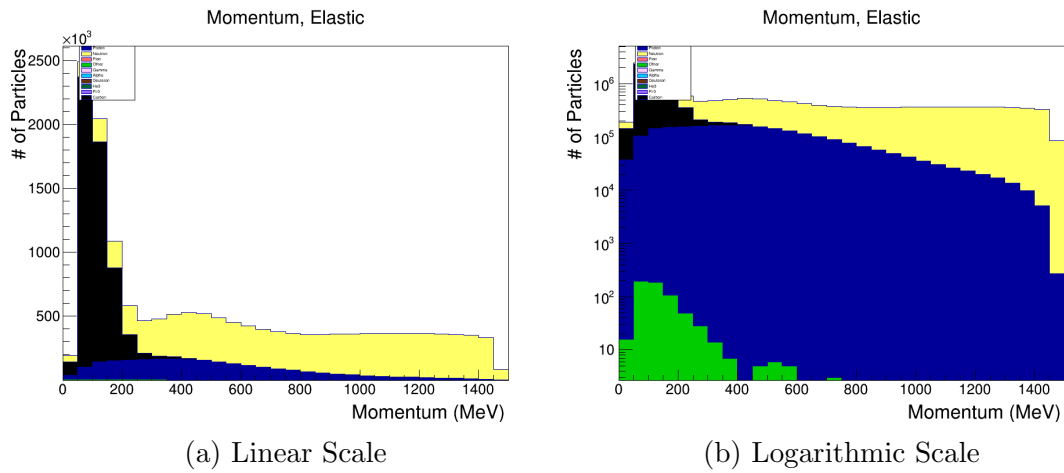


Figure 4.17. Stacked histogram of momentum of outgoing particles from elastic scattering of neutrons on a hydrocarbon target.

## 4.4 Inelastic Scattering

Fig. 4.18 shows stacked histograms for the momentum of outgoing particles from inelastic collisions of neutrons on hydrogen (Fig. 4.18a) and carbon (Fig. 4.18b) targets. We observe that inelastic scattering of neutrons on hydrogen is a source of charged pions production, and note a small amount of deuteron production. We do not observe  $\pi^0$  production from this analysis, however we attribute this to a limitation with the version of Geant4 used and believe this version is unable to track  $\pi^0$ 's. Older versions of Geant (i.e. 4.10.3) were unable to track outgoing carbons, motivating the belief in the limitation of the software to track  $\pi^0$ 's.

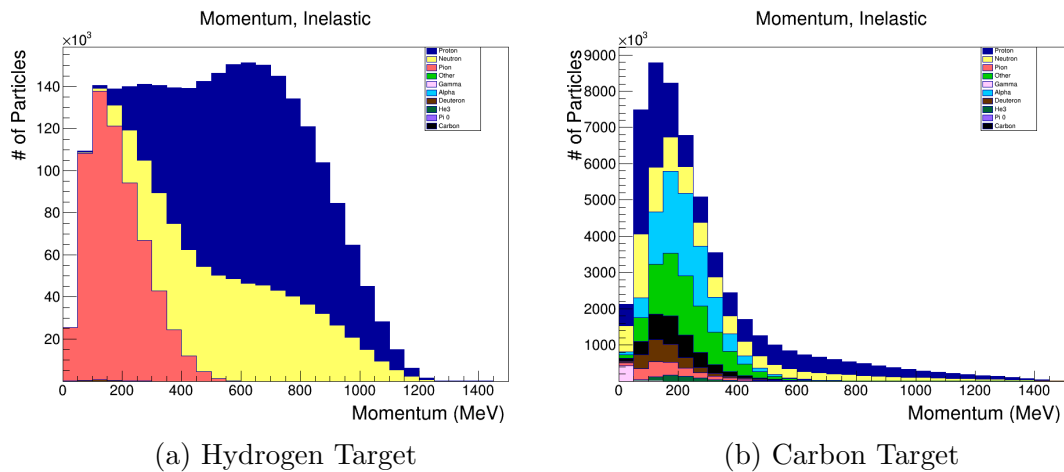
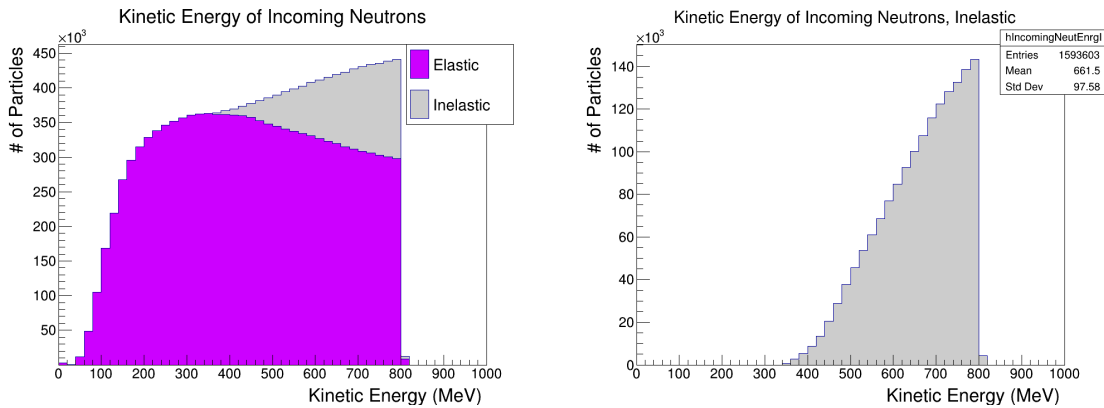


Figure 4.18. Stacked histograms of momentum of outgoing particles from neutron inelastic scattering on a hydrogen and a carbon target.

Fig. 4.19 shows kinetic energies of incoming neutrons organized by collision type which they undergo. Note that the stacked histogram is not flat as we are not including incoming neutrons which interact non-hadronically nor are we including non-interacting neutrons. Here we observe a discrepancy where - only considering the inelastic interaction channels in section 3.1.3 - we expect to observe inelastic interactions beginning at  $\sim 275$  MeV, however our analysis first shows inelastic

interactions at  $\sim 350$  MeV - illustrating a 75 MeV discrepancy. This discrepancy is unlikely to be a feature of the minimum energy required by Geant4 to track particles, as the minimum energy is on the sub-MeV scale and as we can see elastic neutron interactions in 0 - 20 MeV in Fig. 4.19b. It is noteworthy to consider that this distribution agrees with the structure of the expected cross section as a function of incoming neutron energy as seen in Fig. 3.3 - note the low cross section prior to  $\sim 275$  MeV on Fig. 3.3. Note also that the steep, order of magnitude jump in cross section from  $\sim 275$  MeV to  $\sim 350$  MeV in Fig. 3.3. The cause of this 75 MeV discrepancy is not fully understood and requires further investigation.



(a) Stacked histogram of kinetic energies of incoming neutrons which interact inelastically and elastically, linear scale.

(b) Kinetic energies of incoming neutrons which interact inelastically, logarithmic scale.

Figure 4.19. Stacked histogram of incoming neutron energies interacting with free hydrogen elastically and inelastically

Note that in Fig. 4.20 we do not see any charged pions with kinetic energy greater than 450 MeV, which makes sense since the minimum energy required to produce a charged pion at rest from neutron inelastic scattering off of hydrogen is  $\approx 279$  MeV. So, if we have an incoming 800 MeV neutron which inelastically interacts with hydrogen to produce 2 outgoing nucleons and an outgoing charged pion, the sum of the kinetic energies of the products can be at most  $\approx 521$  MeV. If the produced charged pion has 450 MeV, then the produced nucleons have a combined total energy of at most 71 MeV. However, note that we have outgoing protons and neutrons with kinetic energies between 520 MeV and 640 MeV; these are due to inelastic interactions between neutron and free hydrogen which require a lower threshold energy for the incident neutron and produce non-charged pion products - such as  $n + p \rightarrow n + p + \gamma$ .

All deuterons produced by inelastic scattering of neutrons on free hydrogen have kinetic energies lower than 40 MeV as seen by Fig. 4.22 and all outgoing  $\gamma$ 's have kinetic energies lower than 20 MeV as seen by Fig. 4.21. Given the threshold energy for deuteron +  $\pi^0$  production from inelastic interactions of neutrons on free hydrogen of 275 MeV, if we have an incoming 800 MeV neutron then the sum of the kinetic energy of the products can be at most 525 MeV. Therefore, if the produced deuteron has 40 MeV the produced  $\pi^0$  should have at most 485 MeV - but we do not see any  $\pi^0$  production whatsoever. Our leading understanding of

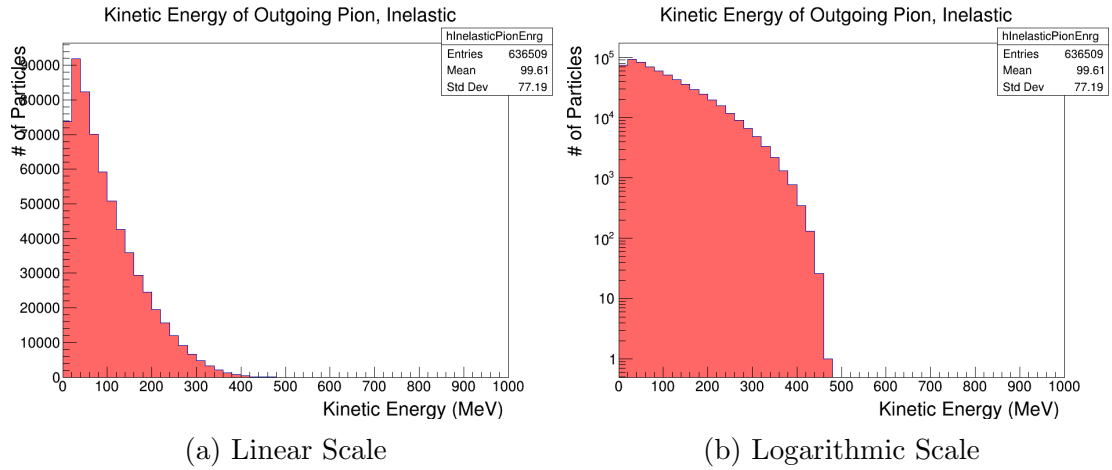


Figure 4.20. Kinetic energy of outgoing  $\pi^\pm$  from neutron inelastic scattering on a hydrogen target.

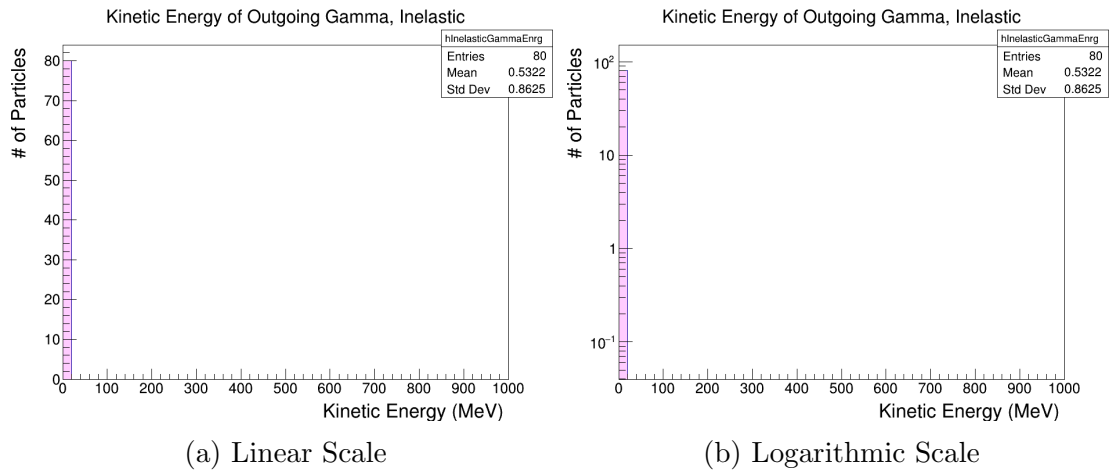


Figure 4.21. Kinetic energy of outgoing  $\gamma$ 's from neutron inelastic scattering on a hydrogen target.

the lack of  $\pi^0$  production is due to a limitation with the version of Geant4 used to create the analyzed MC files, that is to say this version of Geant4 does not **track**  $\pi^0$  production. It was postulated the shortness of the  $\pi^0$  lifetime would mean it decays before the simulation is able to track it; however if this was true we would see the decay products (outgoing  $\gamma$ 's) with significantly higher energies than are observed in Fig. 4.21, therefore we can confidently say that this is unlikely the case. Another possibility we postulate is that the cross section of deuteron +  $\pi^0$  production decreases as a function of incoming neutron energy, however this would need to be specifically for this interaction channel as it contradicts the increasing neutron inelastic cross section as a function of energy seen in Fig. 3.3. Further investigation into the Geant4 source code and creating MC files with different versions of Geant4 to run the analysis software over is necessary to fully understand the lack of  $\pi^0$  production.

Recalling the total integrated cross sections from 0-800 MeV for pion production discussed in Section 3.1.3, we note that we have a considerably higher number of outgoing protons than neutrons or charged pions. This would imply that the  $\pi^-$

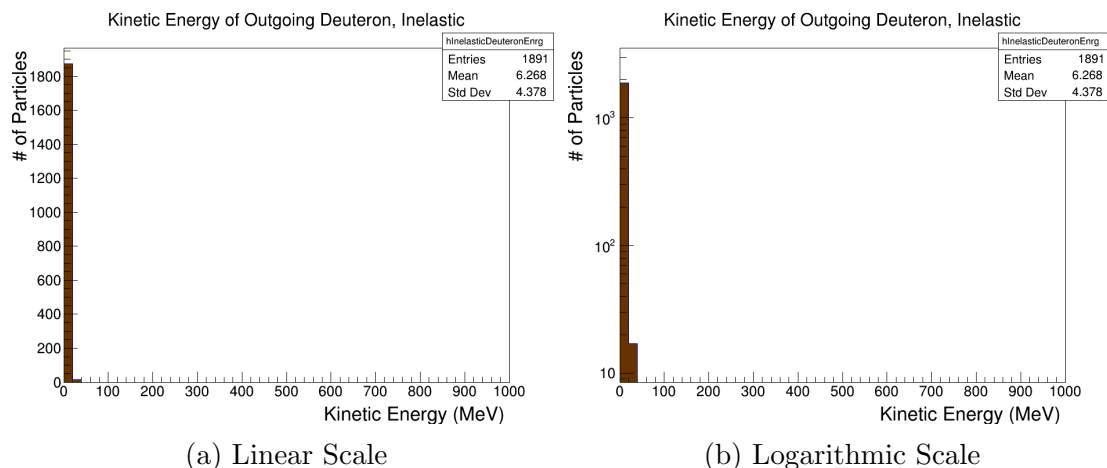


Figure 4.22. Kinetic energy of outgoing deuterons from neutron inelastic scattering on a hydrogen target.

production channel is preferred, except the integrated cross sections for charged pion production for incoming 0-800 MeV neutrons<sup>3</sup> suggest that we should have almost equal numbers of  $\pi^-$  and  $\pi^+$  produced. Inelastic interactions on hydrogen contribute an order of magnitude fewer events to the total inelastic scattering on CH than inelastic scattering on carbon. These discrepancies are not fully understood and require further investigation.

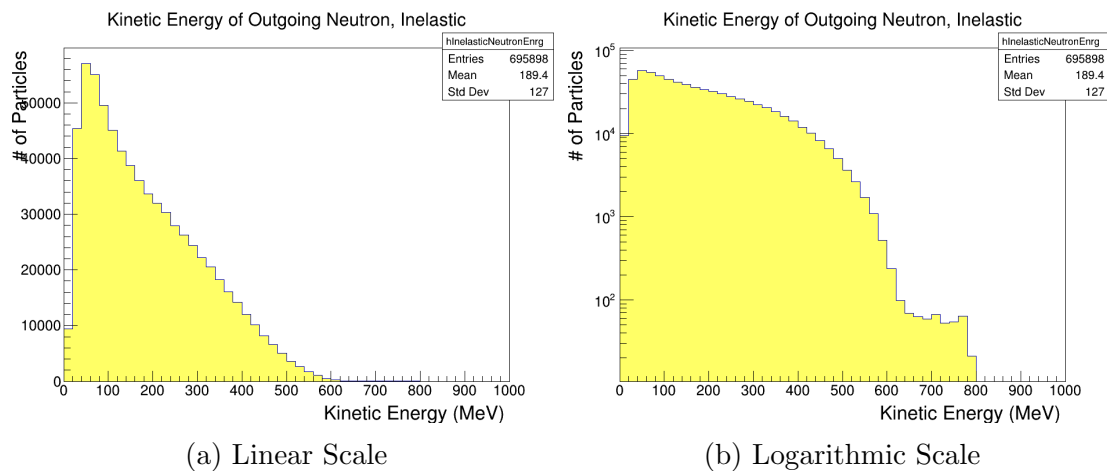


Figure 4.23. Kinetic energy of outgoing neutrons from neutron inelastic scattering on a hydrogen target.

<sup>3</sup> 0.511 barns for  $\pi^+$  and 0.515 barns for  $\pi^-$  production from neutron inelastic scattering on hydrogen, taken from the ENDF data in Ref [5]



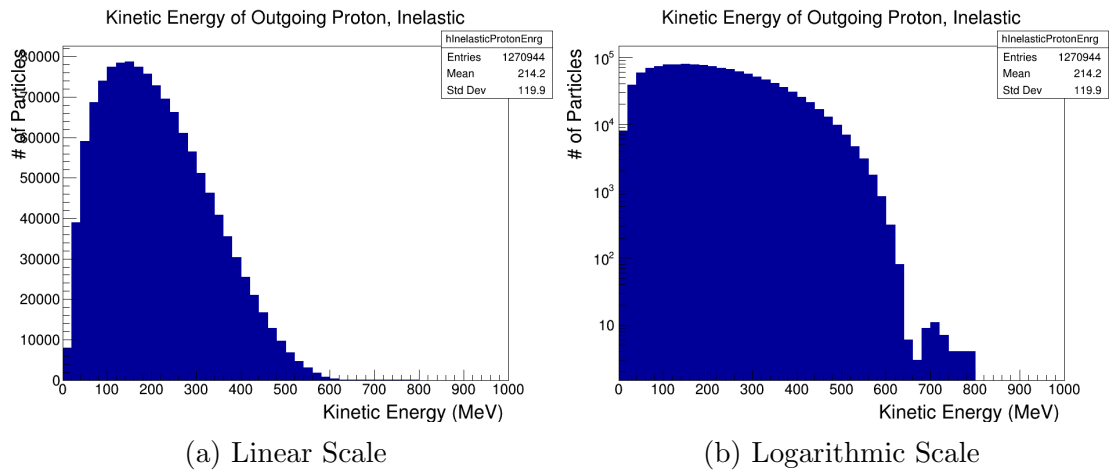


Figure 4.24. Kinetic energy of outgoing protons from neutron inelastic scattering on a hydrogen target.

We observe from Fig. 4.25 that a majority of outgoing neutrons from inelastic collisions on carbon have less than 100 MeV, and there is an exponential decrease in number of outgoing neutrons with increasing kinetic energy - as predicted by Fig. 3.6. The kinetic energy distributions for outgoing protons in Fig. 4.26 illustrates the same trend, however there is a much more gradual decrease in number of outgoing charged pions with increasing kinetic energy in Fig. 4.27; this is reasonable considering the significantly lower mass of the charged pions at  $\sim 135$  MeV when compared to the mass of the neutron at  $\sim 939$  MeV. Hence, we would expect more outgoing charged pions to have higher energies than outgoing neutrons or protons. Kinetic energies for the heavier outgoing particles scale inversely with mass as is expected from conservation of momentum, as all outgoing  $D$ 's,  ${}^3\text{He}$ 's, and  $\alpha$ 's have kinetic energies less than 660 MeV, 520 MeV and 220 MeV, respectively seen in Fig. 4.29, Fig. 4.30 and Fig. 4.31. The vast majority of these heavy outgoing particles have kinetic energies less than 20 MeV.

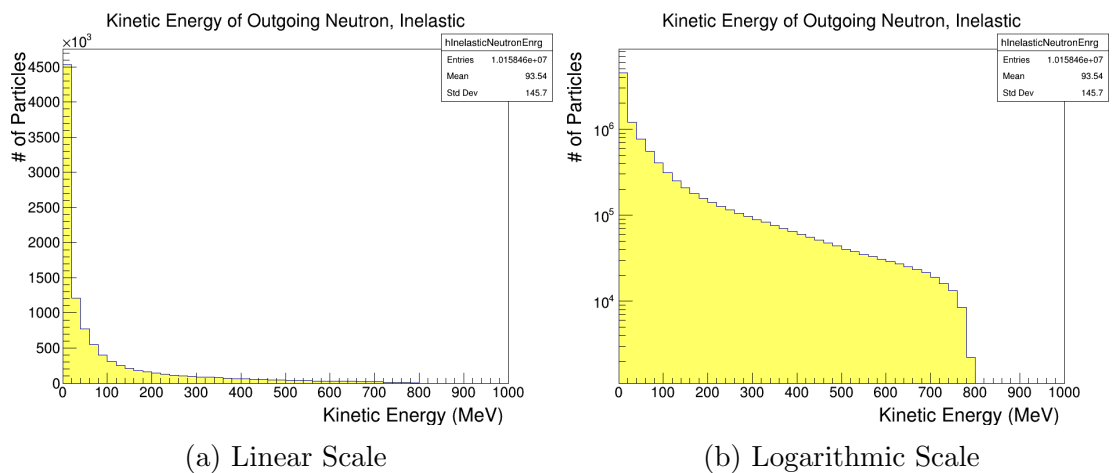


Figure 4.25. Kinetic energy of outgoing neutrons from neutron inelastic scattering on a carbon target.

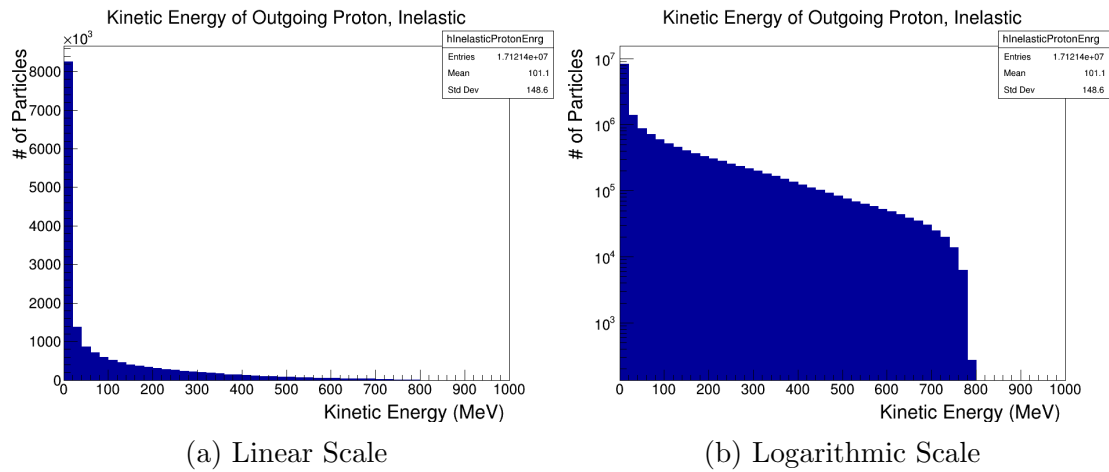


Figure 4.26. Kinetic energy of outgoing protons from neutron inelastic scattering on a carbon target.

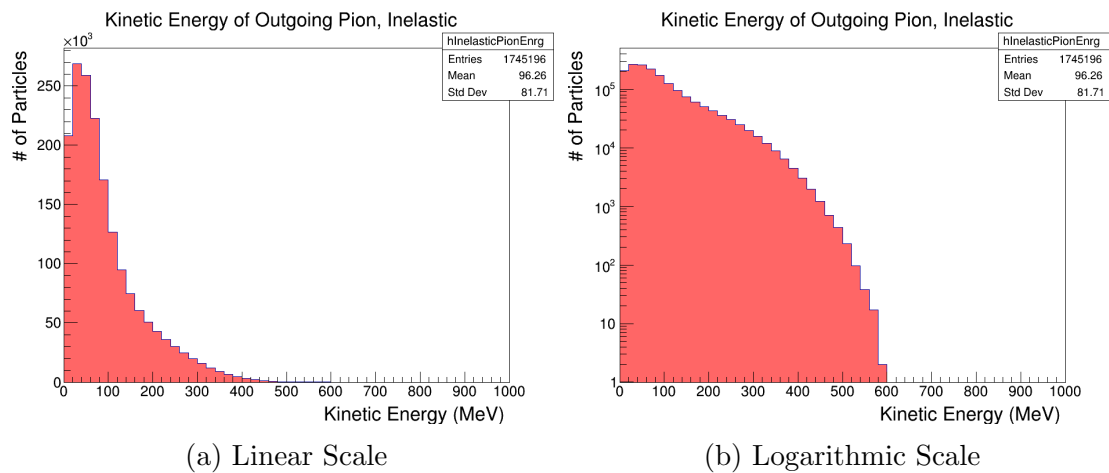


Figure 4.27. Kinetic energy of outgoing  $\pi^{\pm}$ 's from neutron inelastic scattering on a carbon target.

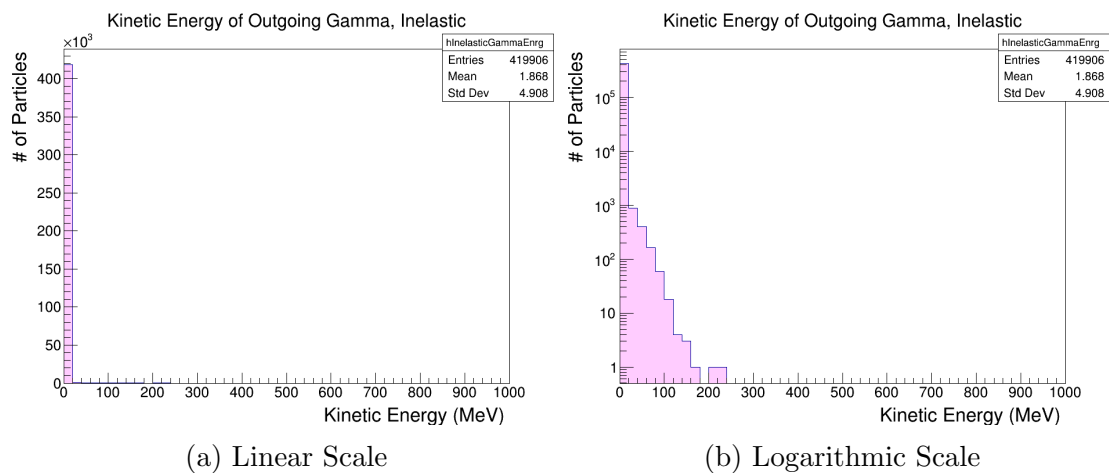


Figure 4.28. Kinetic energy of outgoing  $\gamma$ 's from neutron inelastic scattering on a carbon target.

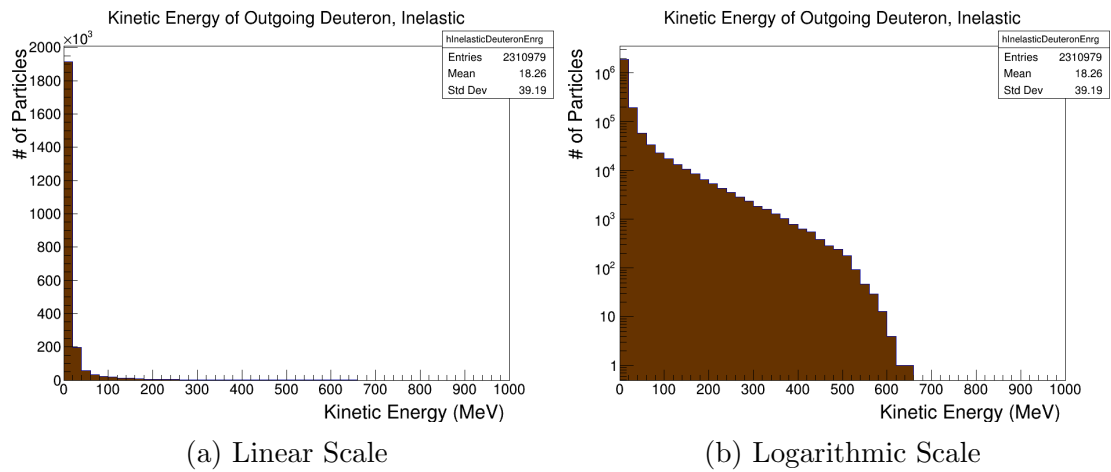


Figure 4.29. Kinetic energy of outgoing deuterons from neutron inelastic scattering on a carbon target.

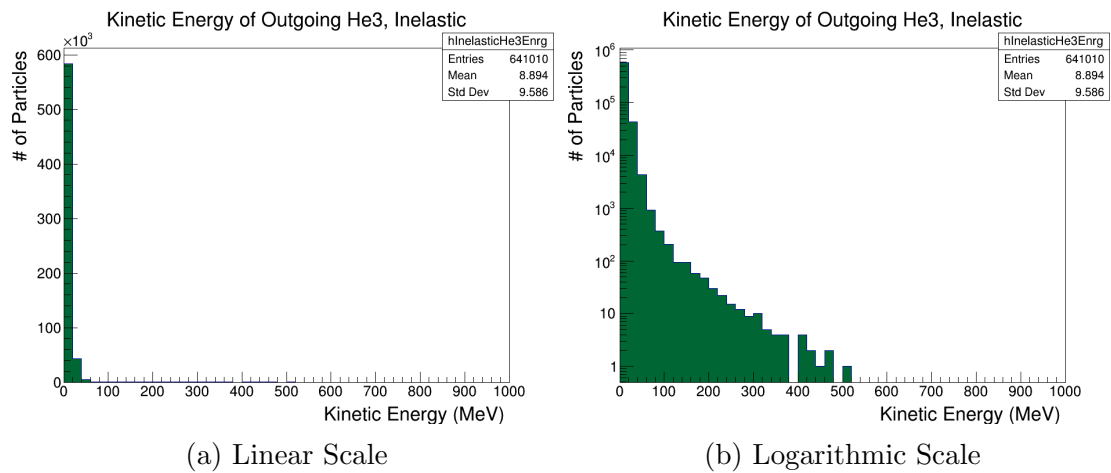


Figure 4.30. Kinetic energy of outgoing  ${}^3\text{He}$ 's from neutron inelastic scattering on a carbon target.

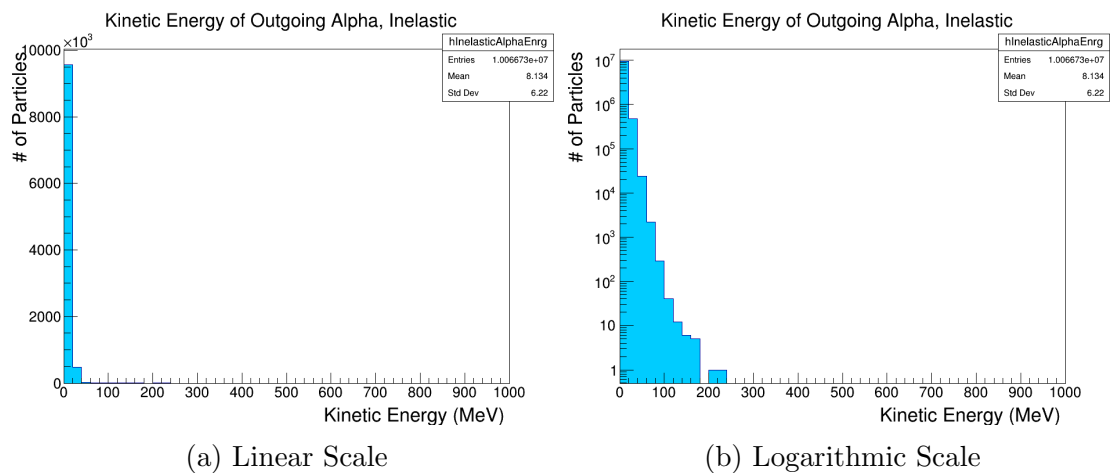


Figure 4.31. Kinetic energy of outgoing  $\alpha$ 's from neutron inelastic scattering on a carbon target.

Fig. 4.32 shows the stacked histograms for the true kinetic energy of the outgoing particles from inelastic collisions of neutrons on a CH target. The kinetic energy distribution for carbon has been omitted from Fig. 4.32 as the kinetic energy was calculated by subtracting the mass from the total energy of the outgoing particles, and since we have marked all isotopes of carbon from  ${}^8\text{C}$  to  ${}^{13}\text{C}$  as “carbon” without distinction it would be inaccurate to subtract the mass of  ${}^{12}\text{C}$  from all outgoing carbons. The majority of inelastic scattering events for neutron interactions on hydrocarbon occur due to neutron inelastic scattering on carbon, hence the features of neutron inelastic scattering on carbon dominate in the appearance of neutron inelastic scattering on hydrocarbon. Therefore, the structure of the stacked histogram resembles Fig. 3.6. Hence, we are able to understand the features of Fig. 4.32 from the understanding of kinetic energy distributions of outgoing particles from neutron inelastic scattering on hydrogen and carbon targets.

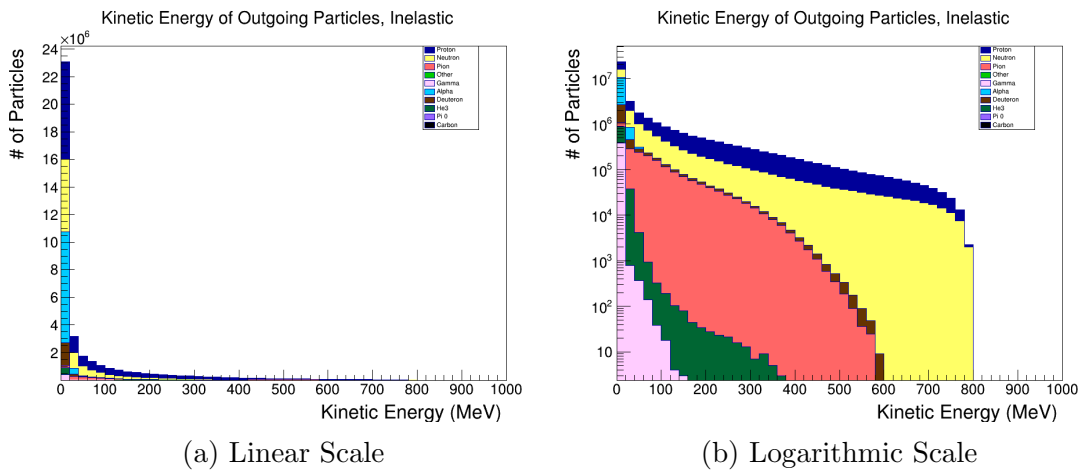


Figure 4.32. Stacked kinetic energy distributions of outgoing particles from inelastic neutron interactions on hydrocarbon. Different colours indicate different particle types.

From relativistic particle kinematics, we know

$$E^2 = p^2 + m^2 \quad (4.3)$$

where  $E$ ,  $p$ , and  $m$  are the total energy, momentum, and mass of a given particle. We re-arrange to see:

$$|p| = \sqrt{E^2 - m^2} = \sqrt{(E - m)(E + m)} \quad (4.4)$$

Therefore, considering kinetic energy was computed as the difference between the total energy and the mass, we can conclude that the shape and structure of the momentum plots should represent the kinetic energy plots with a “horizontal squeeze”<sup>4</sup> proportional to the  $m^2$  of each particle. This is what we observe; Fig. 4.26 shows a sharp drop in number of outgoing protons with kinetic energies greater than 20 MeV, and we see a similar sharp drop in number of outgoing protons with momenta greater than 150 MeV in Fig. 4.35. The shape of Fig. 4.26

<sup>4</sup>shift along the horizontal axis (in this case, momentum) and broadening of the distribution

resembles that of Fig. 4.26 which has been shifted along the x axis and broadened slightly. We can get a sense of the magnitude of this transformation by observing how the mean and standard deviation of the kinetic energy distributions differ from the mean and standard deviations of the momentum distributions; for the outgoing protons the mean of Fig. 4.35  $\approx 2.4$  times greater than the mean of Fig. 4.26, and the standard deviation for Fig. 4.35 is  $\approx 1.1$  times greater than the standard deviation of Fig. 4.26. Similarly, Fig. 4.34 has a gradual decrease in number of outgoing charged pions with kinetic energy greater than 150 MeV, resembling the decrease in number of outgoing charged pions with momenta greater than 250 MeV in Fig. 4.27, although the shift in shape is not as apparent as it is in the distributions for the protons due to the lower mass of the charged pions. The mean and standard deviations of the momentum distribution are  $\approx 0.9$  and  $\approx 0.2$  times higher than those of the kinetic energy distributions, respectively. To consider a case of extremes, note the decrease in number of outgoing  $\alpha$ 's with kinetic energy greater than 40 MeV by two orders of magnitude in Fig. 4.39, and compare it to the significantly more gradual decrease in the number of outgoing  $\alpha$ 's with momenta greater than 250 MeV in Fig. 4.31. The mean and standard deviations of the momentum distribution are  $\approx 26.4$  and  $\approx 13.2$  times higher than those of the kinetic energy distributions, respectively. The momenta distributions for outgoing particles from inelastic interactions on carbon and hydrogen have been presented here in order of increasing mass, with analyses of interactions on carbon presented first. Though this provides a general qualitative explanation for the trend in shape of the momentum distributions, a more concretely qualitative reasoning requires further investigation.

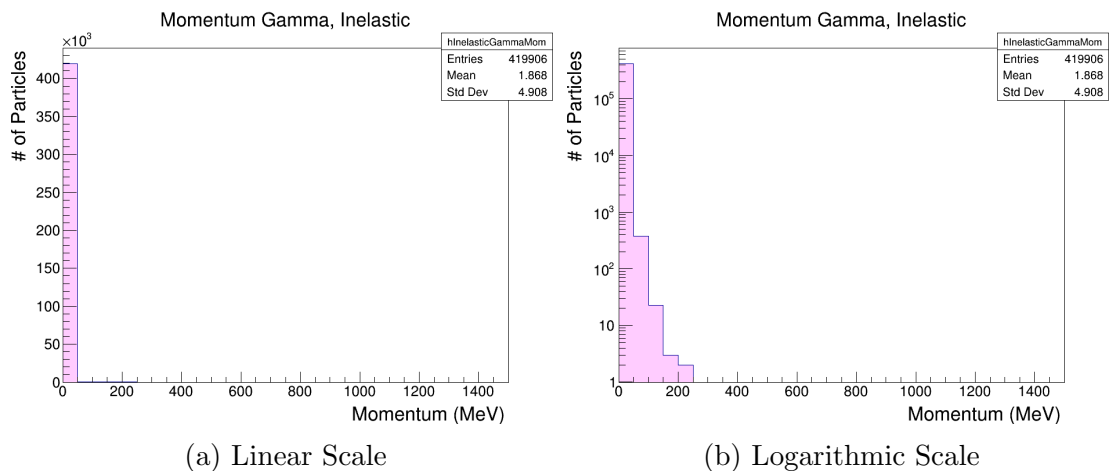


Figure 4.33. Momentum of outgoing  $\gamma$ 's from neutron inelastic scattering on a carbon target.

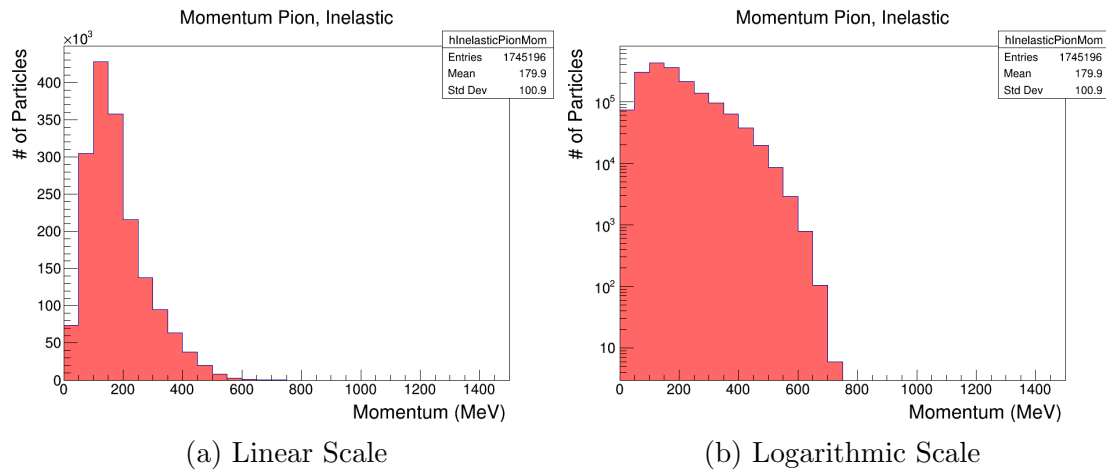


Figure 4.34. Momentum of outgoing  $\pi^\pm$ 's from neutron inelastic scattering on a carbon target.

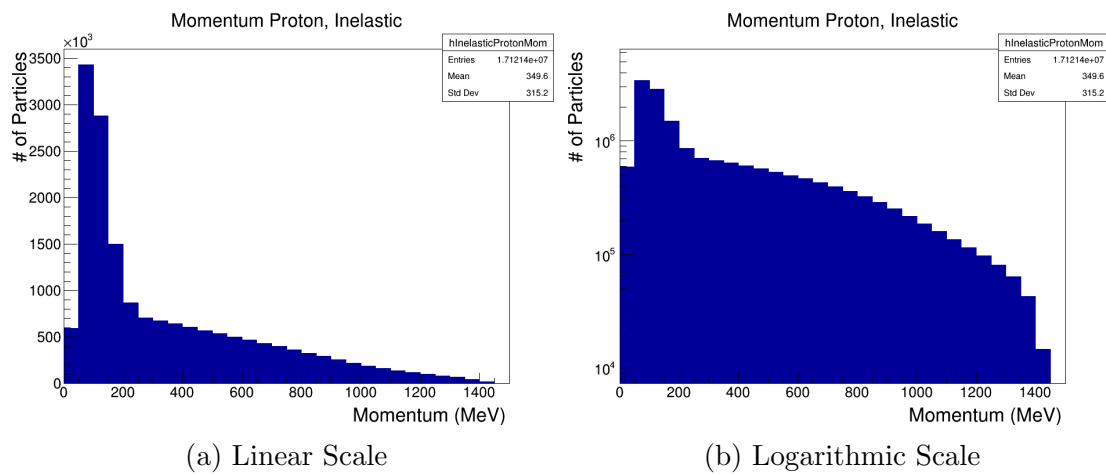


Figure 4.35. Momentum of outgoing protons from neutron inelastic scattering on a carbon target.

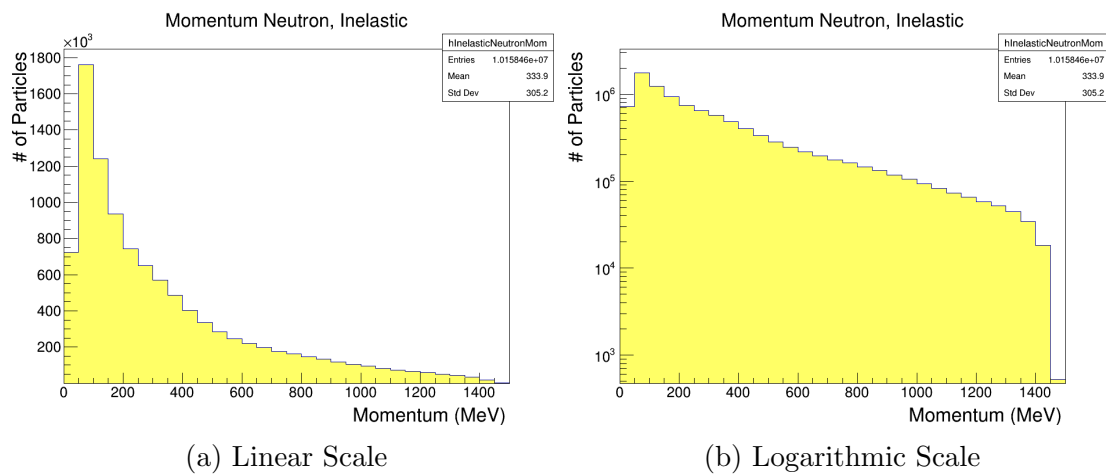


Figure 4.36. Momentum of outgoing neutrons from neutron inelastic scattering on a carbon target.

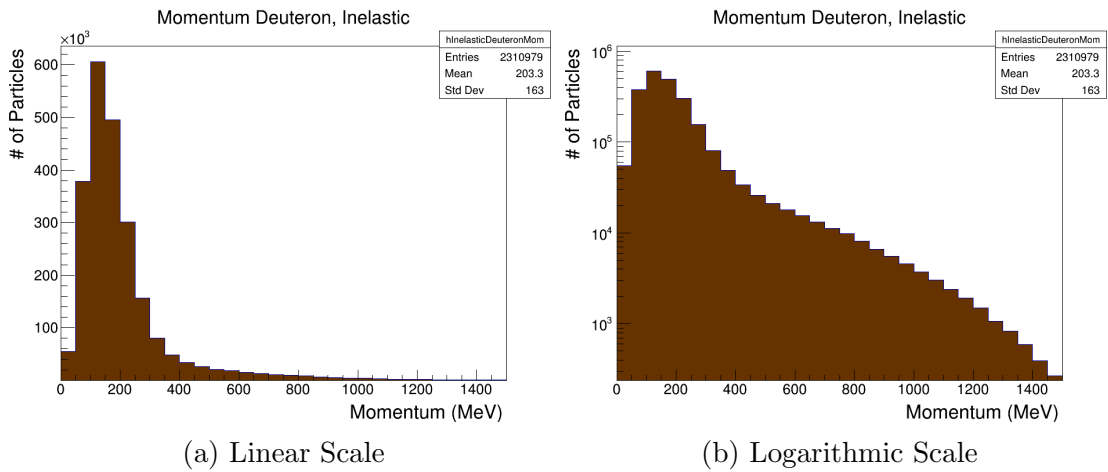


Figure 4.37. Momentum of outgoing deuterons from neutron inelastic scattering on a carbon target.

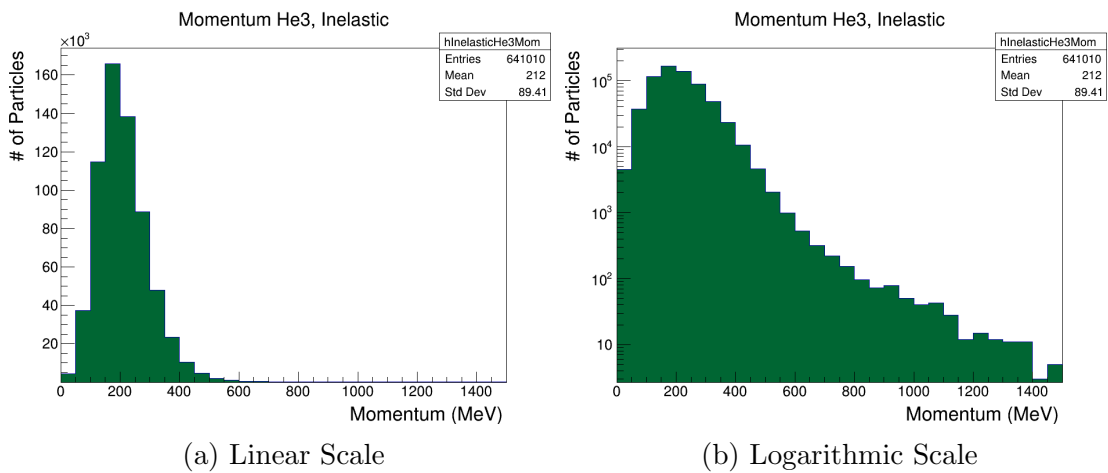


Figure 4.38. Momentum of outgoing  ${}^3\text{He}$ 's from neutron inelastic scattering on a carbon target.

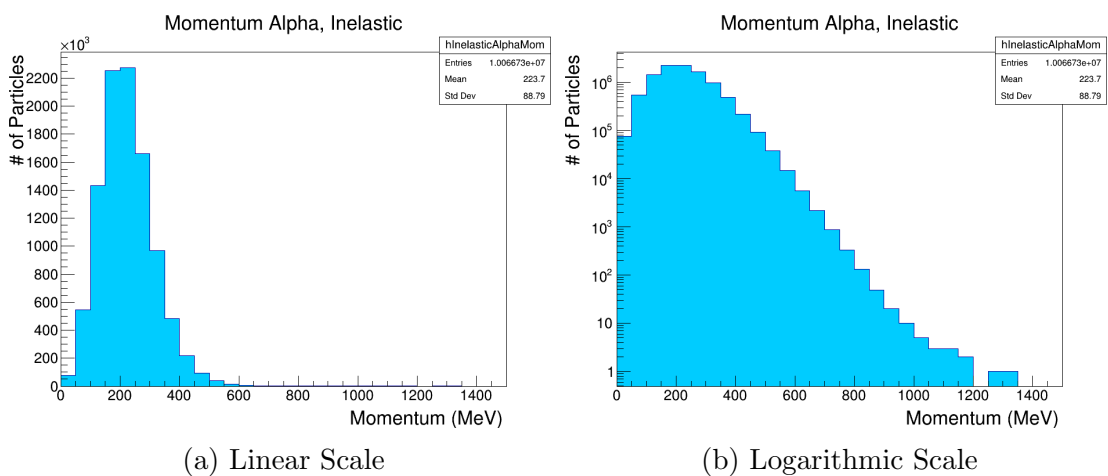


Figure 4.39. Momentum of outgoing  $\alpha$ 's from neutron inelastic scattering on a carbon target.

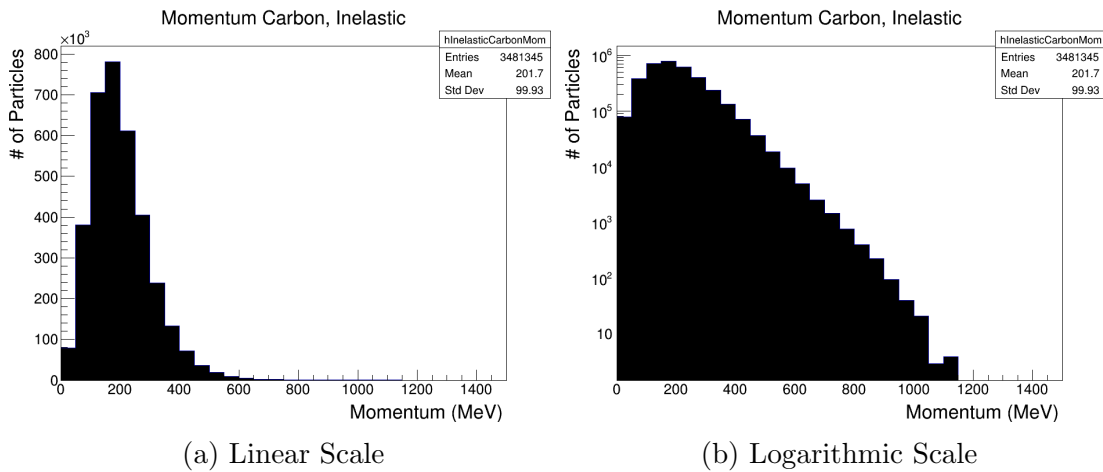


Figure 4.40. Momentum of outgoing carbons from neutron inelastic scattering on a carbon target.

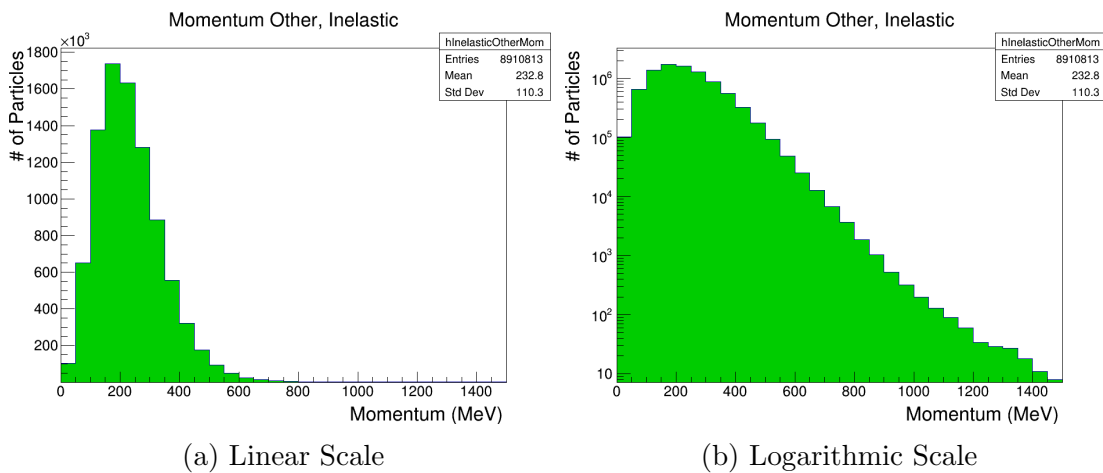


Figure 4.41. Momentum of outgoing 'others' from neutron inelastic scattering on a carbon target.

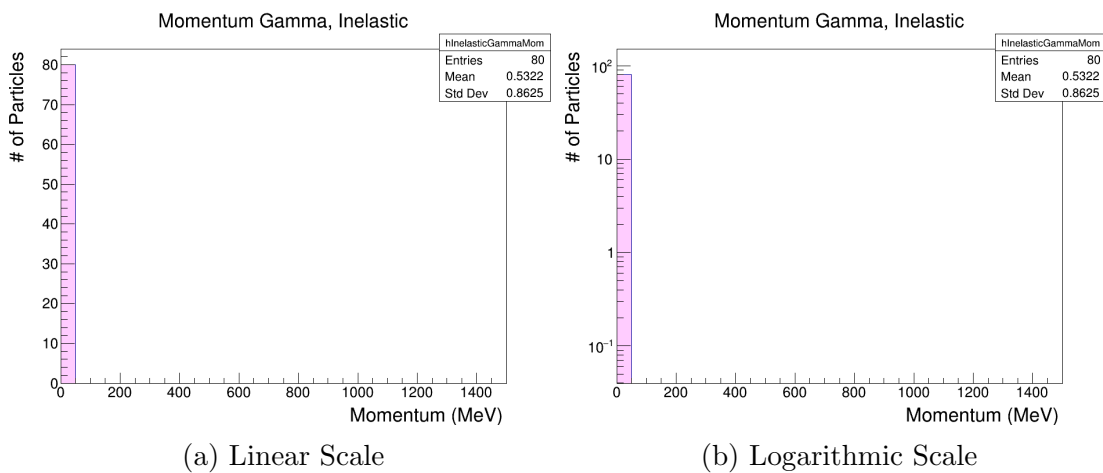


Figure 4.42. Momentum of outgoing  $\gamma$  from neutron inelastic scattering on a hydrogen target.



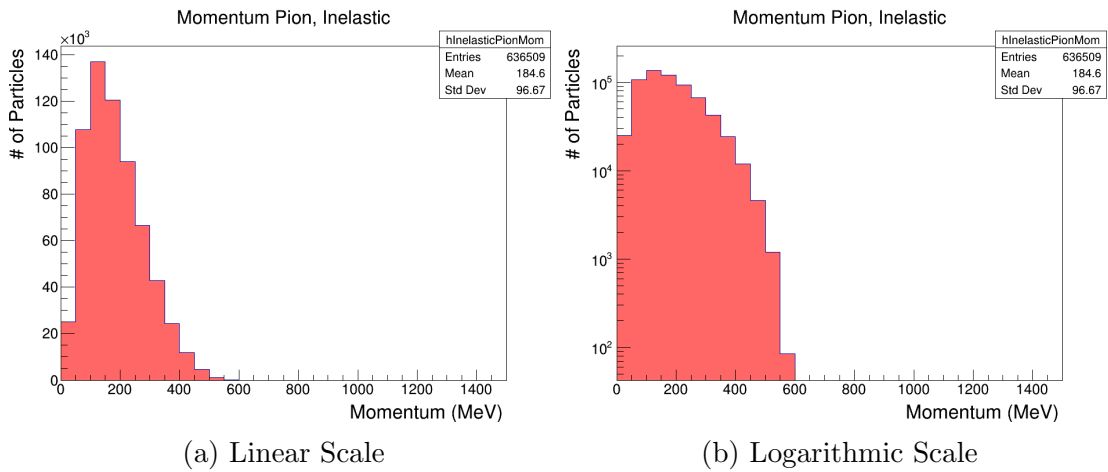


Figure 4.43. Momentum of outgoing  $\pi^\pm$ 's from neutron inelastic scattering on a hydrogen target.

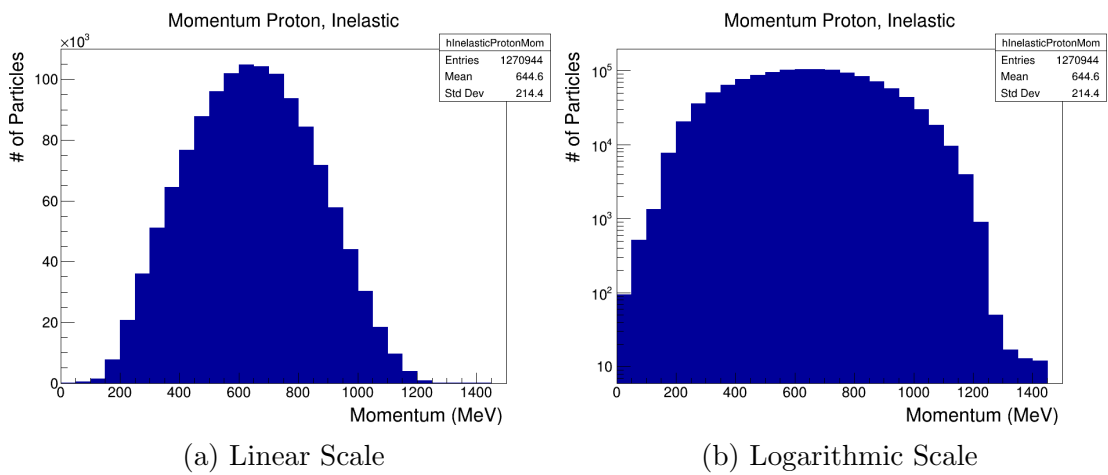


Figure 4.44. Momentum of outgoing protons from neutron inelastic scattering on a hydrogen target.

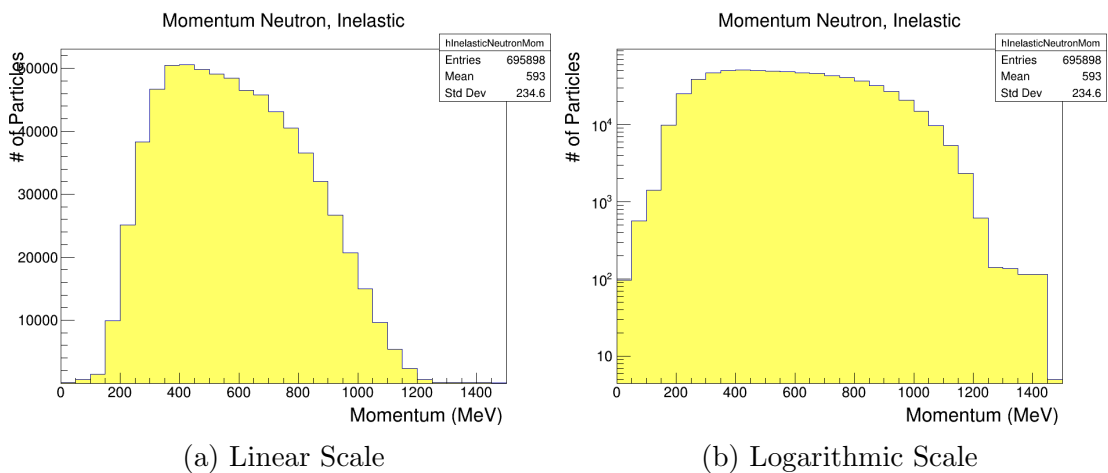


Figure 4.45. Momentum of outgoing neutrons from neutron inelastic scattering on a hydrogen target.

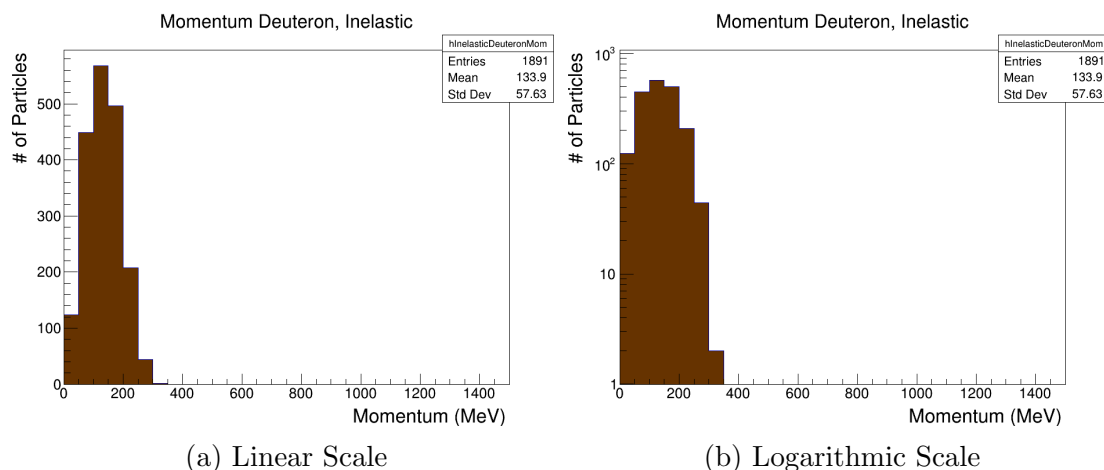


Figure 4.46. Momentum of outgoing deuterons from neutron inelastic scattering on a hydrogen target.

Stacked histograms for the momenta of outgoing particles from inelastic scattering of neutrons on hydrocarbon are presented in Fig. 4.47. Since the majority of inelastic scattering events for neutrons interacting with a CH target occur from scattering on carbon, the features from scattering on carbon (Fig. 4.18b) dominate over features from scattering on hydrogen (Fig. 4.18a).

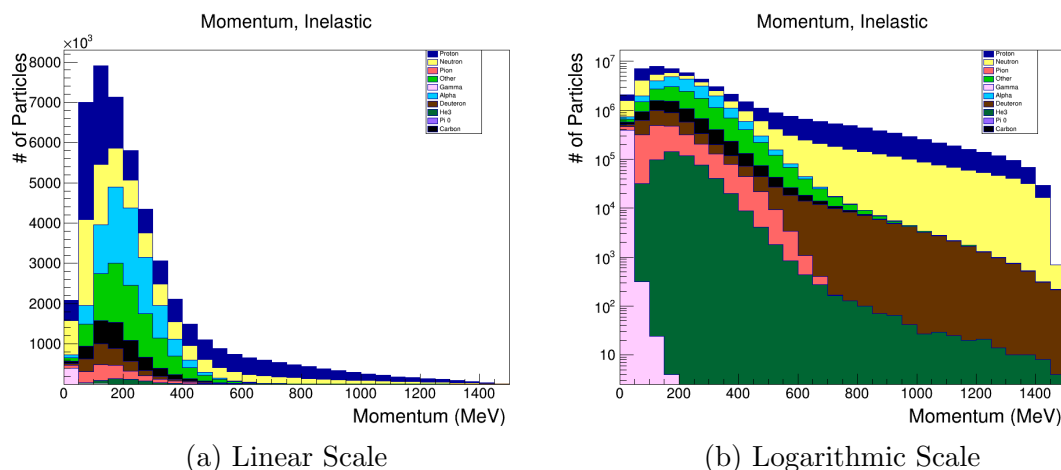
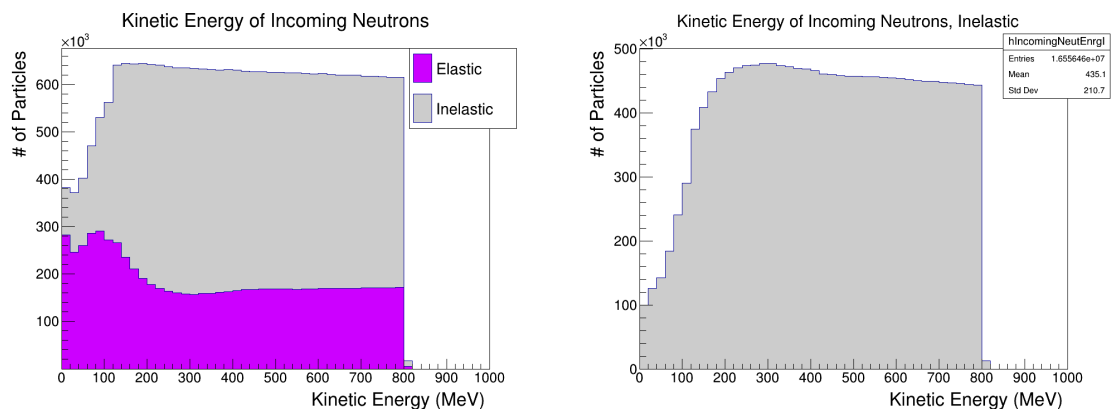


Figure 4.47. Stacked momentum distributions of outgoing particles from inelastic neutron interactions on hydrocarbon. Different colours indicate different particle types.

The dependence of  $\theta$  on the momentum of the particle from Eq. (4.1) implies that verification of our analyses on momenta verifies our analyses on  $\theta$ . The majority of these distributions are provided in the appendix for brevity, as they illustrate similar features. The mean value of the  $\theta$  distribution for outgoing neutrons in Fig. 4.49 is notably skewed towards lower  $\theta$  than the  $\theta$  distribution for outgoing protons in Fig. C.2 in spite of a similar mass, likely due to the contribution of outgoing neutrons from  $n+^{12}\text{C}\rightarrow n+^{12}\text{C}+\gamma$  interactions. Recall that the De Broglie wavelength decreases with increasing momenta and thereby with increasing energy, and as the De Broglie wavelength decreases to the nucleon-nucleon scale we begin to see inelastic interactions. The  $\theta$  distribution for outgoing carbons in Fig. 4.50



(a) Stacked histogram of kinetic energies of incoming neutrons which interact inelastically and elastically, linear Scale.

(b) Kinetic energies of incoming neutrons which interact inelastically, logarithmic Scale.

Figure 4.48. Stacked histogram of incoming neutron energies interacting with carbon elastically and inelastically.

shows a distinct peak around  $80^\circ$  with a relatively sharp drop off around  $\theta \approx 90^\circ$ , followed by a gradual decrease in number of outgoing carbons with increasing  $\theta$ . The ENDF does not provide data for nonelastic interactions of neutrons on  $^{12}\text{C}$  cross sections as a function of angle, therefore we evaluate possible interaction channels for a likely explanation. If we have a neutron inelastically scattering on carbon and one of the outgoing particles is a carbon, the interaction channel is likely  $n + ^{12}\text{C} \rightarrow n + ^{12}\text{C} + \gamma$ . From the point of view of the masses involved, this is very similar to elastic scattering as seen in Fig. 4.7, which is why we observe a similar spike near  $90^\circ$  in Fig. 4.50. This makes sense given that the  $\gamma$  has no mass. Although, given that CoM energy is not conserved in inelastic interactions we note that it is possible - though not as likely - that an outgoing carbon can have  $\theta > 90^\circ$ , explaining the gradual decrease in number of outgoing carbons with increasing  $\theta$  greater than  $90^\circ$ . Furthermore, Fig. 4.51 illustrates the  $\theta$  for outgoing gammas from inelastic neutron scattering off carbons and resembles an isotropic distribution centered at  $90^\circ$ . This is exactly what we would expect given that the photon has no mass.

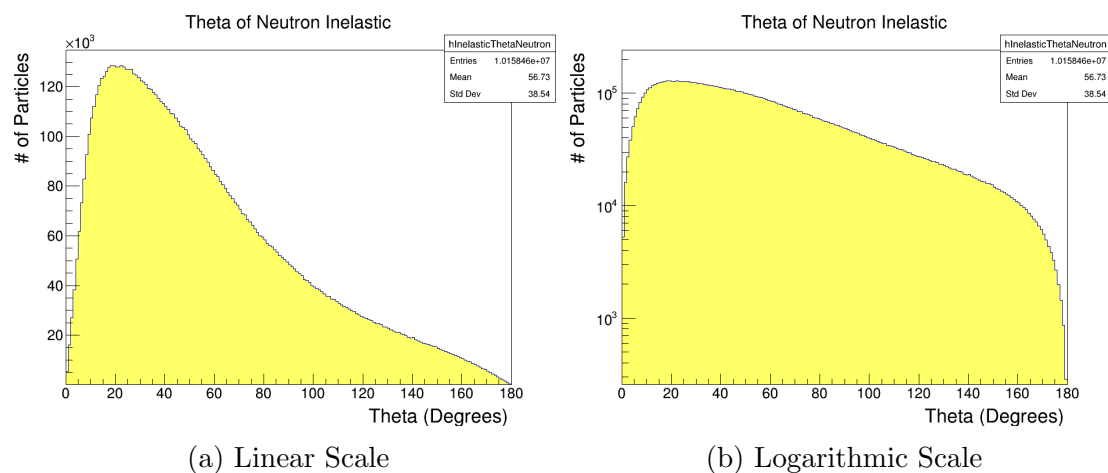


Figure 4.49.  $\theta$  of outgoing neutrons from neutron inelastic scattering on a carbon target.

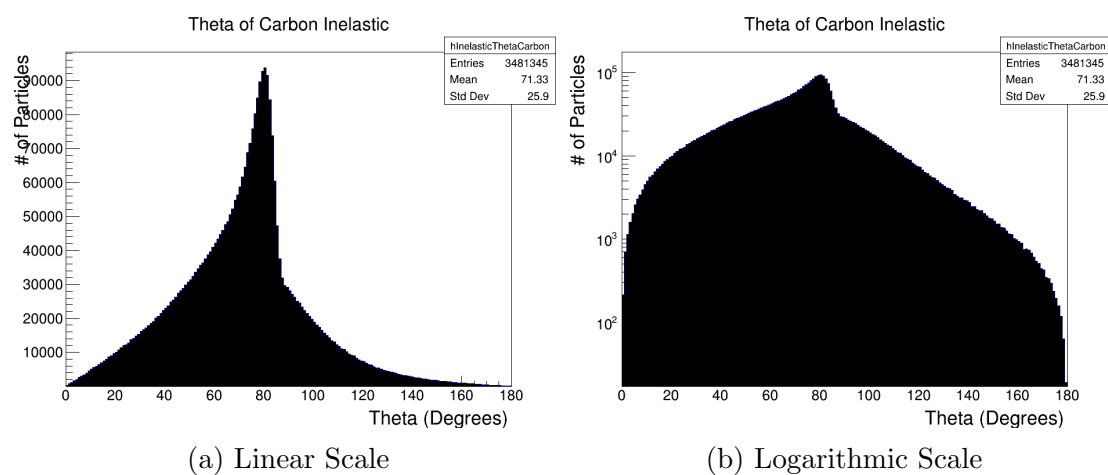


Figure 4.50.  $\theta$  of outgoing carbons from neutron inelastic scattering on a carbon target.

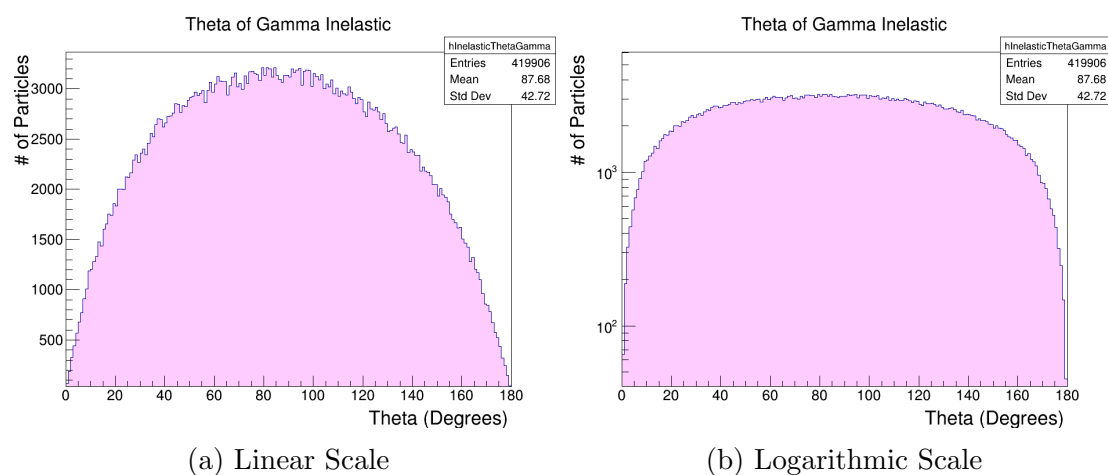


Figure 4.51.  $\theta$  of outgoing  $\gamma$ 's from neutron inelastic scattering on a carbon target.

By combining the  $\theta$  distributions for inelastic scattering on carbon and hydrogen, we are able to understand the features of the  $\theta$  distribution for inelastic scattering on CH given by Fig. 4.52. Note that the distribution is heavily dominated by the inelastic scattering of neutrons on carbon as seen in Fig. C.15, as there appears to be no visibly noticeable contribution from the inelastic scattering of neutrons on hydrogen as seen in Fig. C.14. This corroborates that the total integrated cross section for neutron inelastic scattering on carbon is an order of magnitude higher than for inelastic scattering on hydrogen<sup>5</sup>.

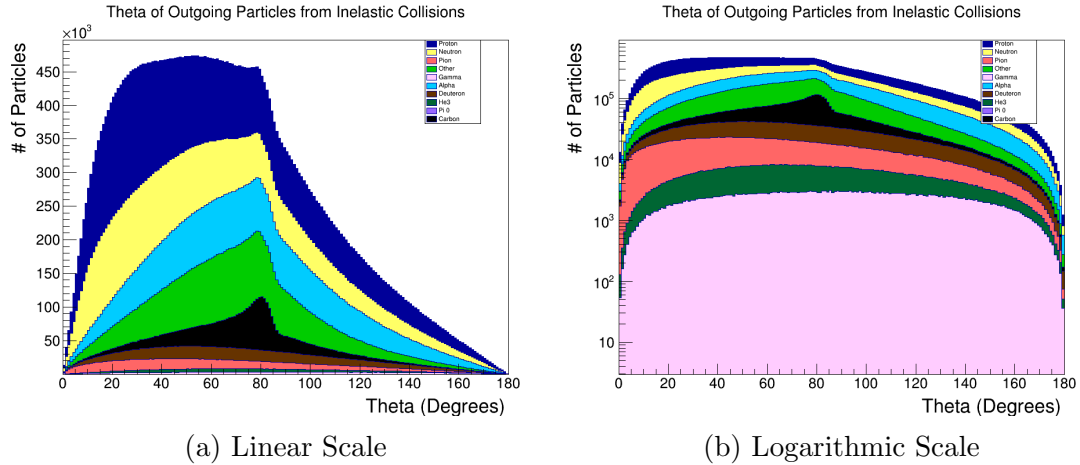


Figure 4.52. Angle relative to beam ( $\theta$ ) of outgoing neutrons from inelastic scattering of neutrons on a Hydrocarbon target.

## 4.5 Model Comparisons

The analysis presented in the preceding section was performed on MC files created using the BERTINI Physics list. The analysis was run over MC files generated using different physics lists (BERTINI HP and INCLXX) to verify the validity of the analysis conducted on MC files generated using the BERTINI physics list, and to investigate how different cascade models affected the analysis. **All plots generated in this section were done for neutron interactions on a hydrocarbon target, unless stated otherwise.**

Each of the non-stacked histograms were area normalized and plotted on the same canvas for comparison, and it was found that the analyses using each physics list produced results either identical or in very high agreement with each other for the majority of elastic scattering distributions. Only one example of such a distribution shall be presented here, as we use this section to highlight notable differences and features. All other relevant histograms are presented in the appendix. The main difference between the physics lists are how they handle intranuclear cascades, therefore an emphasis on the analyses of inelastic collisions of neutrons with hydrocarbon will be explored.

<sup>5</sup>Taken from ENDF data Ref [5]

Fig. 4.53 illustrates the kinematics of the outgoing proton from elastic collisions. As we can see, there is a high degree of agreement between the analyses conducted on all 3 physics lists. There is a notably larger number of entries in the 0-20 MeV range for the analyses of kinetic energy conducted on the BERTINI files than on the BERTINI HP and INCLXX files. Such differences between the BERTINI and BERTINI HP is expected since BERTINI HP is an extension of BERTINI below 20 MeV. There are also notable differences in 50-250 MeV range for the momentum of the outgoing protons as seen in Fig. 4.53a. Moreover, we see similar agreements between different physics lists for the kinematics of the outgoing carbons from elastic collisions as can be seen in Fig. 4.55. Although the  $\theta$  distributions for outgoing neutrons in Fig. 4.54 share nearly identical distributions between the 3 physics lists, Fig. 4.54a and Fig. 4.54b illustrate different structures between the INCLXX and BERTINI physics lists.

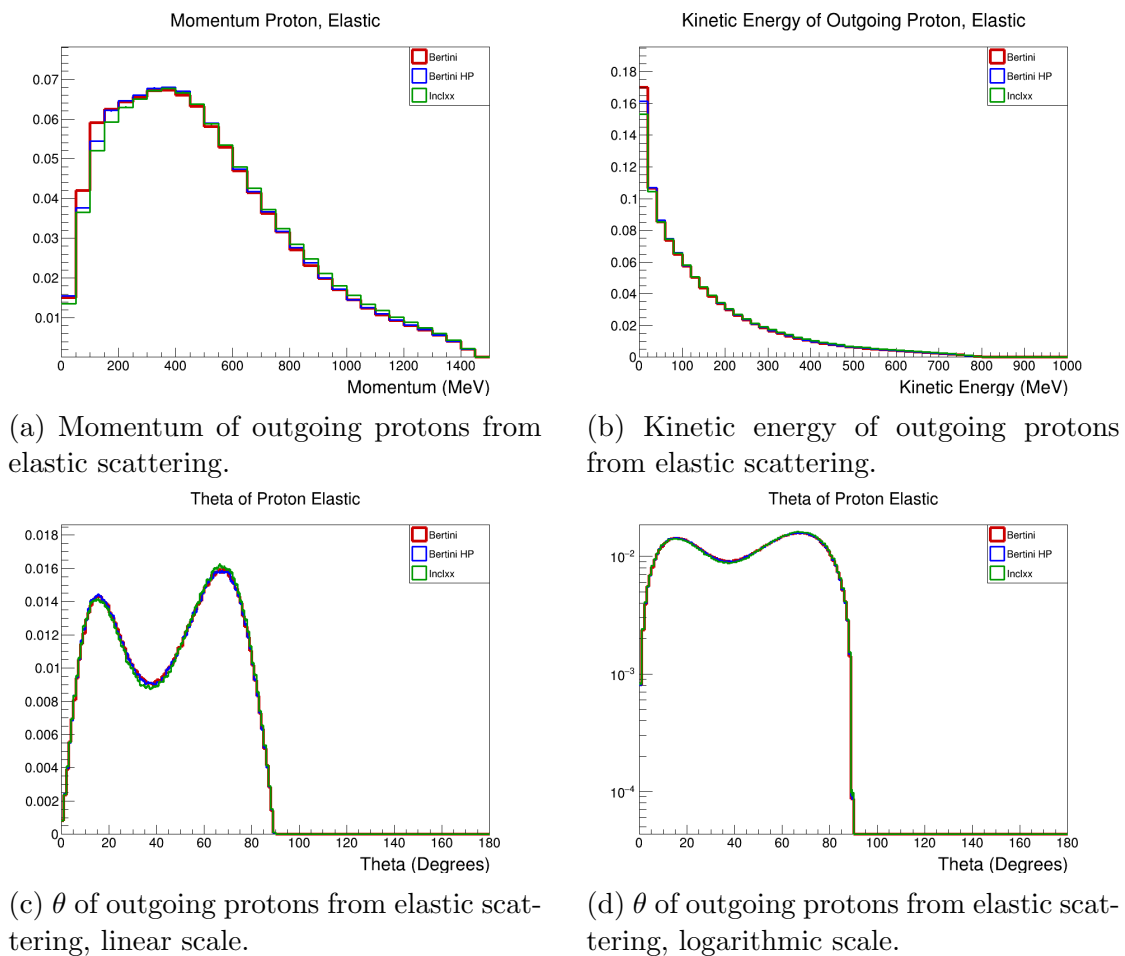
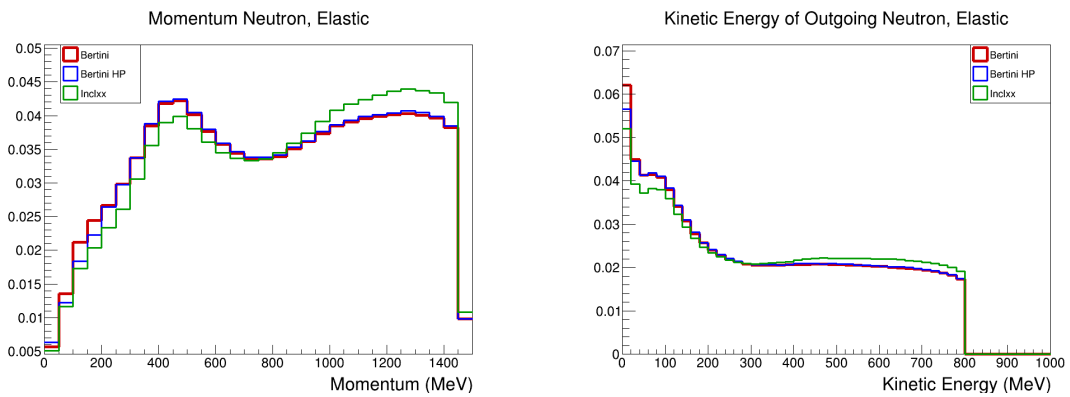


Figure 4.53. Comparison distributions for the kinematics of outgoing protons from elastic collisions. Each line colour represents data produced by a different physics list. The histograms in these plots have been area normalized. The bottom right plot shows the data from the bottom left plot on a logarithmic y-axis scale. The top left plot shows the momentum distributions and the top right plot shows the kinetic energy distributions.

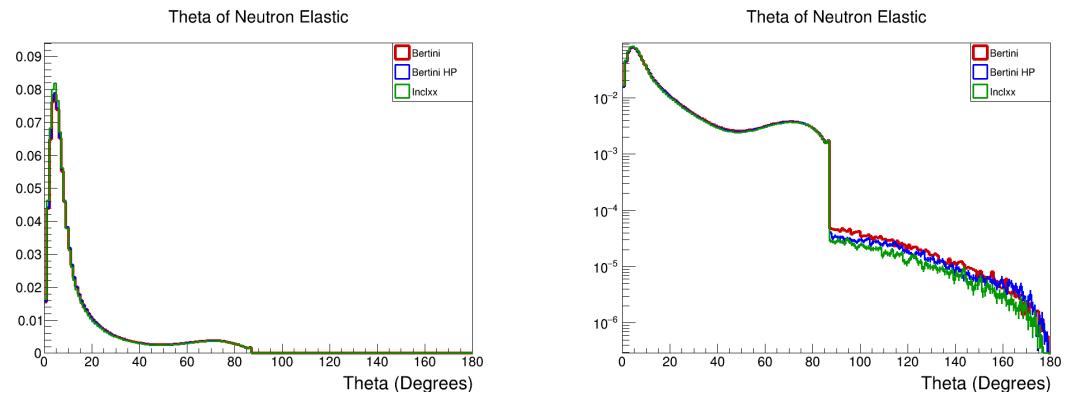
We start to see noticeable differences between the analyses on the physics lists when viewing the kinematics from inelastic collisions; particularly those of the

outgoing protons (Fig. 4.56) and charged pions (Fig. 4.57). We see in the momentum and kinetic energy distributions for both of these particle types that the shapes of the distributions created by the analysis using the INCLXX physics list is entirely different from the BERTINI and BERTINI HP physics lists. The most apparent difference between the INCLXX and BERTINI physics lists is presented in Fig. 4.58. We expect these significant differences, as the BERTINI physics list uses the Fermi Gas model, assuming the medium through which the incident neutron travels is a gas under the assumption that the nucleon size is small relative to the medium. However, the INCLXX physics list uses the Leige Intranuclear Cascade model, meaning that it is better suited to modelling intranuclear processes. Since inelastic interactions of neutron on carbon heavily involve such intranuclear processes and dominate inelastic interactions of neutron on CH, it is reasonable to expect that we would see considerable differences between the BERTINI and INCLXX models reflected in kinematics of inelastic neutron scattering off CH. Subsequently, we observe differences in the kinematics for all outgoing particles from inelastic interactions, as can be seen in the remaining figures in this chapter.



(a) Momentum of outgoing neutrons from elastic scattering.

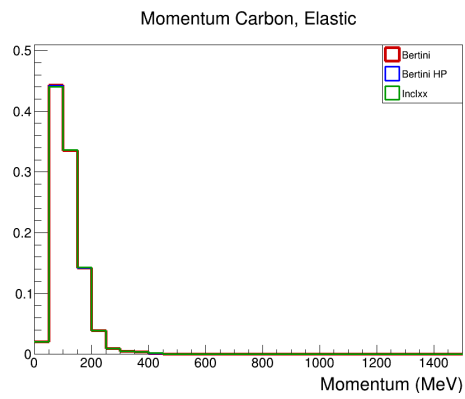
(b) Kinetic energy of outgoing neutrons from elastic scattering.



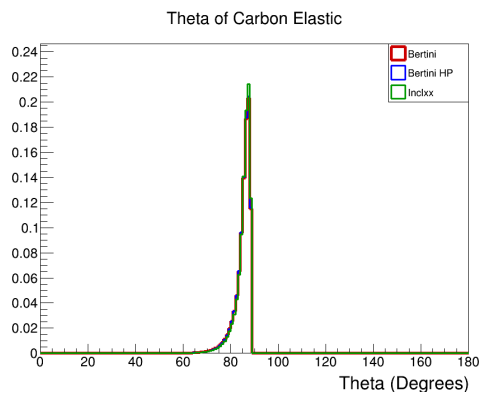
(c)  $\theta$  of outgoing neutrons from elastic scattering, linear scale.

(d)  $\theta$  of outgoing neutrons from elastic scattering, logarithmic scale.

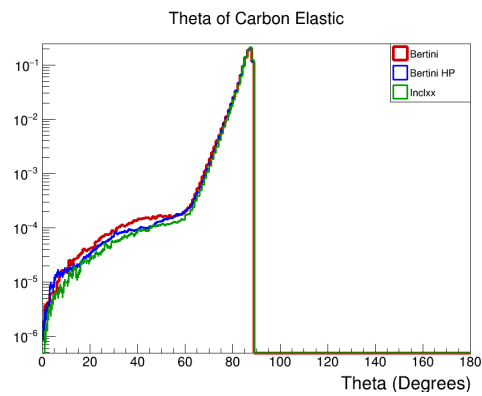
Figure 4.54. Comparison distributions for the kinematics of outgoing neutrons from elastic collisions. Each line colour represents data produced by a different physics list. The histograms in these plots have been area normalized. The bottom right plot shows the data from the bottom left plot on a logarithmic y-axis scale. The top left plot shows the momentum distributions and the top right plot shows the kinetic energy distributions.



(a) Momentum of outgoing carbons from elastic scattering, linear scale.



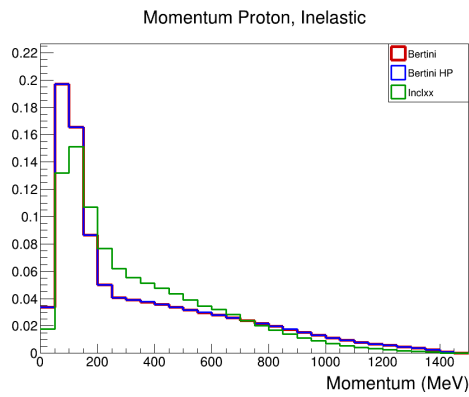
(b)  $\theta$  of outgoing carbons from elastic scattering, linear scale.



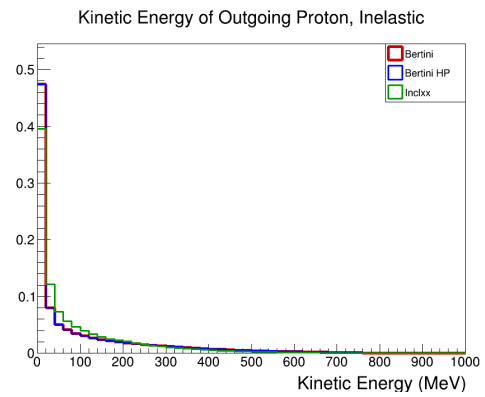
(c)  $\theta$  of outgoing carbons from elastic scattering, logarithmic scale.

Figure 4.55. Comparison distributions for the kinematics of outgoing carbons from elastic collisions. Each line colour represents data produced by a different physics list. The histograms in these plots have been area normalized. The bottom right plot shows the data from the bottom left plot on a logarithmic y-axis scale. The top plot shows the momentum distributions.





(a) Momentum of outgoing protons from inelastic scattering.



(b) Kinetic energy of outgoing protons from inelastic scattering.

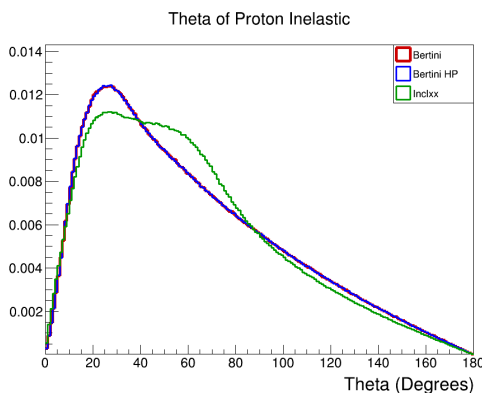
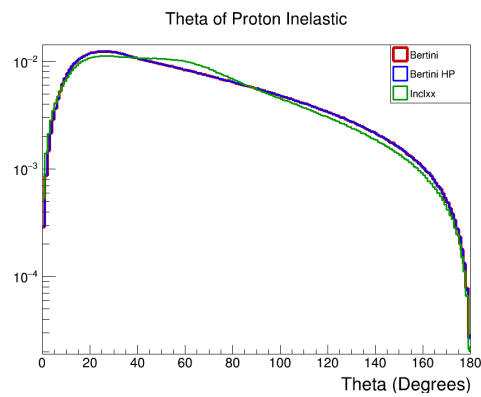
(c)  $\theta$  of outgoing protons from inelastic scattering, linear scale.(d)  $\theta$  of outgoing protons from inelastic scattering, logarithmic scale.

Figure 4.56. Comparison distributions for the kinematics of outgoing protons from inelastic collisions. Each line colour represents data produced by a different physics list. The histograms in these plots have been area normalized. The bottom right plot shows the data from the bottom left plot on a logarithmic y-axis scale. The top left plot shows the momentum distributions and the top right plot shows the kinetic energy distributions.

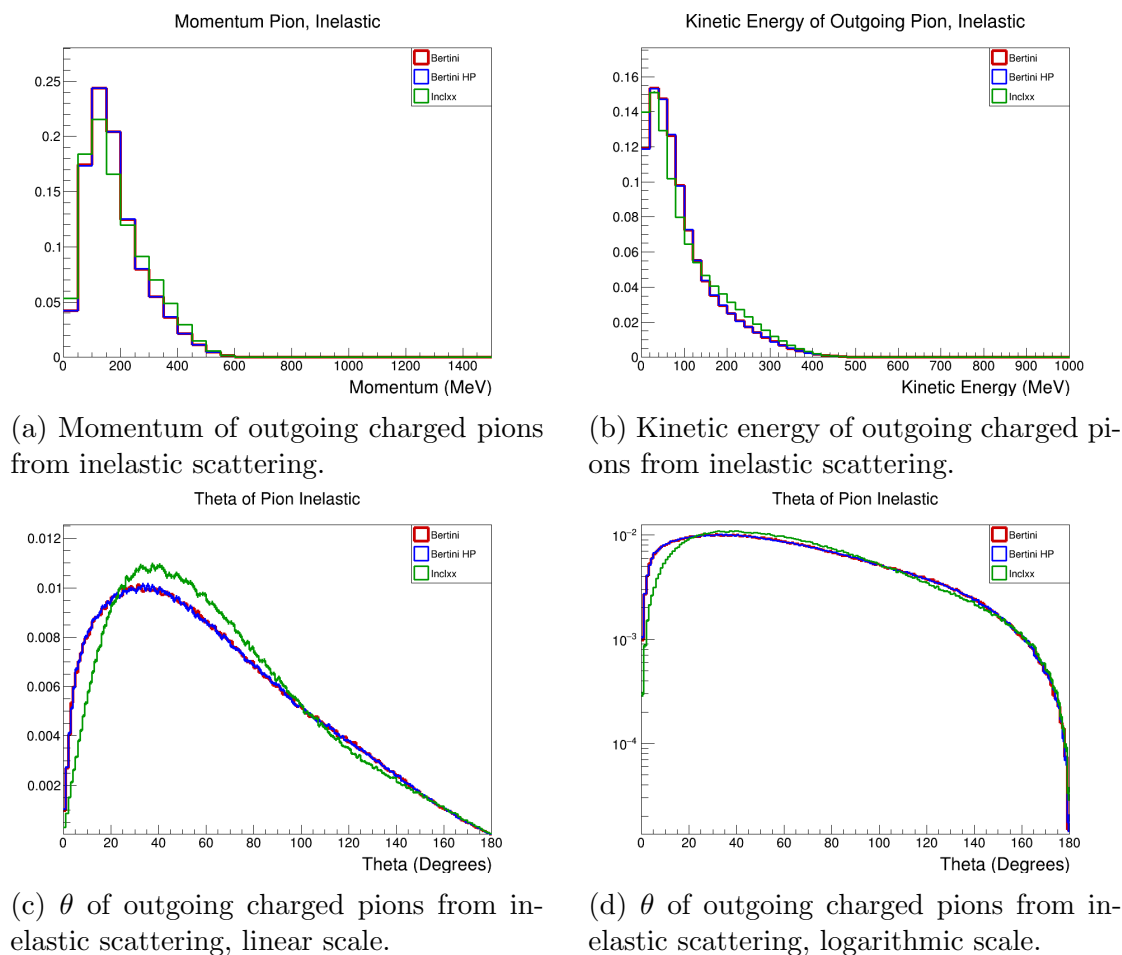
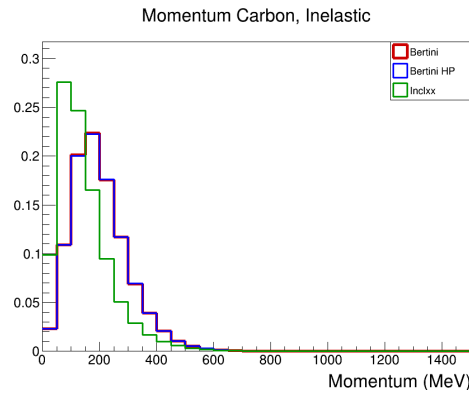
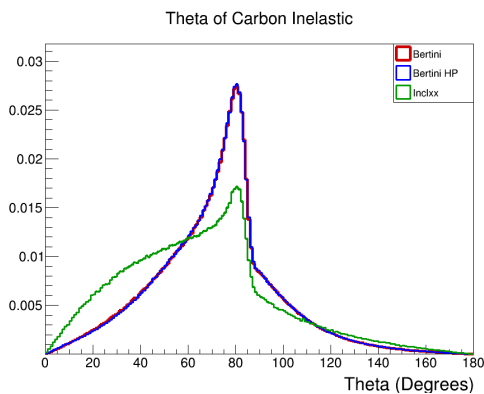


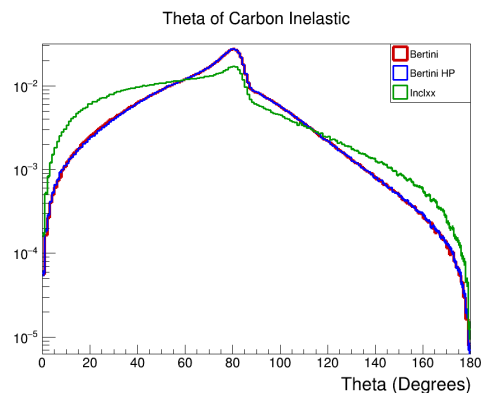
Figure 4.57. Comparison distributions for the kinematics of outgoing charged pions from inelastic collisions. Each line colour represents data produced by a different physics list. The histograms in these plots have been area normalized. The bottom right plot shows the data from the bottom left plot on a logarithmic y-axis scale. The top left plot shows the momentum distributions and the top right plot shows the kinetic energy distributions.



(a) Momentum of outgoing carbons from inelastic scattering.



(b)  $\theta$  of outgoing carbons from inelastic scattering, linear scale.



(c)  $\theta$  of outgoing carbons from inelastic scattering, logarithmic scale.

Figure 4.58. Comparison distributions for the kinematics of outgoing carbons from inelastic collisions. Each line colour represents data produced by a different physics list. The histograms in these plots have been area normalized. The bottom right plot shows the data from the bottom left plot on a logarithmic y-axis scale. The top plot shows the momentum distributions.

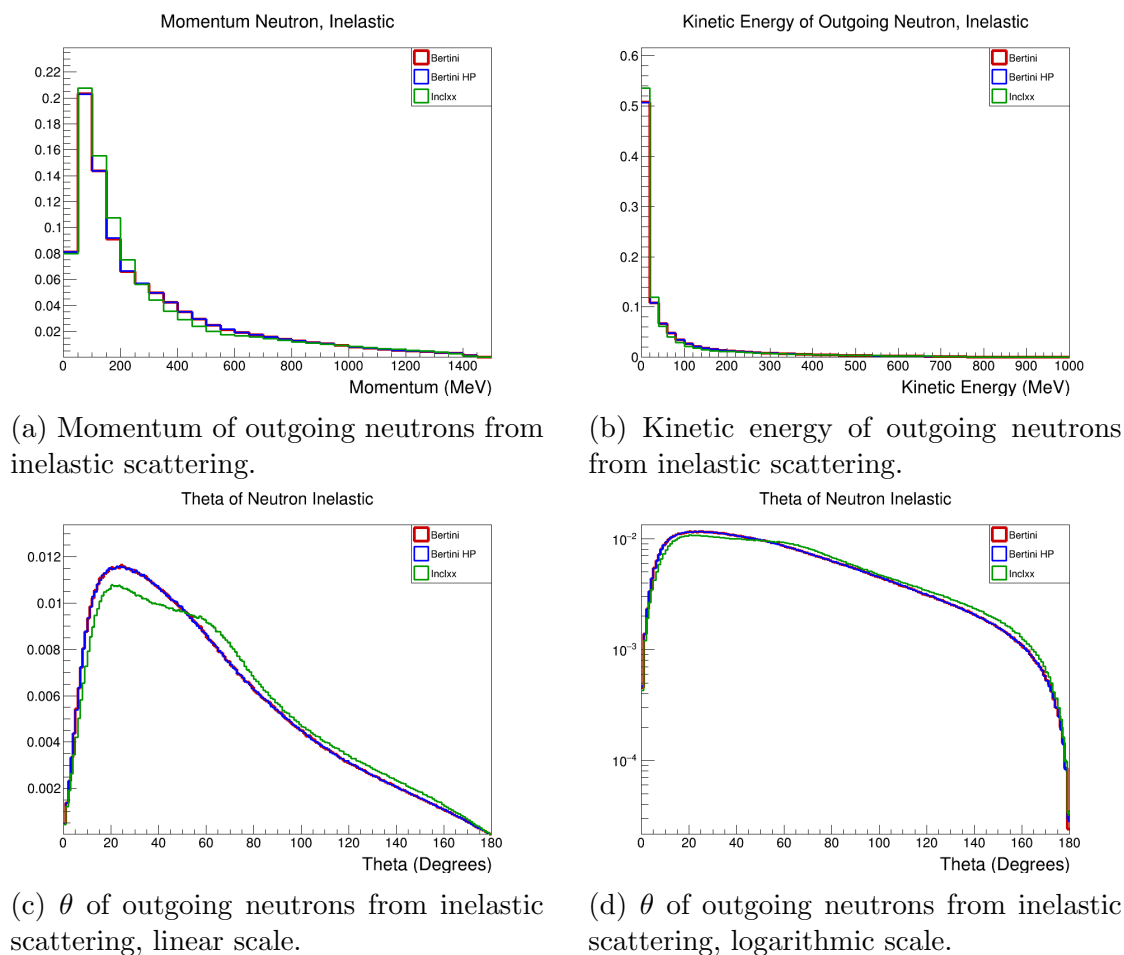


Figure 4.59. Comparison distributions for the kinematics of outgoing neutrons from inelastic collisions. Each line colour represents data produced by a different physics list. The histograms in these plots have been area normalized. The bottom right plot shows the data from the bottom left plot on a logarithmic y-axis scale. The top left plot shows the momentum distributions and the top right plot shows the kinetic energy distributions.

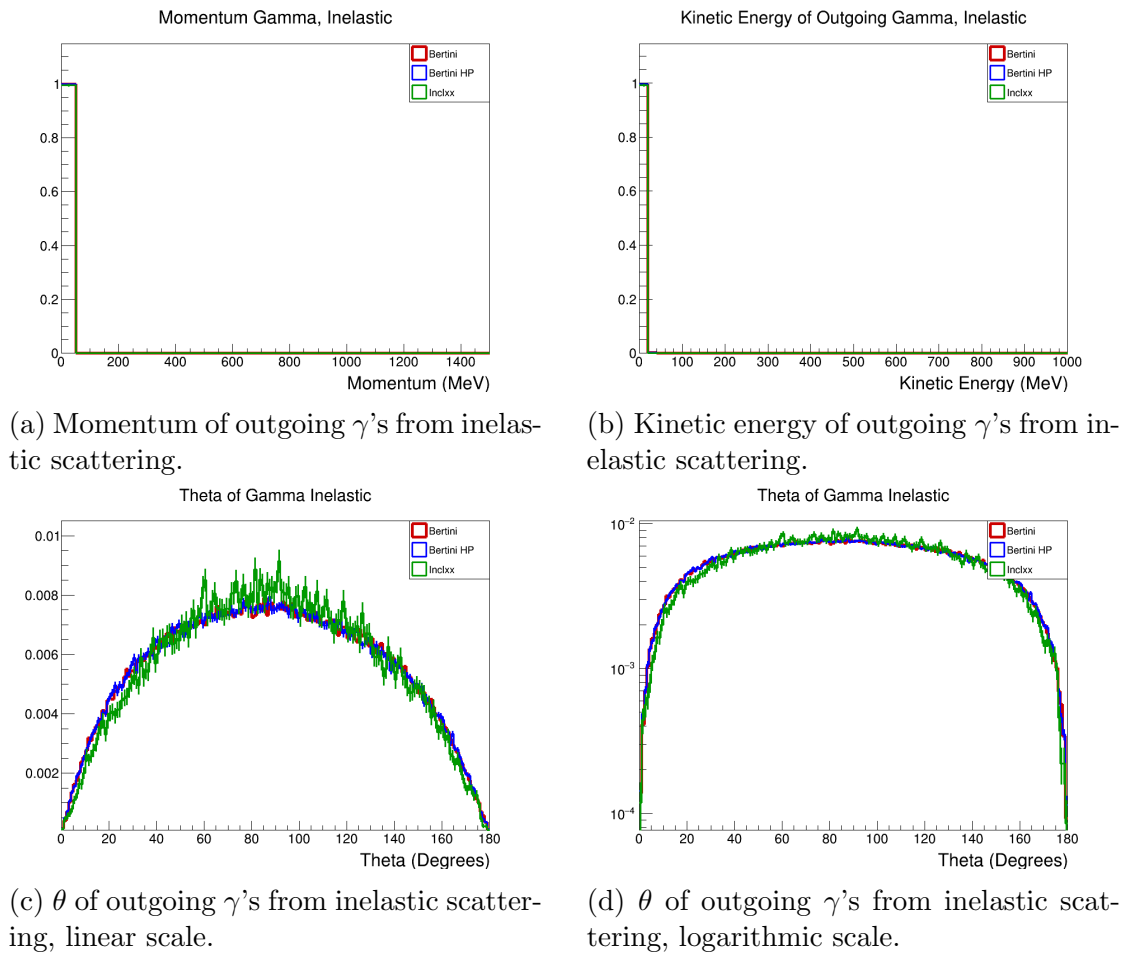


Figure 4.60. Comparison distributions for the kinematics of outgoing  $\gamma$ 's from inelastic collisions. Each line colour represents data produced by a different physics list. The histograms in these plots have been area normalized. The bottom right plot shows the data from the bottom left plot on a logarithmic y-axis scale. The top left plot shows the momentum distributions and the top right plot shows the kinetic energy distributions.

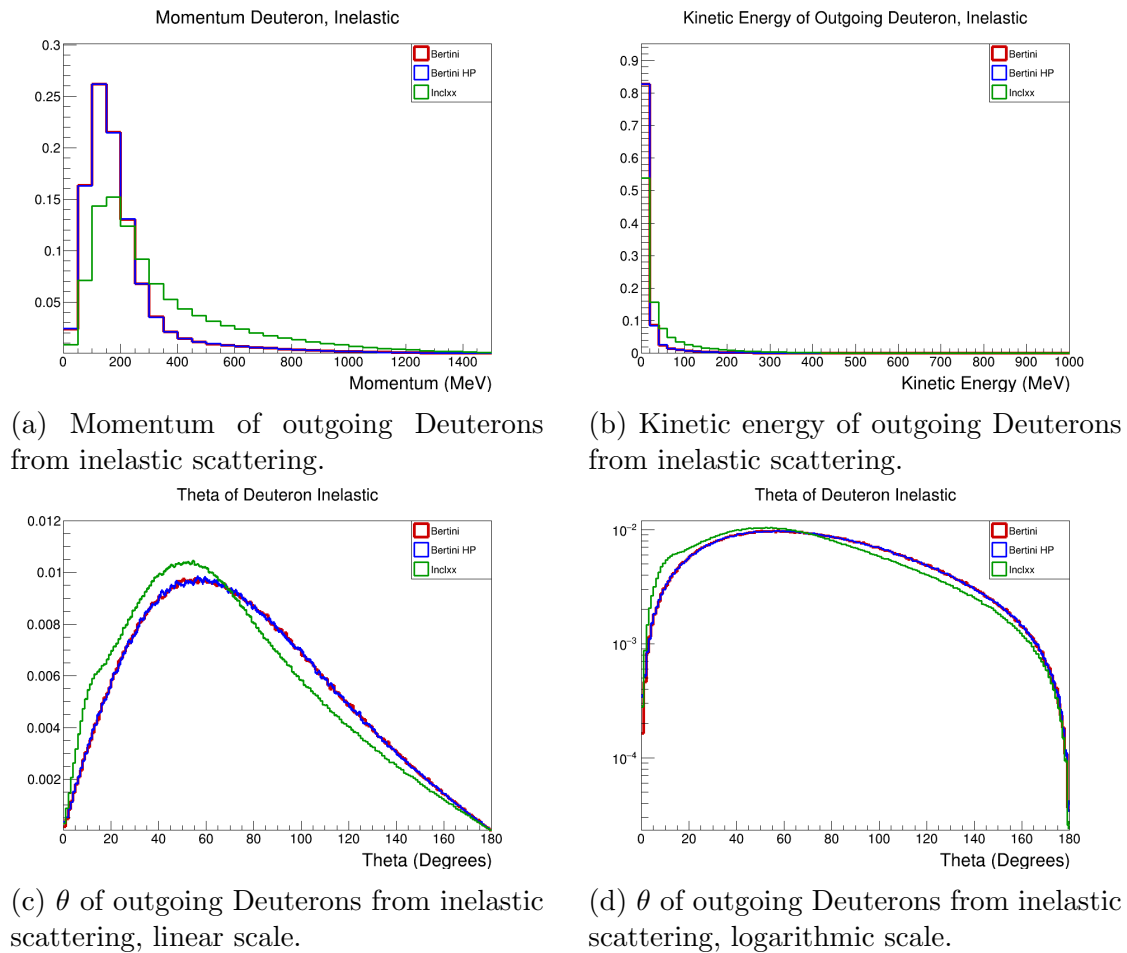


Figure 4.61. Comparison distributions for the kinematics of outgoing Deuterons from inelastic collisions. Each line colour represents data produced by a different physics list. The histograms in these plots have been area normalized. The bottom right plot shows the data from the bottom left plot on a logarithmic y-axis scale. The top left plot shows the momentum distributions and the top right plot shows the kinetic energy distributions.

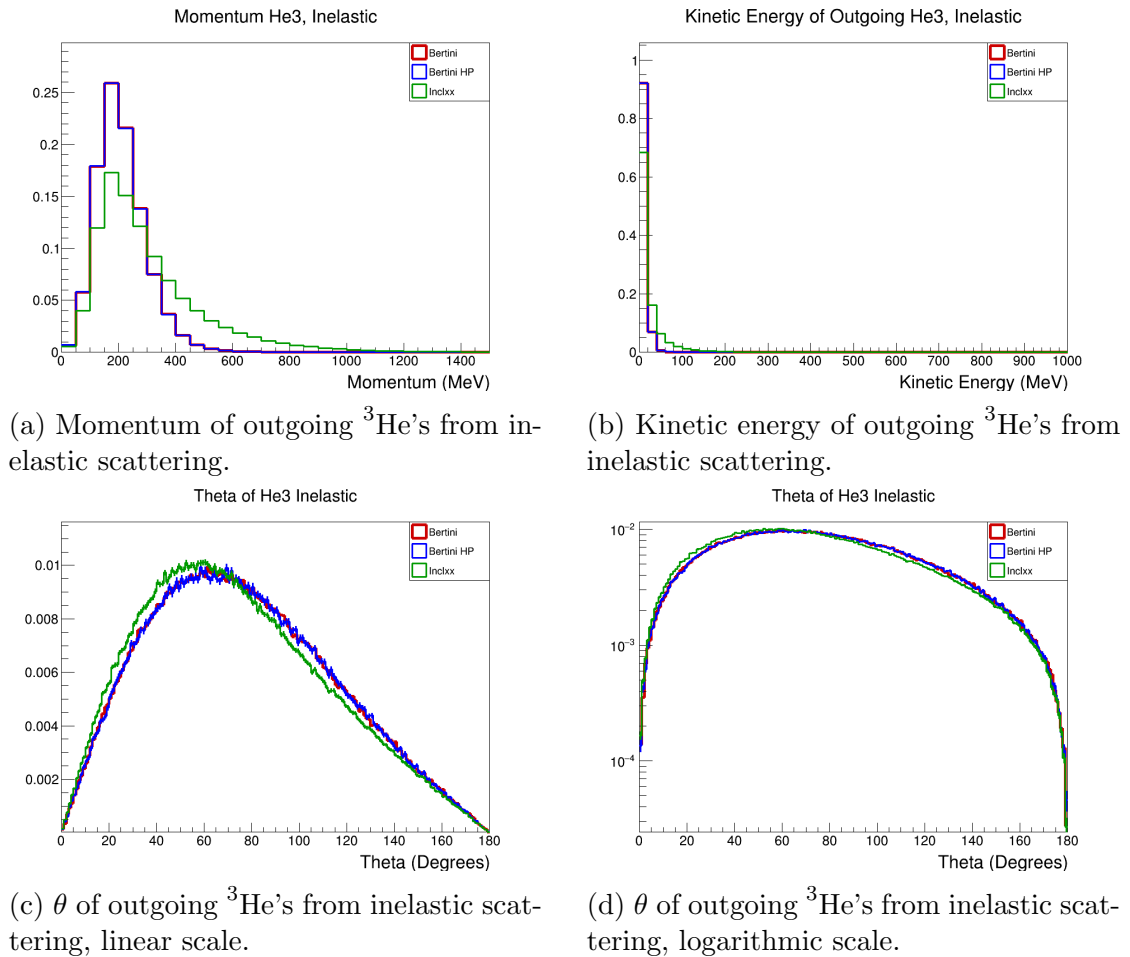


Figure 4.62. Comparison distributions for the kinematics of outgoing  ${}^3\text{He}$ 's from inelastic collisions. Each line colour represents data produced by a different physics list. The histograms in these plots have been area normalized. The bottom right plot shows the data from the bottom left plot on a logarithmic y-axis scale. The top left plot shows the momentum distributions and the top right plot shows the kinetic energy distributions.

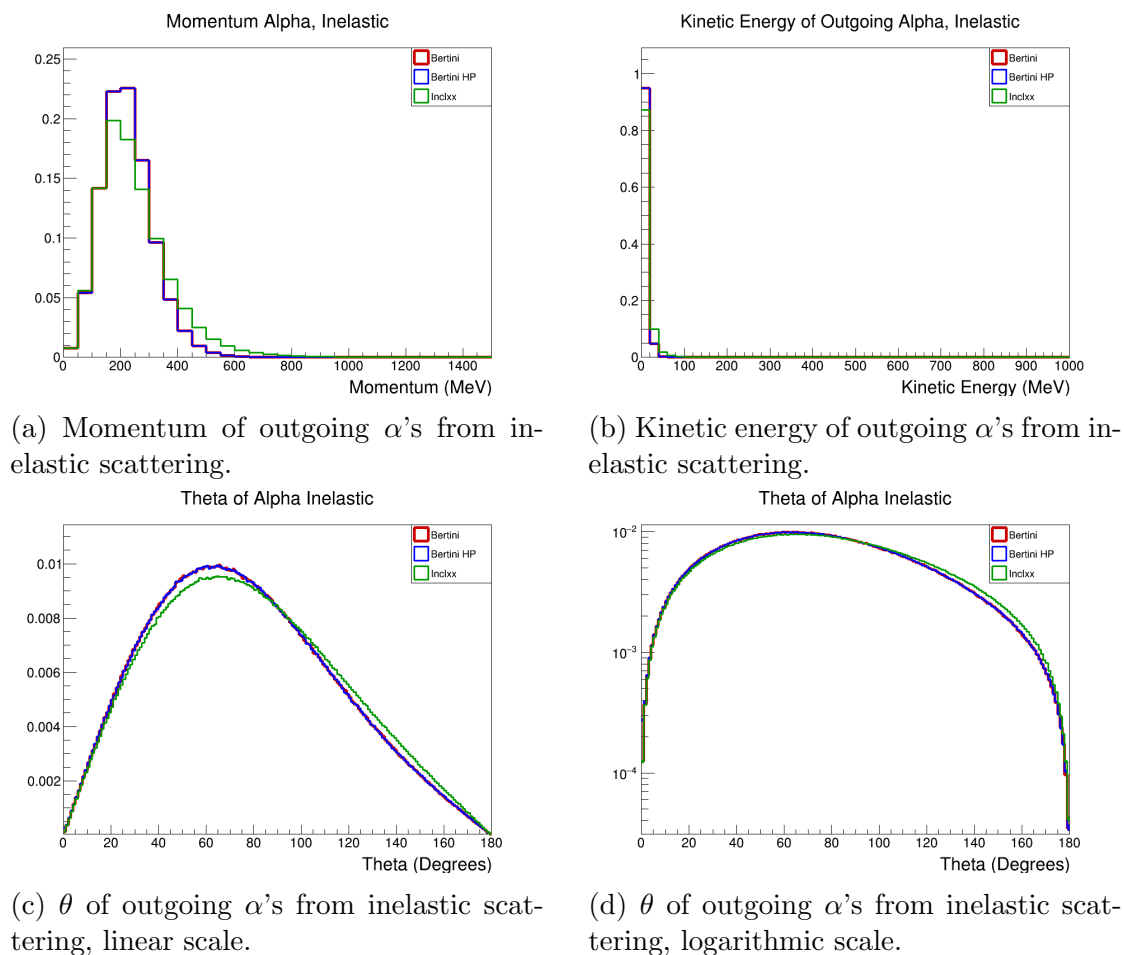
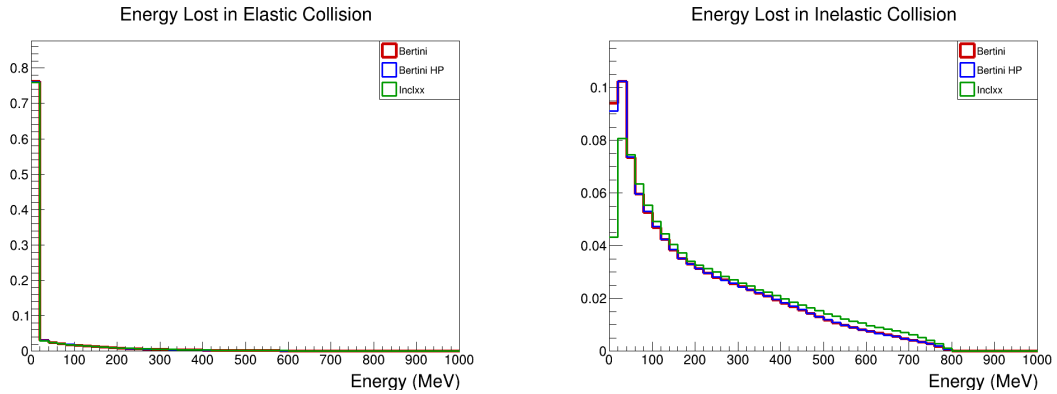


Figure 4.63. Comparison distributions for the kinematics of outgoing  $\alpha$ 's from inelastic collisions. Each line colour represents data produced by a different physics list. The histograms in these plots have been area normalized. The bottom right plot shows the data from the bottom left plot on a logarithmic y-axis scale. The top left plot shows the momentum distributions and the top right plot shows the kinetic energy distributions.



Energy loss distributions are shown in Fig. 4.64, wherein the “Energy Loss” refers to the difference between the energy of the incoming neutron before and after the interaction. As can be seen by Fig. 4.64a, the analyses over different physics lists mostly show nearly identical results for elastic collisions. However, in the 0-40 MeV range for Fig. 4.64b we observe that the analysis over the Iclxx physics list has a significantly lower number of entries than the BERTINI and BERTINI HP physics lists analyses, in addition to smaller discrepancies in shape at higher energies.

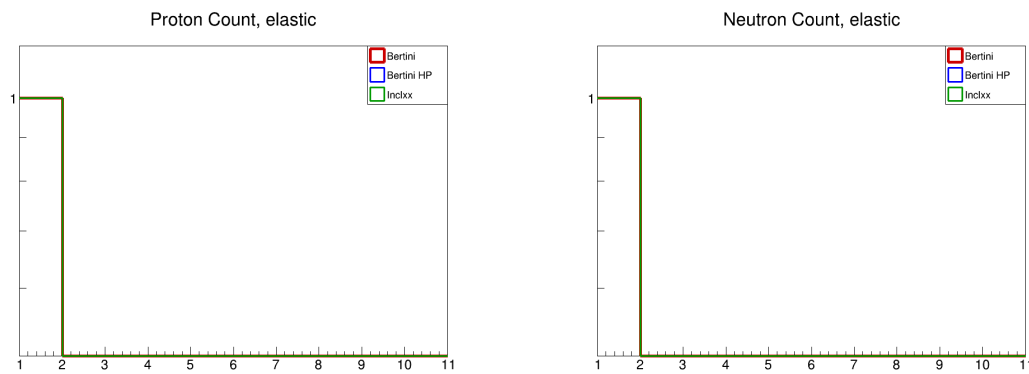


(a) Energy loss of incoming neutron (energy difference between incoming neutron and outgoing neutron) after elastic collision.

(b) Energy loss of incoming neutron (energy difference between incoming neutron and outgoing neutron) after inelastic collision.

Figure 4.64. Comparison distributions for the energy difference between the incoming neutrons and the outgoing neutrons for each event. Each line colour represents data produced by a different physics list. The histograms in these plots have been area normalized. The left plot shows the data for neutrons from elastic collisions and the right plot shows the data for neutrons from inelastic collisions.

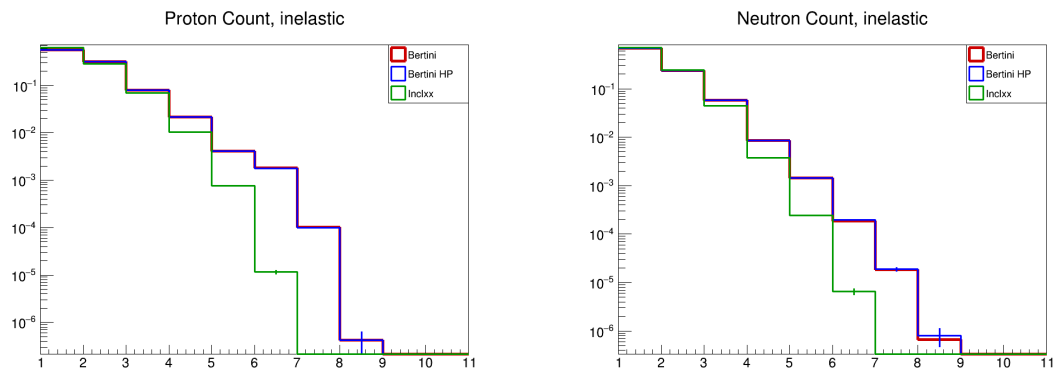
Area normalized distributions for the multiplicity of outgoing protons and neutrons from elastic scattering seen in Fig. 4.65 is identical, as expected. Although, Fig. 4.66 shows fewer number of outgoing neutrons and protons produced from inelastic scattering on the INCLXX analyses than on the BERTINI & BERTINI HP analysis. Although, the order of magnitude on which these differences take place is considerably smaller than the overall scale of the distributions (note the logarithmic scale) - as can be viewed by the observational differences between Fig. 4.66 and Fig. C.9. The number of  $\pi^\pm$ 's produced per event are nearly identical across all 3 analyses. The event where we have 7 and 8 outgoing protons and neutrons could potentially be due to interactions with simulated air particles (oxygen, nitrogen, etc.) or due neutron interactions on  $^{13}\text{C}$  isotopes, however these events and the differences in the number of outgoing protons and neutrons per event between the physics lists requires further investigation to fully understand.



(a) Multiplicity (number of particles per event) of outgoing protons from Elastic Scattering, logarithmic y-axis.

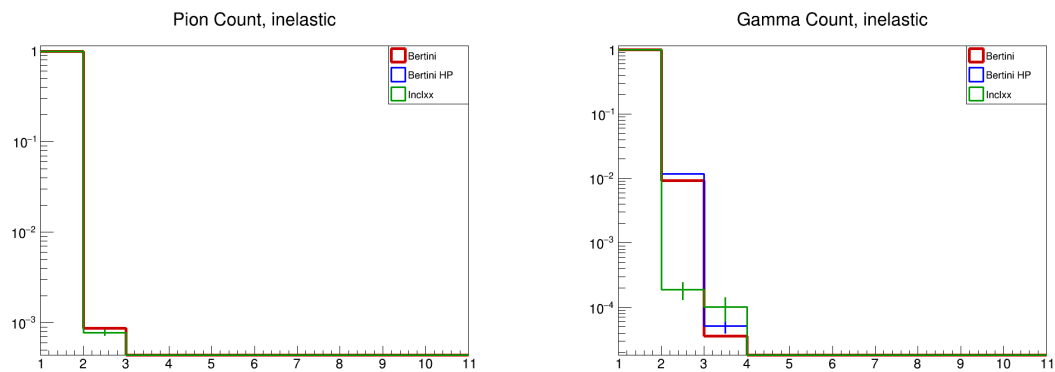
(b) Multiplicity (number of particles per event) of outgoing neutrons from elastic scattering, logarithmic y-axis.

Figure 4.65. Comparison distributions for the multiplicity (number of particles per event) of outgoing particles from elastic collisions. Each line colour represents data produced by a different physics list and both plots show the data on a logarithmic y-axis scale. The histograms in these plots have been area normalized. The right plot shows the data for outgoing neutrons, while the left plot shows data for the outgoing protons.



(a) Multiplicity (number of particles per event) of outgoing protons from inelastic scattering, logarithmic y-axis.

(b) Multiplicity (number of particles per event) of outgoing neutrons from inelastic scattering, logarithmic y-axis.



(c) Multiplicity (number of particles per event) of outgoing charged pions from inelastic scattering, logarithmic y-axis.

(d) Multiplicity (number of particles per event) of outgoing  $\gamma$ 's from inelastic scattering, logarithmic y-axis.

Figure 4.66. Comparison distributions for the multiplicity (number of particles per event) of outgoing particles from inelastic collisions. Each line colour represents data produced by a different physics list. The histograms in these plots have been area normalized. All plots show the same data as Fig. C.9 on a logarithmic y-axis scale. The top right plot shows the data for outgoing neutrons, while the top left plot shows data for the outgoing protons. The bottom left plot shows the data for outgoing charged pions and the bottom right plot shows the data for outgoing  $\gamma$ 's.

# Chapter 5

## Single-Track Event Selection

Recall that our detector is a voxelized scintillation detector; meaning when a charged particle scintillates inside the detector we will be able to determine from which cubes (or voxels, note that the terms ‘cube’ and ‘voxel’ may be used interchangeably here) the scintillation light occurred. However, we will not know where specifically from within a given voxel that charged particle interacted with the CH material. This limits the accuracy to identify the position points of charged particles in our detector to the dimensions of each  $1\text{cm}\times 1\text{cm}\times 1\text{cm}$  cube. Though this is a considerable improvement from the FGD used in the near detector of T2K, it is a limitation that needs to be accounted for. The MC simulations were converted into a format similar to data using a framework developed by multiple members of the collaboration and stored in the repository at Ref. [17]. We have restructured this code to aid our investigation into neutron interactions with a single outgoing charged particle.

Measurements of the cross section for neutron interactions on CH by firing a beam of neutrons and  $\gamma$ 's at the SuperFGD prototype considered depletion of the number of events along the axis of the beam (Ref [3]). In order to do this, a selection on neutron interactions with 1 outgoing charged particle was conducted as so called ‘single-track events’ allowed for a clear identification of the vertex of interaction. Since a long-term goal for this research is to compare the analyses on the MC simulations to analyses conducted on the 2019 and 2020 LANL beam test data, we are interested in better understanding these single-track events. Specifically, we want to investigate the purity of the particle types and collision types contributing maximally to these single-track events.

### 5.1 LANL Software

#### 5.1.1 Monte Carlo Reduction

We use a script known as `dumptree.py` to convert MC simulations of neutrons interacting on a CH target into a tree of values. Using the MC simulation files as input, `dumptree.py` scans through the files, determines attributes of each particle for every point of every trajectory in every event, and saves these values to an output file containing a tree of these values. In addition to particle kinematics, we have modified added functionality into `dumptree.py` to store additional information including particle type, process type and subprocess type at every point from

the MC input files.

The output file of this script is a tree of branches with values, and has no “structure” per se; it does not give us any information about which points belong to which trajectories. In order to move forward, we need to organize the output of `dumptree.py` into a usable format to allow us to analyze outgoing particle kinematics. For this, we have another script written by multiple members of the collaboration: `EventStructureMCUpdate.exe` (Henceforth referred to as Event Structure) [17].

### 5.1.2 Monte Carlo Restructure

The Event Structure script takes in the tree of values from the output of `DumpTree.py` and performs selection cuts each entry to organize them to represent neutron interactions. The script additionally sets these organized values in a tree of Event objects, where “Event” is a specified class of objects containing information about particle trajectories, kinematics and position among other information. In this sense, the output of Event Structure resembles the organization of information we would expect to obtain from data. We adapted the Event Structure script to account for modifications we made to `dumptree.py`, including saving particle type and interaction type information. The output of the Event Structure script is a file containing a Tree of Event objects, where the kinematics for all points of all trajectories were assigned and set to each Event and organized to show neutron interaction in CH. The output of this script is in a usable file format for analyses including selection of single-track events, covered in the following section.

## 5.2 Single-Track Event Selection

Depending on how charged particles interact with the hydrocarbon target throughout the detector volume, we may observe a variety of different signal structures from the voxels in which scintillation has occurred, such as those depicted in Fig. 5.1. Recall that only charged particles will produce scintillation light, so we will only observe signals from charged particles moving through the detector volume. If we have the case of a charged particle interacting with the detector volume resulting in the production of a non-charged particle, and later that non-charged particle interacts with the detector volume to produce a charged particle which moves through the detector, we will only see the charged particles - as depicted in Fig. 5.1d.

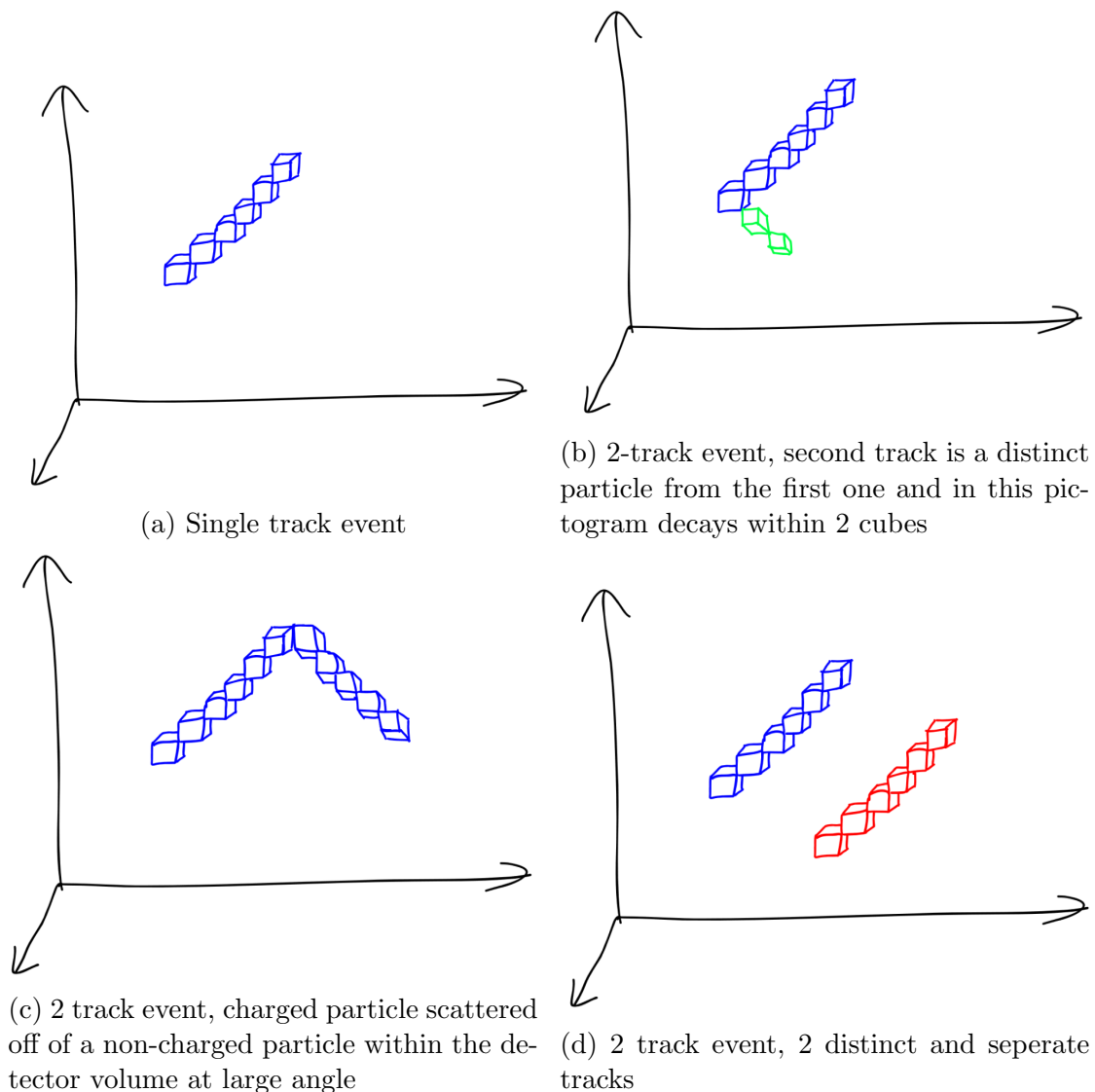


Figure 5.1. Pictogram illustrating possible observed tracks in the detector volume. Each cube represents a voxel from which scintillation light has been detected. Each colour represents a different particle type. The axis shows both a general idea of axial coordinates and represents the corner of the detector volume.

Note that there are limitations to the detector's ability to accurately observe single-

track events, as we may have any of the following three cases in Fig. 5.2. We could have 2 tracks generated within the same cube, and one of them stops inside the first cube as in Fig. 5.2b. Alternatively, we may have multiple charged particles moving close together relative to the cube size, resulting in observing a signal which looks like a single-track event but is not - as depicted by Fig. 5.2c. The limitations of measuring single-track events should be taken into consideration when analyzing data, however is not of major concern when analyzing MC simulation files that have been re-formatted to resemble data. We are able to obtain direct position information of each track from the MC simulations, and are able to obtain voxelized position information of each track from reconstructed data. In doing so, we are able to compare the truth of the positions of single-track events within the detector volume (directly from MC simulation files) to the reconstructed data of single-track events. In this analyses, we found the maximum distance between a true and reconstructed single-track event is 8.3 mm; less than half the diagonal distance across a single cube ( $\frac{\sqrt{3}}{2}$  cm  $\approx$  8.6 mm).

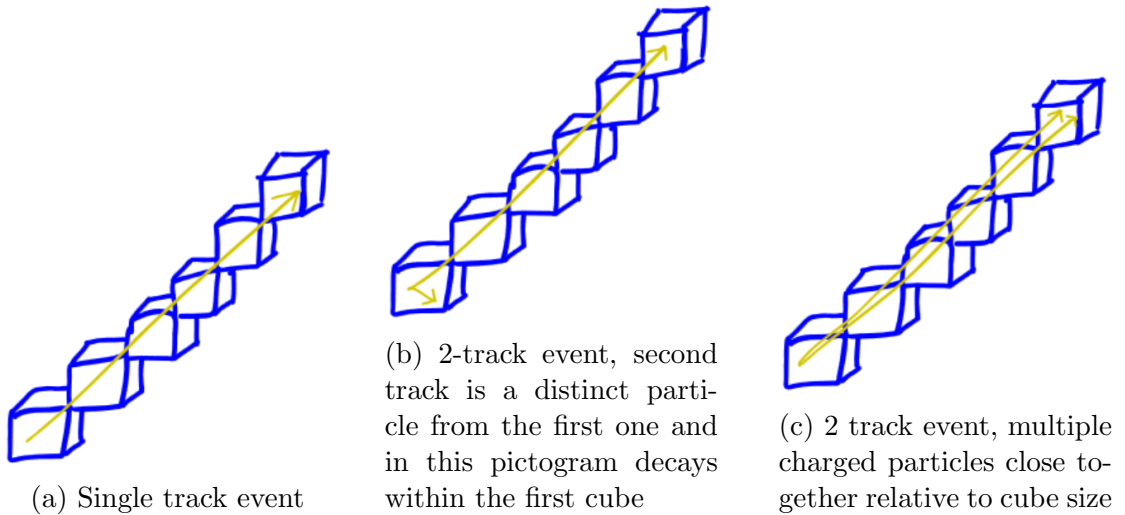


Figure 5.2. Pictogram illustrating possible ways we may observe a “single” track event in the detector volume. Each cube represents a voxel from which scintillation light has been detected. The straight, yellow lines represent the path of the charged particle through the detector material.

Several cuts are made on each event to determine whether or not an event we are considering is a “single-track” event, including:

- Ensuring that each hit meets a minimum energy deposit threshold (or 80% of a minimum potential energy threshold for an attenuated beam).
- Requiring that we have more than 3 voxels to ensure that we are not considering noise or particles from outside sources (3 cm is our spatial resolution for the SuperFGD and SuperFGD prototype).
- Using a clustering algorithm to “group” each track into “clusters” to ensure that we only consider events with 1 cluster, effectively removing events such as Fig. 5.1d from consideration.

- Calculating a principal component vector for each cluster, and requiring that the maximum width of the cluster surrounding the computed principal component vector associated with the track is within a certain boundary. Events such as the ones depicted by Fig. 5.1b and Fig. 5.1c would be grouped as single clusters, however the principal component vectors associated with these clusters would fall out of bounds of the cut and therefore such events would not be considered single-track events.
- Performing a check to ensure that the selected track is within the fiducial volume of the detector.

After these cuts are performed, only a small number of tracks survive. Running this analysis over 64 million events for incoming neutron energies from 0-800 MeV (8000 events per MeV), we note that we have 588695 events which survive these cuts and are marked as “single-track events;” about 0.91% of all events. From these, using the data saved from the MC simulation we are able to categorize the maximally contributing particles from these events by particle type, interaction type, and interaction process.

### 5.3 Purity Analysis

From the truth information, we are able to determine the particle type, interaction type and interaction processes of all particles in single-track events. In fact, with truth data we are able to determine which single-track events are missed track events, such as depicted in Fig. 5.2b and Fig. 5.2c. Given this insight, we are able to determine the energy deposition of each particle in each single-track event, considering the particles with highest energy deposition as those which have contributed maximally to the hit. We have organized these maximally contributing particles to single-track events by particle type, interaction type, and process type in Table I, Table II, and Table III.

It is imperative to understand that Geant4 may attribute energy deposition to neutral particles. Physically this makes no sense, however this can occur if a neutral and charged particle are created from an interaction vertex and the charged particle decays without travelling enough distance for Geant4 to track it. In such a case, Geant4 attributes an “energy deposition” to the neutral particle equal to the energy of the charged particle at the stopping point of the charged particle. Therefore particles determined to be incident neutrons (identified by other parameters including `TrackID` and `ParentID`) were ignored from consideration as particles with “highest energy deposition.” For inelastic collisions, outgoing neutrons with largest energy deposition were determined to be the incident neutron.

We find that the 84.7% of particles from single-track events which have the largest energy deposit are protons, and that 97.2% of single-track events are from hadronic neutron interactions. We expect the majority of single-track events to be attributed to elastic scattering on hydrogen, hence we expect outgoing protons to have the highest energy deposition for most events.  $\pi^\pm$ 's,  $\alpha$ 's,  $e^-$ 's, isotopes of carbon and deuterons cumulatively make up 13.3% of maximally contributing particles to single-track events, with each particle type contributing maximally to less



than 6.0% of single-track events. The presence of neutral particles ( $^{12}\text{C}$  and neutrons) is a feature of how Geant4 attributes energy deposition, and these neutral particles cumulatively comprise of <2.2% of maximally contributing particles from single-track events. The presence of nitrogen is likely due to air particles in the simulation, though they are insignificant in number.

It is interesting to see that 56.0% of single-track events are from inelastic interactions, while 41.2% of single-track events are from elastic interactions. Further investigations into the purities of outgoing particles from elastic and inelastic events separately is of high interest for future work.

TABLE I. Purity of maximally contributing outgoing particles for single-track events from neutron interactions with hydrocarbon

| Particle Type                | Purity  |
|------------------------------|---------|
| p                            | 84.7%   |
| $\pi^\pm$                    | 5.9%    |
| $\alpha$                     | 2.7%    |
| $e^-$                        | 2.5%    |
| $^8\text{C} - ^{13}\text{C}$ | 1.3%    |
| $^2\text{H}$                 | 1.0%    |
| $e^+$                        | 0.3%    |
| $^3\text{He}$                | 0.3%    |
| $\mu^+$                      | 0.01%   |
| $\mu^-$                      | < 0.01% |
| $\gamma$                     | < 0.01% |
| n                            | < 0.01% |
| Others                       | 1.19%   |

TABLE II. Purity analysis of “Other” maximally contributing outgoing particles (from Table I) for single-track events from neutron interactions with hydrocarbon

| Particle Type                   | Purity  |
|---------------------------------|---------|
| $^8\text{B} - ^{12}\text{B}$    | 0.6%    |
| $^3\text{H}$                    | 0.4%    |
| $^6\text{Be} - ^{11}\text{Be}$  | 0.2%    |
| $^{10}\text{N} - ^{15}\text{N}$ | < 0.01% |

TABLE III. Interaction processes and sub-processes of maximally contributing outgoing particles for single-track events from neutron interactions with hydrocarbon

| First Interaction Process<br>(ProcessID) | First Interaction Type<br>(SubProcessID) | Purity  |
|--|--|---------|
| Hadronic                                 | Inelastic Scattering                     | 56.0%   |
|  | Elastic Scattering                       | 41.2%   |
|  | Hadron at Rest                           | < 0.01% |
| Electromagnetic                          | Compton Scattering                       | 2.3%    |
|  | Gamma Conversion                         | 0.3%    |
|  | Ionization                               | < 0.01% |
| Decay                                    | Decay                                    | 0.2%    |

# Chapter 6

## Future Work & Conclusions

### 6.1 Improvements to Methodology

Comparing analyses over different physics lists and over different versions of Geant is a promising area to further understand the limitations of the toolkit towards physics modelling for our purposes. A thorough investigation into multiple versions of the Geant source code is a promising next step to better understand expected differences in the analyses given differences between the Geant versions. Furthermore, such an investigation may allow for a better understanding of how to identify the incident neutron from outgoing particles resulting from an inelastic neutron scattering off of carbon. In fact, investigation into the analyses using different Geant versions may show  $\pi^0$  production, especially when considering that carbons were not accounted for at all when using the older version of Geant despite neutron elastic scattering on carbon was observed.

Additionally, separate analyses on the kinematics of incoming neutrons interacting inelastically with carbon organized by outgoing particle types produced is of key interest to better understand inelastic interactions of neutrons on CH. The ENDF provides data for the total neutron cross sections for production of  $\gamma$ 's,  $\pi^\pm$ 's,  $\pi^0$ 's, protons, neutrons, deuterons,  $^3\text{He}$ 's, and  $\alpha$ 's from neutron inelastic scattering on carbons. These plots for 0-800 MeV incident neutron energies are provided in the appendix (Fig. C.18 - Fig. C.25), and re-producing these distributions from MC would be a good verification of the inelastic neutron scattering distributions.

Finally, we are interested to investigate a purity analysis of single-track events produced from inelastic neutron interactions on CH, and the interaction channels contributing to these events.

### 6.2 Comparisons to Data

The most prominent area of investigation now is to compare analyses on 2019 and 2020 LANL beam data to the analyses conducted on MC files for this thesis. We should begin by refining the file conversion process to re-format data to a file format which will allow us to run the analysis code. Collaborators within the group are currently working on verifying the results from analyses on the converted files, hence there is currently active progress being made. Additionally, comparisons between truth events (from MC simulations), reconstructed events,

and data events would be interesting to further investigate expected features of outgoing particle kinematics from neutron interactions on a CH target.

## 6.3 Code Robustness

Currently, the code used for the above analyses is very hard-coded, and has limited flexibility. Additionally, the main `.cc` file used to create the executable contains over 2500 lines of code alone, and the computation time for analyses of MC simulation files over the full incoming neutron energy range currently takes about 2 hours. There are many inefficiencies within the script which (though they do not affect the analysis) increase computation time and therefore increase the time spent on a computing cluster when an analysis job is submitted - taking away computing resources from others who may need the space. Increasing the robustness of the script by introducing more effective computational methods and improvements to code formatting without affecting the analysis would decrease computation time required to produce these analysis results, allowing us to conduct more analyses over a larger array of parameters (such as analyses for MC files generated using different Geant versions and different physics lists). Moreover, this would free up resources available to others on a local computing cluster.

Additional quality of life improvements such as command line argument implementation are also of key interest. The easier the script is to use by changing parameters in the command line, the more accessible analysis of this nature becomes. Without these improvements, one would need to read at length through the script contents and comments or other technical documents to gain an understanding of how to use the script. While such technical notes are important for documenting how such computation proceeds, they should not be required to understand how to use the analysis program. Finally, implementing CPU and GPU usage (such as using CUDA) to parallelize the computations is of interest in the long-term to improve computation time.

## 6.4 Final Remarks

Our analyses of neutron interactions on a CH target largely illustrates features expected from cross section distributions and classical kinematics. We observe that elastic interactions of neutrons on hydrogen contribute largely to elastic collisions of neutrons on CH, whereas inelastic interactions on a CH target are dominated by inelastic interactions on carbon. Outgoing neutrons and protons from elastic collisions share a dip structure with two peaks at high and low  $\theta$  due to the expected cross sections as a function of angle and the  $90^\circ$  angle between outgoing particles with similar masses calculated in Section 3.1.1. We also observe negligible amounts of neutrons and protons with  $\theta > 90^\circ$  as a feature of the MC simulations, as we do not expect either mass in elastic scattering of particles with similar masses with a  $\theta > 90^\circ$ . For elastic scattering of neutron off carbon, we observe most carbons with  $\theta \sim 90^\circ$  while the majority of neutrons have low  $\theta$ , although we do see neutrons with  $\theta > 90^\circ$  given the  $\approx 12\times$  mass difference between the carbon and neutron.

The kinetic energy distributions for all outgoing particles from elastic collisions of neutrons on hydrogen and carbon largely agree with the cross sections as functions of incident neutron energy in Chapter 3. However, there is a considerable difference between the expected and observed number of outgoing particles from inelastic collisions on hydrogen by particle type. We expect a 1:1:1:1 ratio of outgoing protons, neutrons, charged pions and neutral pions from the cross sections - but we do not observe any neutral pions. Moreover, we observe a significantly larger number of outgoing protons from inelastic collisions than outgoing neutrons; which does not agree with the interaction channels proposed. Furthermore, we observe a  $\approx 75$  MeV difference between when we would expect to see inelastic interactions begin to occur and when we actually observe them. Although inelastic scattering of neutrons on hydrogen contribute an order of magnitude less to inelastic interactions on CH than inelastic interactions on carbon do, these features require further investigation.

Comparisons between the analyses conducted on MC files constructed using different physics lists overall showed no significant difference between the Bertini and Bertini HP models aside from momentum at the 0-20 MeV range, as was expected. However, notable differences between the Bertini and Inclxx distributions were apparent in most kinematics investigated for outgoing particles from inelastic collisions; notably the kinetic energy and momentum distributions for outgoing protons and neutrons from inelastic collisions differed significantly between the analyses conducted on both physics lists. No significant differences between the analyses conducted on different physics lists were found for outgoing particles from elastic collisions. These are to be expected as the INCLXX uses an intra-nuclear cascade model (the Leige Intranuclear Cascade model) which is more appropriate for modelling inelastic scattering of neutrons on carbon than the Boltzmann gas model used by the BERTINI and BERTINI HP physics lists.

Momentum distributions for elastic scattering are verified by our understanding of the respective kinetic energy and  $\theta$  distributions, and  $\theta$  distributions for inelastic scattering are verified by our understanding of the respective momentum and kinetic energy distributions.

We performed a single-track event selection on both MC simulations and reformatted simulations to resemble data. In doing so, we were able to measure the maximum distance between the principal component vectors of clusters and the true position vectors of each single-track particle through the detector to determine that the largest distance found was less than half the diagonal distance of a single cube. This demonstrates high agreement between truth and reconstructed tracks. Using information passed from the MC simulations, we performed a purity analysis on the particles with maximum energy deposition in each single-track event.  $\sim 84.7\%$  of single-track events have protons contributing maximally to the hit, with charged pions,  $\alpha$ 's and  $e^-$ 's contributing maximally to  $\sim 5.9\%$ ,  $\sim 2.7\%$ ,  $\sim 2.5\%$  of single-track events. Other particle types make up  $\sim 1\%$  or fewer than  $\sim 0.01\%$  of maximum contributing particles to single-track events. Neutral particles contributing to energy deposition is a feature of the software version we are using. Hadronic interactions contribute to  $\sim 97.2\%$  of single-track events, with electromagnetic interactions and decays contributing to  $\sim 2.6\%$  and  $\sim 0.2\%$ , respectively.

# Appendices

# Appendix A

## Additional Tables

TABLE I. Table of Geant4 ProcessID's.

| ProcessID Value | Type of Process    |
|-----------------|--------------------|
| 0               | Not Defined        |
| 1               | Transportation     |
| 2               | Electromagnetic    |
| 3               | Optical            |
| 4               | Hadronic           |
| 5               | Photolepton hadron |
| 6               | Decay              |
| 7               | General            |
| 9               | Parameterisation   |
| 10              | UserDefined        |
| 11              | Parallel           |



TABLE II. Table of Geant4 SubProcessID's.

| SubprocessID Value | Type of Process                 |
|--------------------|---------------------------------|
| 1                  | Coulomb Scattering              |
| 2                  | Ionization                      |
| 3                  | Bremsstrahlung                  |
| 4                  | PairProdByCharged               |
| 5                  | Annihilation                    |
| 6                  | Annihilation to $\mu\mu$        |
| 7                  | Annihilation to Hadrons         |
| 8                  | Nuclear Stopping                |
| 10                 | Multiple Scattering             |
| 11                 | Rayleigh                        |
| 12                 | PhotoElectric Effect            |
| 13                 | Compton Scattering              |
| 14                 | $\gamma$ Conversion             |
| 15                 | $\gamma$ Conversion to $\mu\mu$ |
| 21                 | Cerenkov                        |
| 22                 | Scintillation                   |
| 23                 | Synchotron Radiation            |
| 24                 | Transition Radiation            |
| 91                 | Transportation                  |
| 92                 | Coupled Transportation          |
| 111                | Elastic                         |
| 121                | Inelastic                       |
| 131                | Capture                         |
| 141                | Fission                         |
| 151                | Hadron At Rest                  |
| 152                | Lepton At Rest                  |
| 161                | Charge Exchange                 |
| 201                | Decay                           |
| 210                | Radioactive Decay               |
| 211                | Unknown Decay                   |
| 231                | External Decay                  |
| 401                | Step Limiter                    |
| 402                | User Special Cuts               |
| 403                | Neutron Killer                  |

# Appendix B

## Proofs

### B.1 Classical calculation for angle between two masses of similar masses

Consider two masses  $m_1$  and  $m_2$ , where  $m_2$  is initially at rest and  $m_1$  impinges onto  $m_2$  with an initial velocity of  $\vec{v}_{1i}$ . After the collision, the masses move with velocities  $\vec{v}_{1f}$  and  $\vec{v}_{2f}$ , respectively. Recall conservation of momentum from Appendix B.1.

$$m_1 v_{1i} = m_1 v_{1f} + m_2 v_{2f} \quad (\text{B.1})$$

which by re-arranging we obtain:

$$v_{1i} = v_{1f} + \frac{m_2}{m_1} v_{2f} \quad (\text{B.2})$$

Applying the conservation of energy given by Appendix B.1,

$$\frac{1}{2} m_1 |\vec{v}_{1i}|^2 = \frac{1}{2} m_1 |\vec{v}_{1f}|^2 + \frac{1}{2} m_2 |\vec{v}_{2f}|^2 \quad (\text{B.3})$$

we may obtain:

$$|\vec{v}_{1i}|^2 = |\vec{v}_{1f}|^2 + \frac{m_2}{m_1} |\vec{v}_{2f}|^2 \quad (\text{B.4})$$

and applying the law of cosines Appendix B.1:

$$|\vec{v}_{1i}|^2 = |\vec{v}_{1f}|^2 + \left| \frac{m_2}{m_1} \vec{v}_{2f} \right|^2 - 2 |\vec{v}_{1f}| \left| \frac{m_2}{m_1} \vec{v}_{2f} \right| \cos(\phi') \quad (\text{B.5})$$

where  $\phi$  is the angle between the masses and  $\phi'$  is  $\pi - \phi$  since we used the law of cosines, we obtain:

$$0 = \left| \frac{m_2}{m_1} \vec{v}_{2f} \right|^2 - 2 |\vec{v}_{1f}| \left| \frac{m_2}{m_1} \vec{v}_{2f} \right| \cos(\phi') - \frac{m_2}{m_1} |\vec{v}_{2f}|^2 \quad (\text{B.6})$$

$$\frac{m_2^2}{m_1^2} |\vec{v}_{2f}|^2 - \frac{m_2}{m_1} |\vec{v}_{2f}|^2 = 2 \frac{m_2}{m_1} |\vec{v}_{1f}| |\vec{v}_{2f}| \cos(\phi') \quad (\text{B.7})$$

$$\frac{m_2}{m_1} |\vec{v}_{2f}| - |\vec{v}_{2f}| = 2 |\vec{v}_{1f}| \cos(\phi') \quad (\text{B.8})$$

$$\frac{\left(\frac{m_2}{m_1} - 1\right) |\vec{v}_{2f}|}{2 |\vec{v}_{1f}|} = \cos(\phi') \quad (\text{B.9})$$

$$\arccos\left(\frac{\left(\frac{m_2}{m_1} - 1\right) |\vec{v}_{2f}|}{2 |\vec{v}_{1f}|}\right) = \phi' \quad (\text{B.10})$$

And if we set  $m_1 = m_2$  in Appendix B.1, we get:

$$\arccos\left(\frac{0 \times |\vec{v}_{2f}|}{2 |\vec{v}_{1f}|}\right) = \phi' \quad (\text{B.11})$$

$$\arccos(0) = \phi' \quad (\text{B.12})$$

$$90^\circ = \phi' \quad (\text{B.13})$$

$$90^\circ = \phi \quad (\text{B.14})$$

Therefore, for particles with similar masses involved in elastic scattering, the angle between them will always be  $90^\circ$ .

## B.2 Maximum angle between carbon and neutron from elastic neutron scattering

Recalling Eq. (3.1) and noting that for neutron impinging on a  $C^{12}$  at rest,  $m_2 \approx 11262 \text{ MeV}$ ,  $m_1 \approx 939 \text{ MeV}$ , so we have:

$$\phi' = \arccos\left(\frac{|\vec{v}_2| \left(\frac{m_{C^{12}}}{m_n} - 1\right)}{2 |\vec{v}_1|}\right) \quad (\text{B.15})$$

Recalling conservation of energy in Appendix B.1, and recalling  $Q_{Max}$  discussed in Section 3.2.1, assuming maximum energy transfer from the neutron to the carbon, we can obtain:

$$0.28 E_n \approx E_{C^{12}} \quad (\text{B.16})$$

$$0.28 m_n v_{1i}^2 \approx m_{C^{12}} v_{2f}^2 \quad (\text{B.17})$$

$$\sqrt{\frac{0.28 m_n}{m_{C^{12}}}} |\vec{v}_{1i}| \approx |\vec{v}_{2f}| \quad (\text{B.18})$$

and since

$$|\vec{v}_{1f}| < |\vec{v}_{1i}| \quad (\text{B.19})$$

we get:

$$\sqrt{\frac{0.28m_n}{m_{C^{12}}}} |\vec{v}_{1f}| < \sqrt{\frac{0.28m_n}{m_{C^{12}}}} |\vec{v}_{1i}| \approx |\vec{v}_{2f}| \quad (\text{B.20})$$

leading us to:

$$\frac{|\vec{v}_{2f}| \left( \frac{m_{C^{12}}}{m_n} - 1 \right)}{2|\vec{v}_{1f}|} > \frac{\sqrt{\frac{0.28m_n}{m_{C^{12}}}} |\vec{v}_{1f}| \left( \frac{m_{C^{12}}}{m_n} - 1 \right)}{2|\vec{v}_{1f}|} = \frac{\sqrt{\frac{0.28m_n}{m_{C^{12}}}} \left( \frac{m_{C^{12}}}{m_n} - 1 \right)}{2} \quad (\text{B.21})$$

and therefore:

$$\frac{|\vec{v}_{2f}| \left( \frac{m_{C^{12}}}{m_n} - 1 \right)}{2|\vec{v}_{1f}|} > \frac{\sqrt{\frac{0.28 \times 939}{11262}} \left( \frac{11262}{939} - 1 \right)}{2} \approx 0.839 \quad (\text{B.22})$$

Hence, the domain of  $\phi'$  is restricted to being less than  $\approx 0.839$ . That is to say, though the domain of arccos is mathematically  $[-1, 1]$ , the domain of  $\phi'$  due to the limitation of the max energy transfer possible from neutrons to carbon-12's is  $[-1, 0.839]$ . Moreover, since the arccos value we are taking will always be  $\geq 0$  for the carbon the domain of  $\phi'$  is actually  $[0, 0.839]$ . Therefore, the range of  $\phi'$  is  $[\approx 32^\circ, 90^\circ]$  - therefore since  $\phi = \pi - \phi'$  the range of  $\phi$  changes to  $[90^\circ, \approx 148^\circ]$ . Meaning that for maximum energy transfer, we have a minimum angle between the outgoing particles of  $\phi \approx 90^\circ$  and a maximum angle of  $\phi = 148^\circ$ . Note that this is for maximum energy transfer, and if we transfer less energy then we may have  $\phi < 90^\circ$ , and in fact for higher energy neutrons we have lower energy transfer to carbons via elastic scattering, as discussed in Section 4.4.

# Appendix C

## Additional Plots

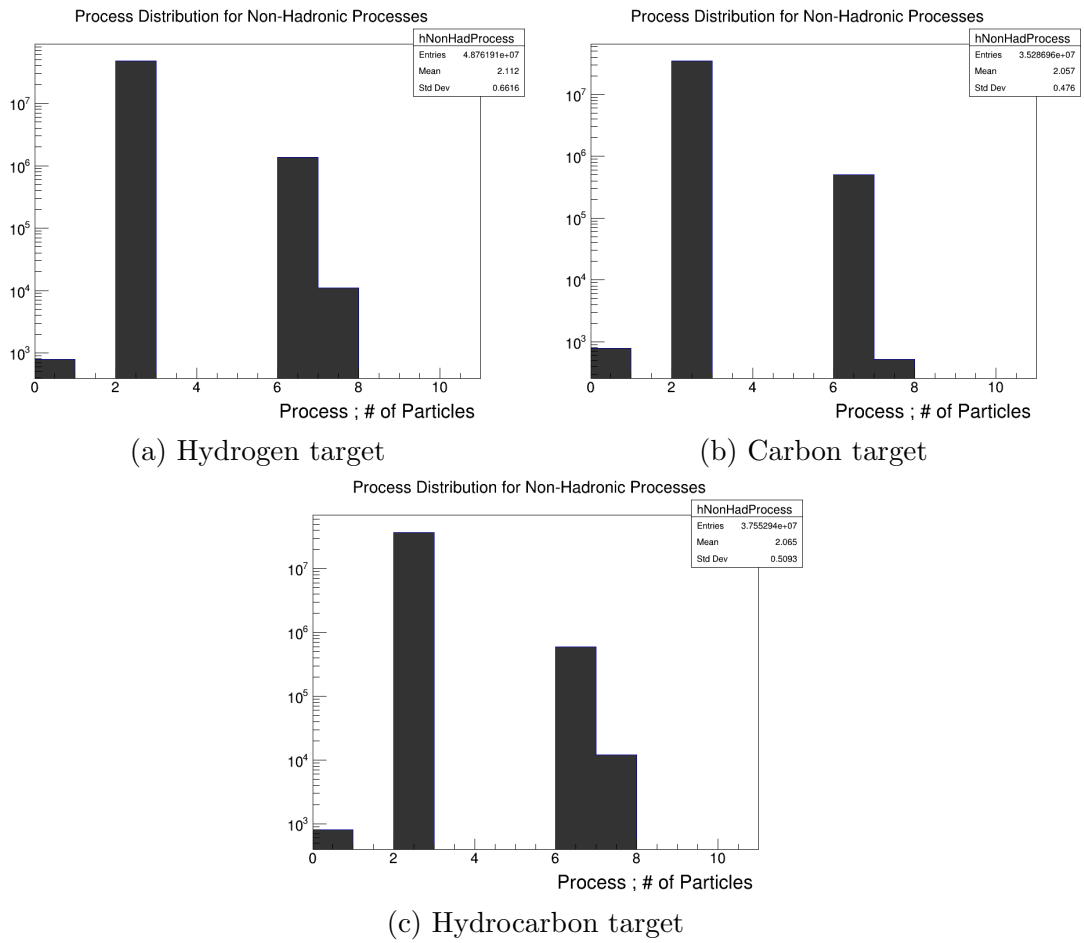


Figure C.1. Number of non-hadronic first neutron interactions on different targets, presented on a log scale for better visual clarity.

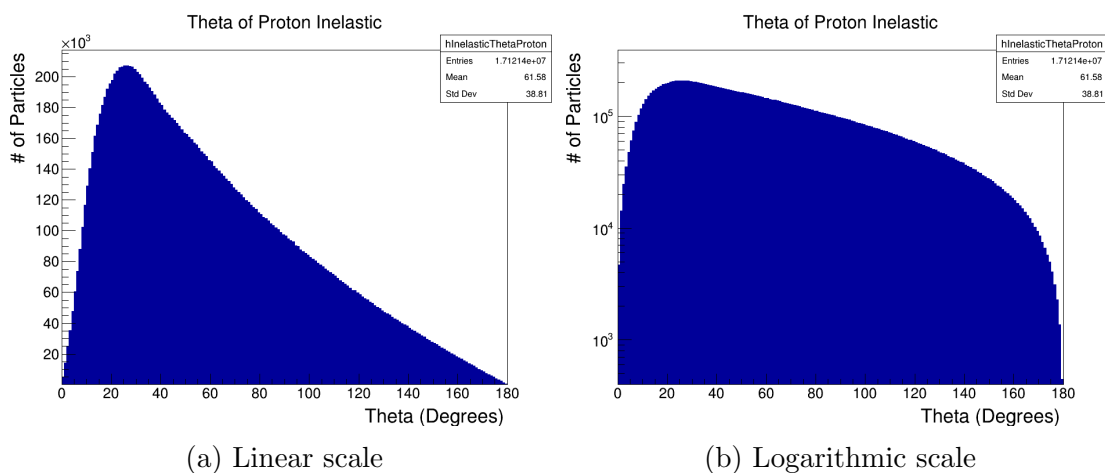


Figure C.2.  $\theta$  of outgoing protons from neutron inelastic scattering off a carbon target.

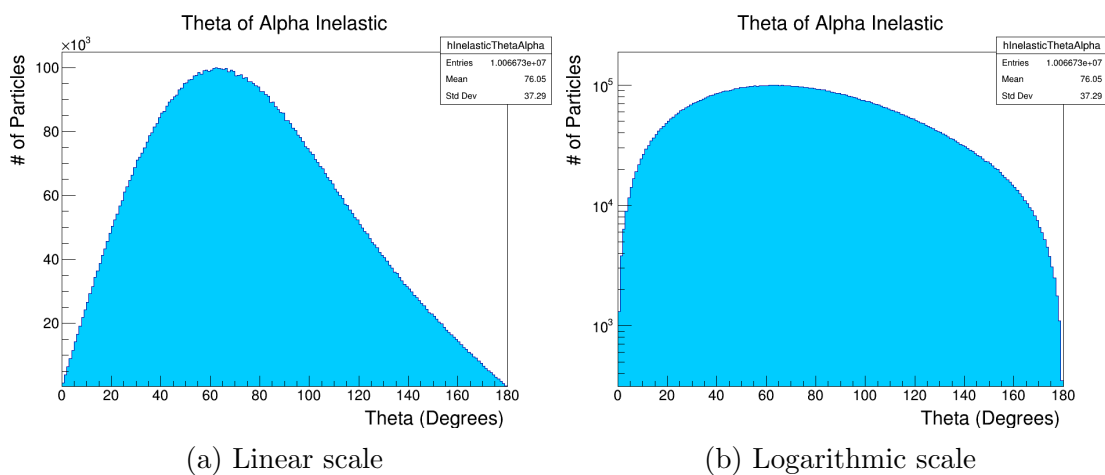


Figure C.3.  $\theta$  of outgoing  $\alpha$ 's from neutron inelastic scattering off a carbon target.

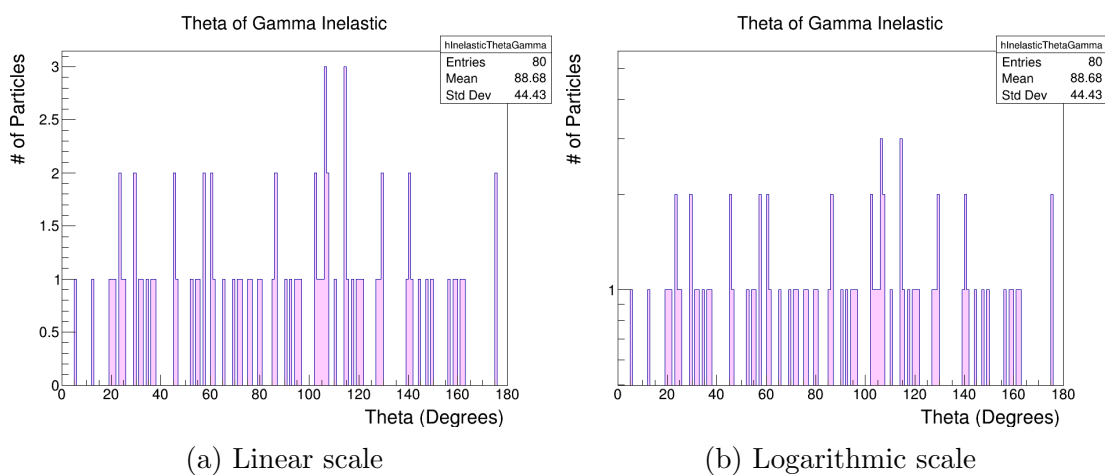


Figure C.4.  $\theta$  of outgoing  $\gamma$ 's from neutron inelastic scattering off a hydrogen target.

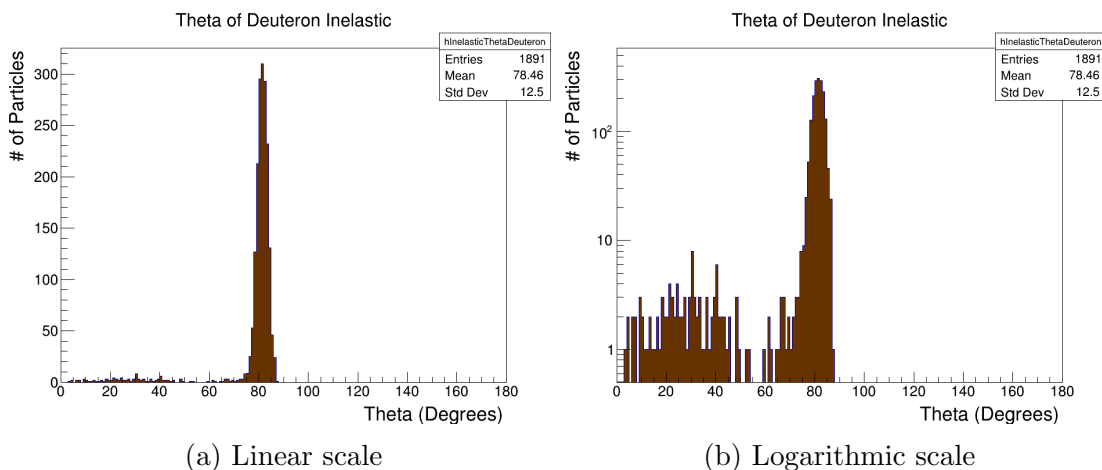


Figure C.5.  $\theta$  of outgoing deuterons from neutron inelastic scattering off a hydrogen target.

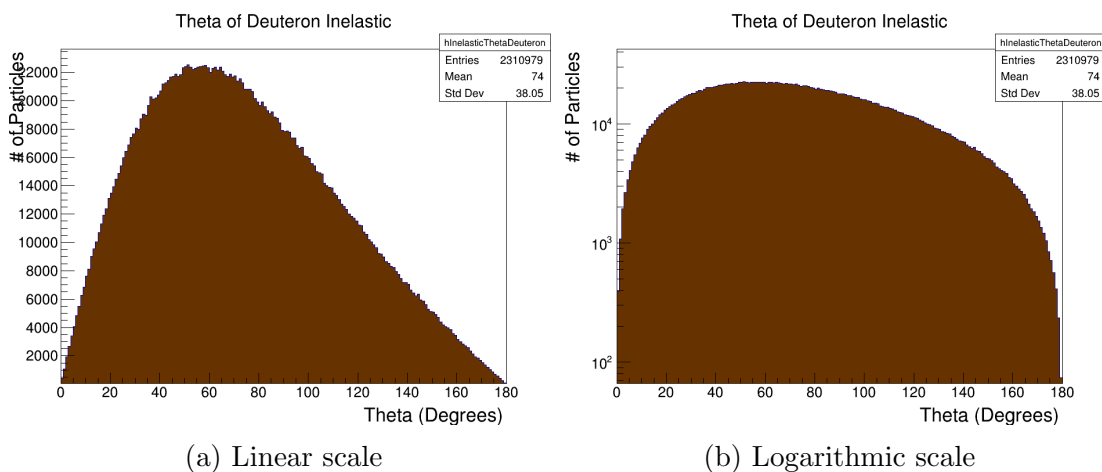


Figure C.6.  $\theta$  of outgoing deuterons from neutron inelastic scattering off a carbon target.

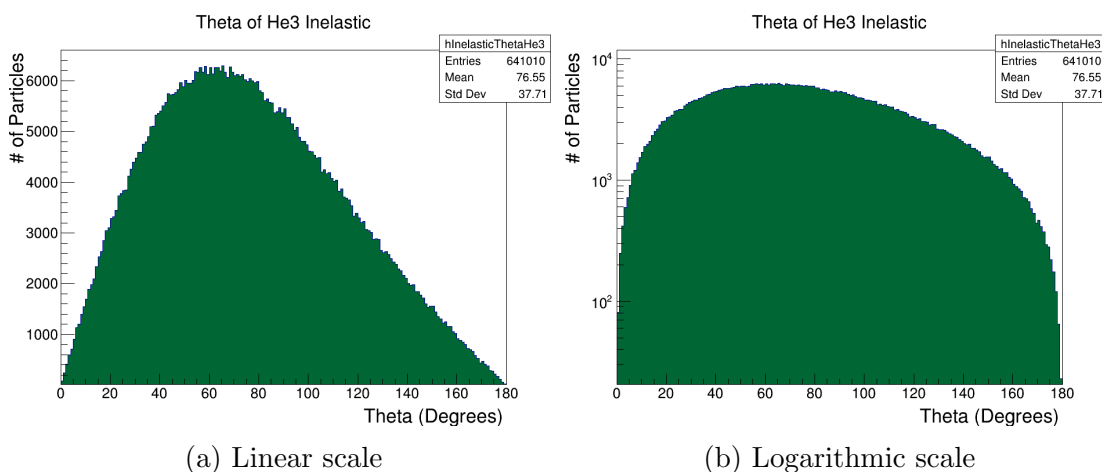


Figure C.7.  $\theta$  of outgoing  ${}^3\text{He}$ 's from neutron inelastic scattering off a carbon target

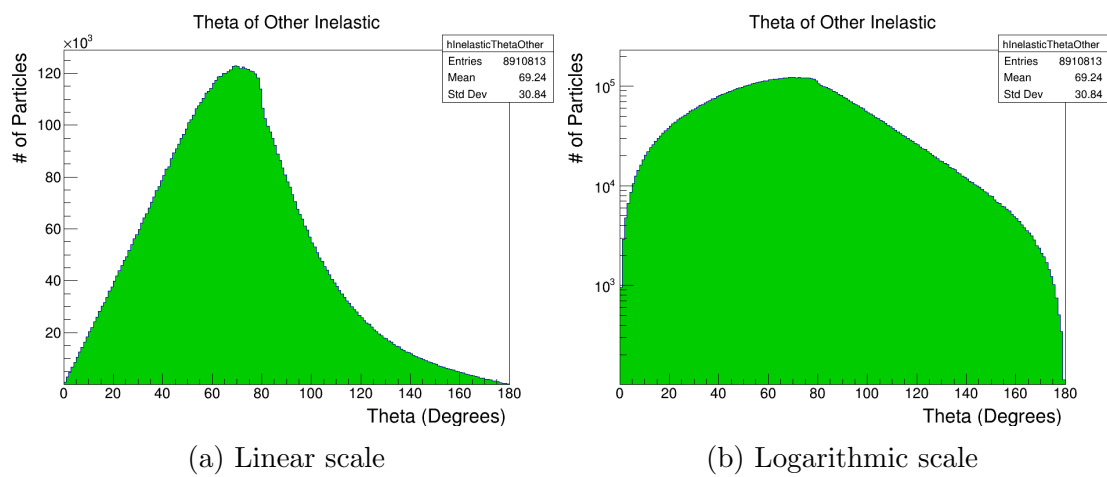
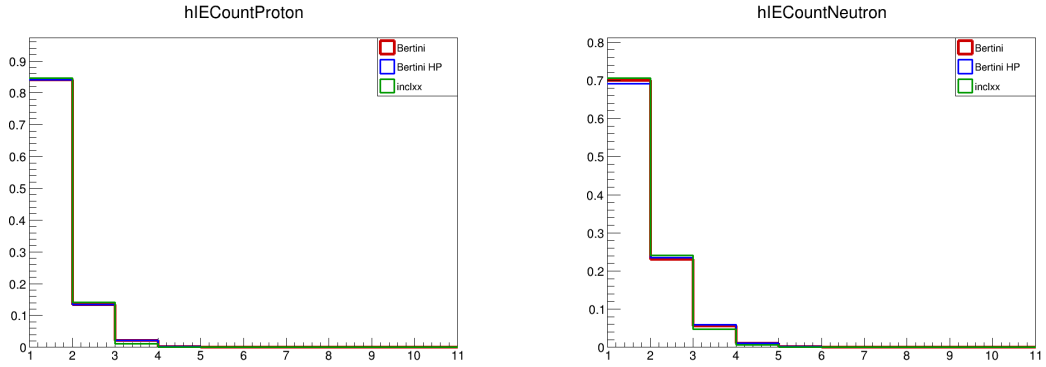


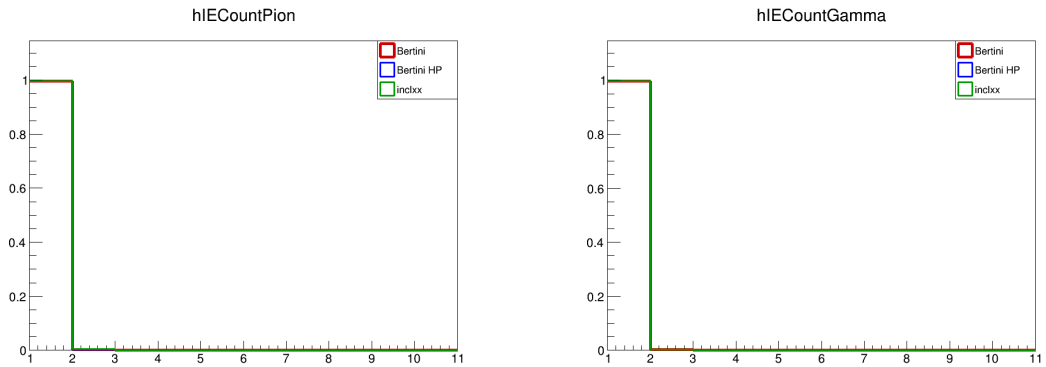
Figure C.8.  $\theta$  of outgoing others from neutron inelastic scattering off a carbon target.





(a) Multiplicity (number of particles per event) of outgoing protons from inelastic scattering.

(b) Multiplicity (number of particles per event) of outgoing neutrons from inelastic scattering.



(c) Multiplicity (number of particles per event) of outgoing  $\pi^\pm$ 's from inelastic scattering.

(d) Multiplicity (number of particles per event) of outgoing  $\gamma$  from inelastic scattering.

Figure C.9. Comparison distributions for the count (number of particles per event) distributions of outgoing particles generated from inelastic collisions. Each line colour represents data produced by a different physics list. The histograms in these plots have been area normalized. The top right plot shows the data for outgoing neutrons, while the top left plot shows data for the outgoing protons. The bottom left plot shows the data for outgoing  $\pi^\pm$ 's and the bottom right plot shows the data for outgoing  $\gamma$ 's

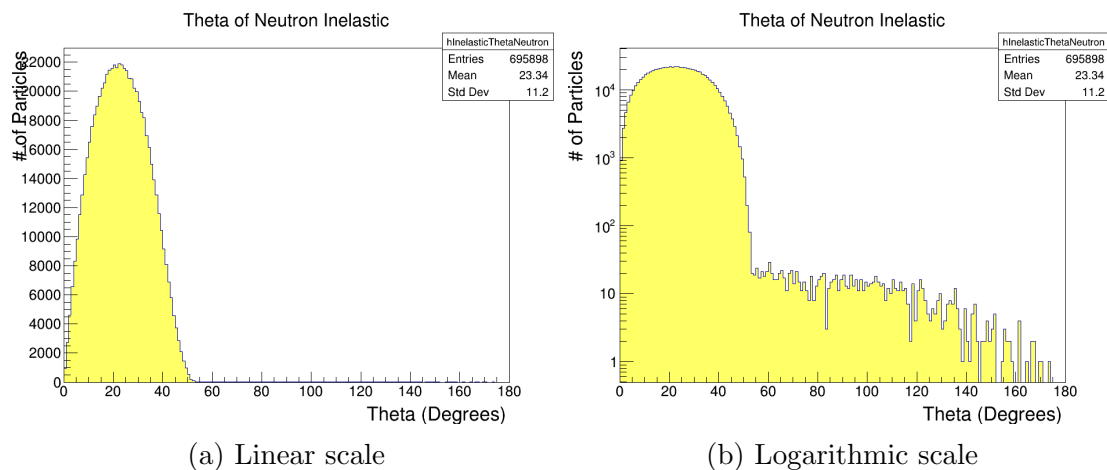


Figure C.10.  $\theta$  of outgoing neutrons from neutron inelastic scattering off a hydrogen target.

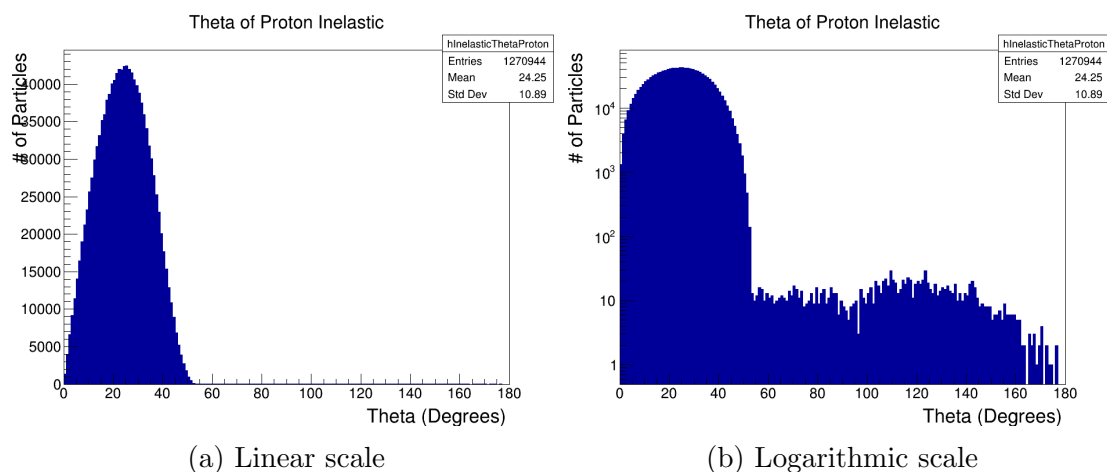


Figure C.11.  $\theta$  of outgoing protons from neutron inelastic scattering off a hydrogen target.

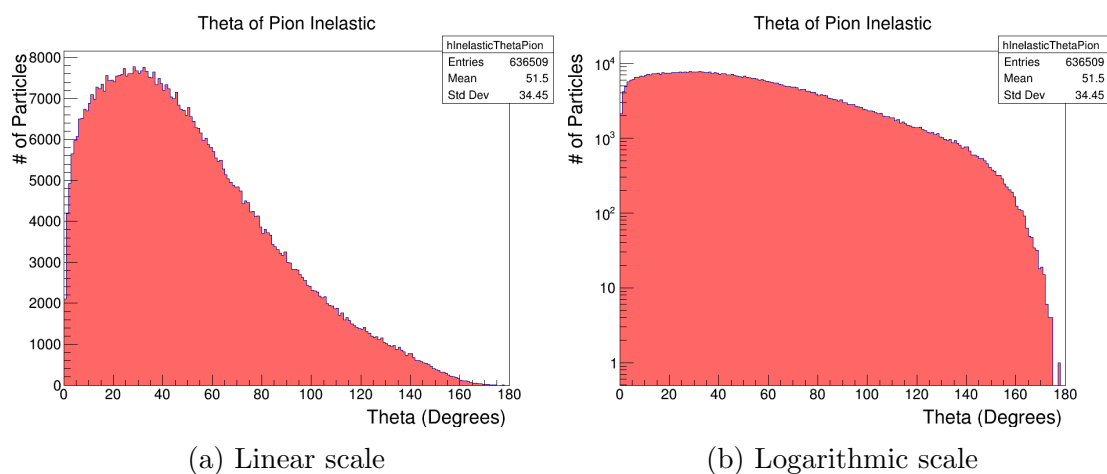


Figure C.12.  $\theta$  of outgoing  $\pi^\pm$ 's from neutron inelastic scattering off a hydrogen target.

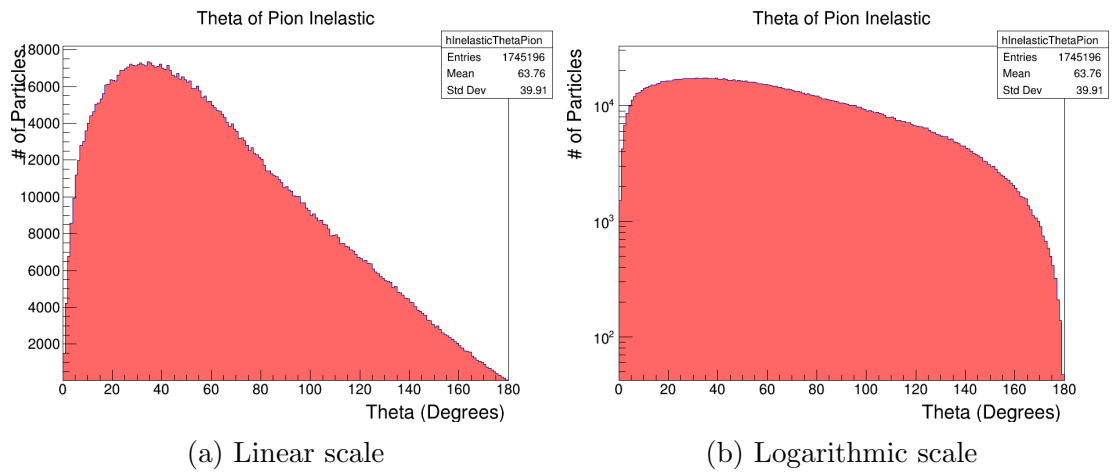


Figure C.13.  $\theta$  of outgoing  $\pi^\pm$ 's from neutron inelastic scattering off a carbon target.

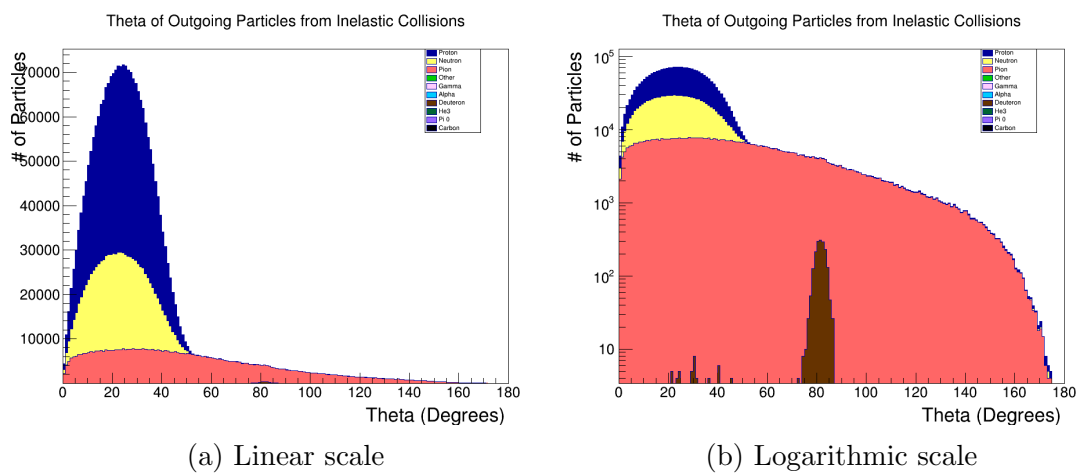


Figure C.14. Angle relative to beamline ( $\theta$ ) of outgoing neutrons from inelastic scattering of neutrons on a hydrogen target.

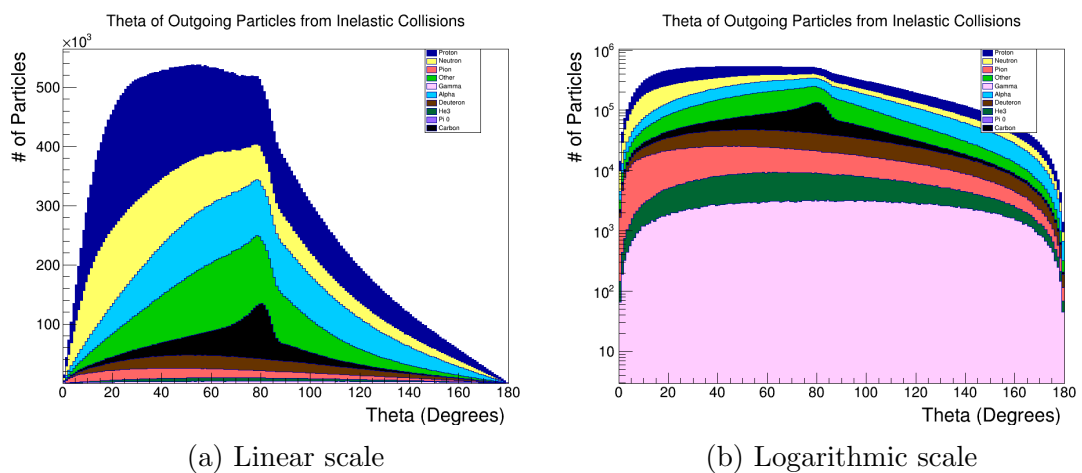
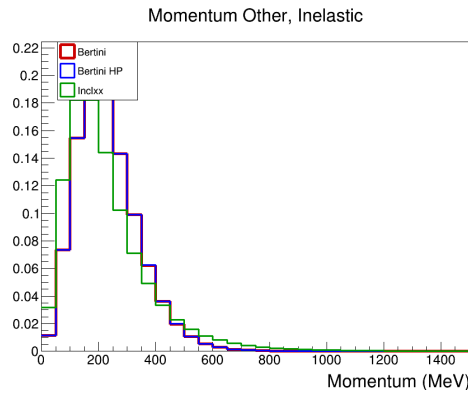
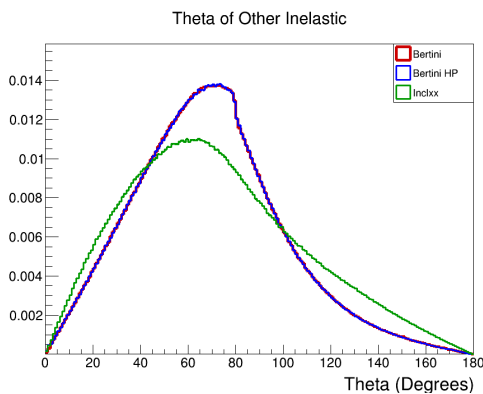


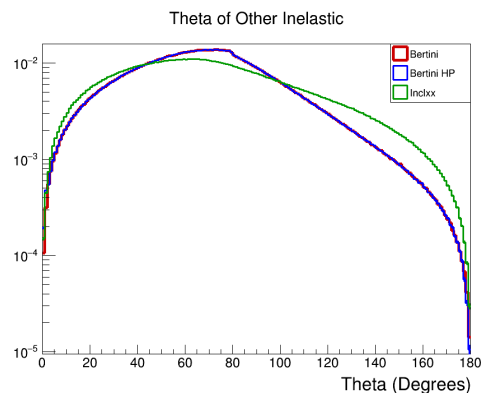
Figure C.15. Angle relative to beamline ( $\theta$ ) of outgoing neutrons from inelastic scattering of neutrons on a carbon target.



(a) Momentum of outgoing Others from inelastic scattering.

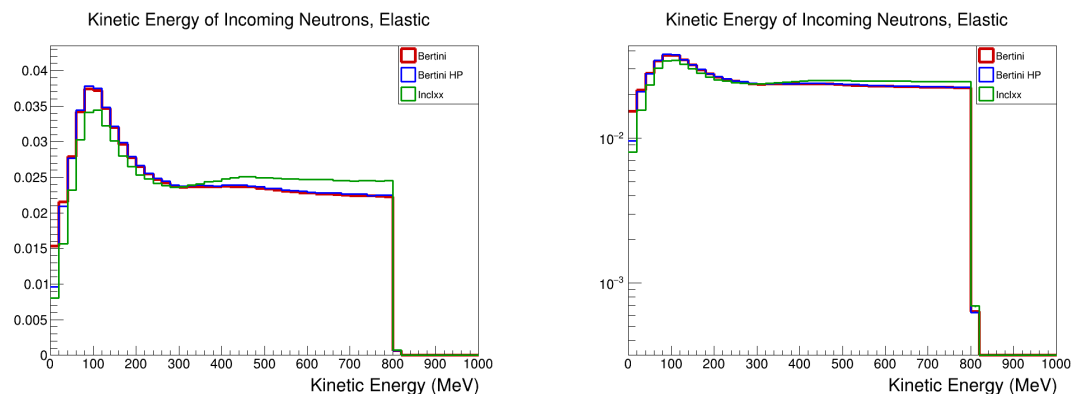


(b)  $\theta$  of outgoing Others from inelastic scattering, linear scale.



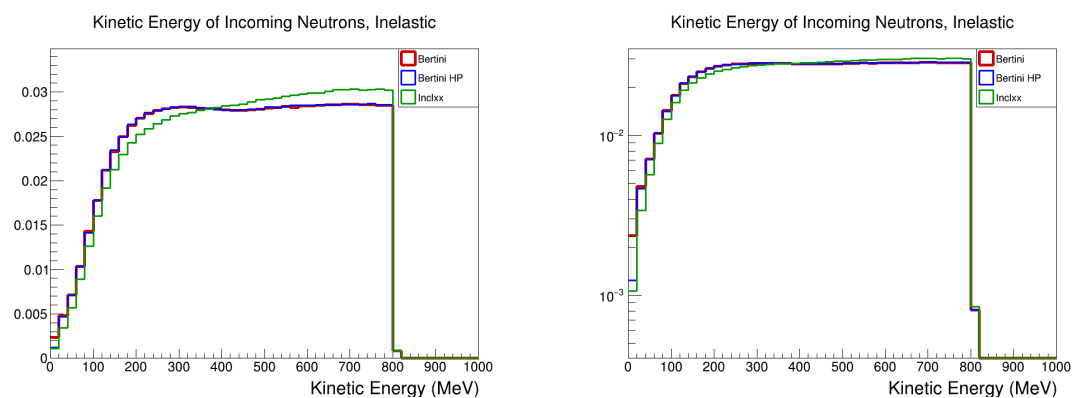
(c)  $\theta$  of outgoing Others from inelastic scattering, logarithmic scale.

Figure C.16. Comparison distributions for the kinematics of outgoing others generated from inelastic collisions. Each line colour represents data produced by a different physics list. The histograms in these plots have been area normalized. The bottom right plot shows the data from the bottom left plot on a logarithmic y-axis scale. The top plot shows the momentum distributions.



(a) Incoming energy of incoming neutrons that interact elastically with CH, linear scale.

(b) Incoming energy of incoming neutrons that interact elastically with CH, logarithmic scale.



(c) Incoming energy of incoming neutrons that interact inelastically with CH, linear scale.

(d) Incoming energy of incoming neutrons that interact inelastically with CH, logarithmic scale.

Figure C.17. Comparison distributions for the energy of incoming neutrons which interact hadronically with CH. Each line colour represents data produced by a different physics list. The histograms in these plots have been area normalized. The left column shows a linear scale, and the right column shows a logarithmic scale. The top row shows neutrons which elastically interact with CH and the bottom row shows neutrons which inelastically interact with CH.

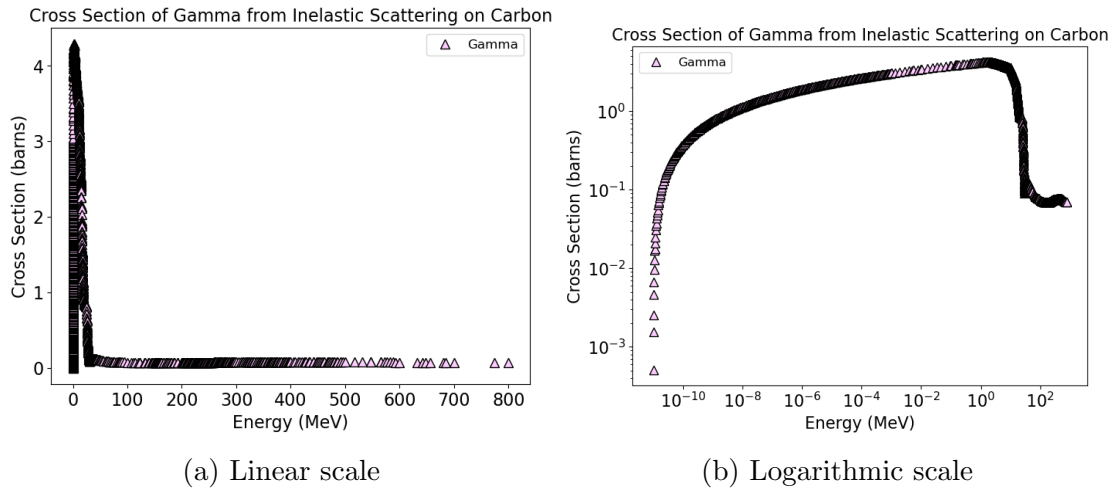


Figure C.18. Cross section as a function of kinetic energy for incoming neutrons producing outgoing  $\gamma$ 's from inelastic scattering on carbon.

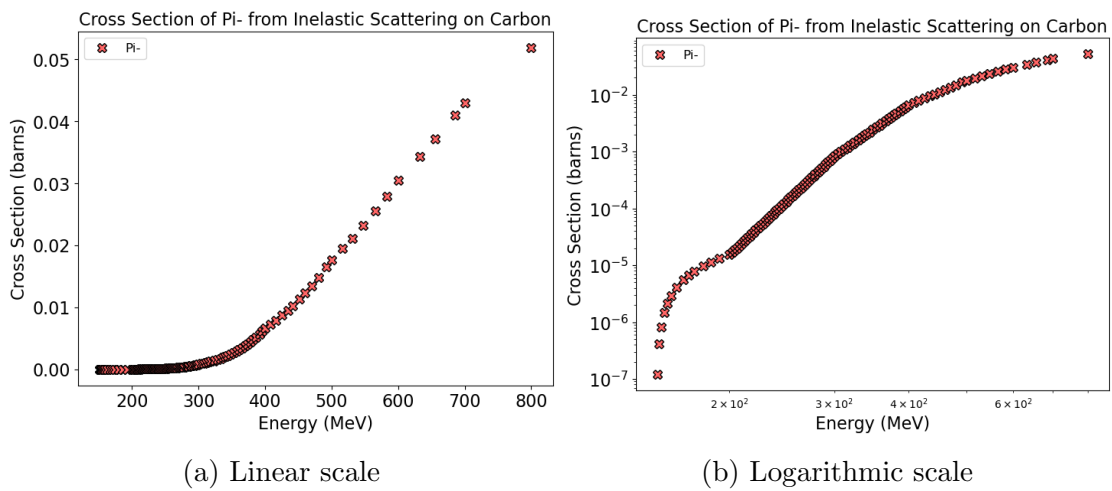


Figure C.19. Cross section as a function of kinetic energy for incoming neutrons producing outgoing  $\pi^-$ 's from inelastic scattering on carbon.

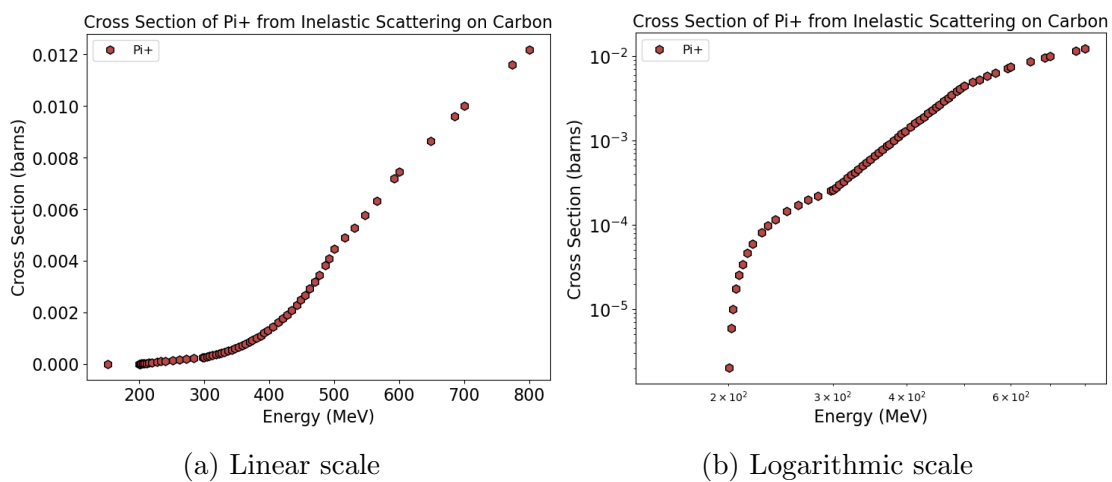


Figure C.20. Cross section as a function of kinetic energy for incoming neutrons producing outgoing  $\pi^+$ 's from inelastic scattering on carbon.

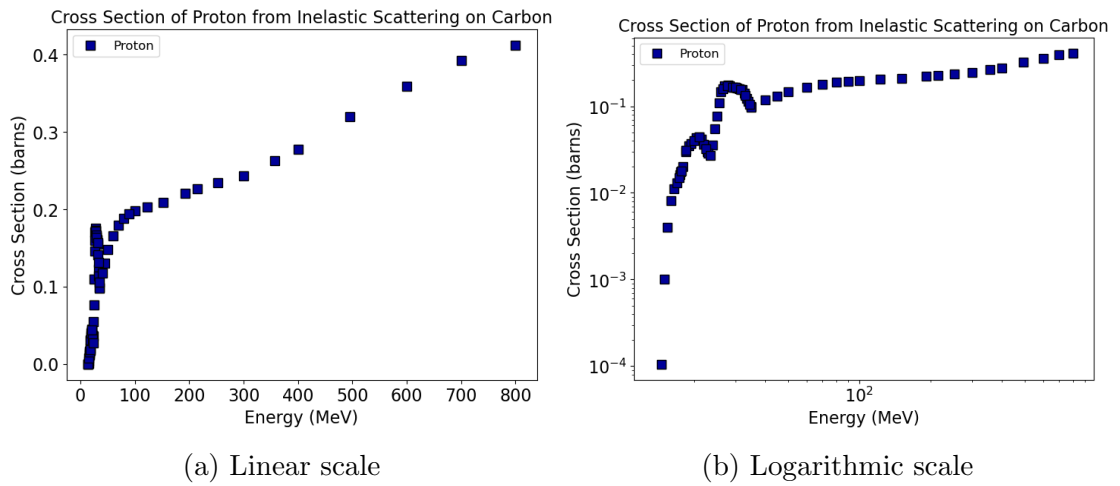


Figure C.21. Cross section as a function of kinetic energy for incoming neutrons producing outgoing protons from inelastic scattering on carbon.

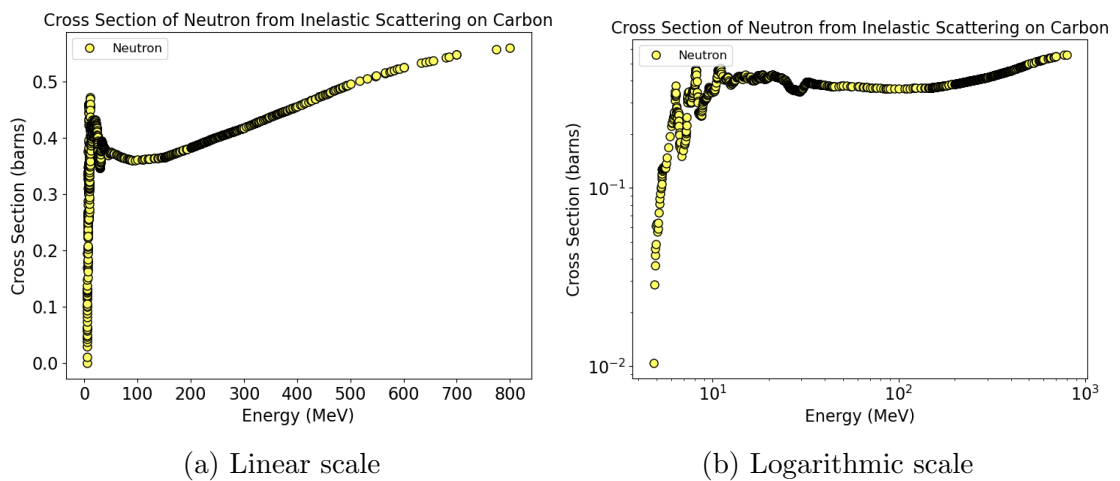


Figure C.22. Cross section as a function of kinetic energy for incoming neutrons producing outgoing neutrons from inelastic scattering on carbon.

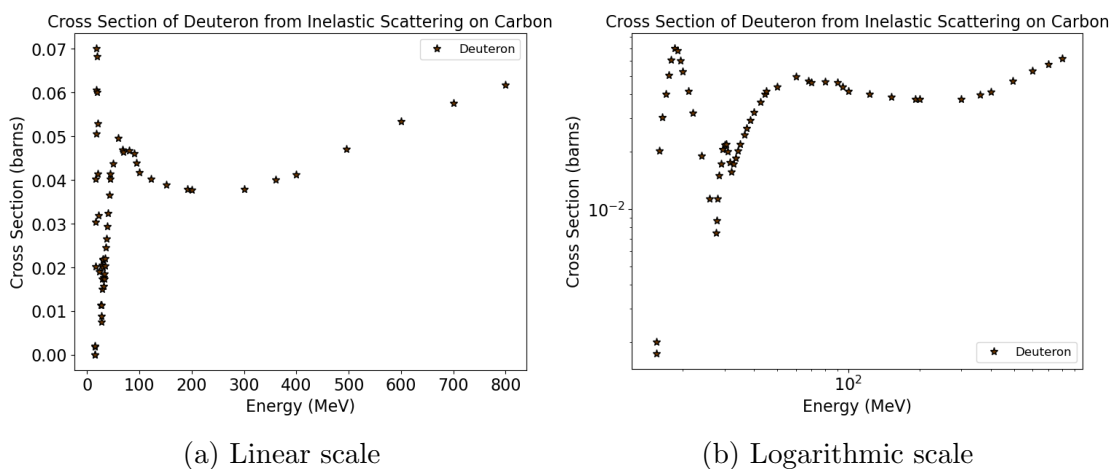


Figure C.23. Cross section as a function of kinetic energy for incoming neutrons producing outgoing deuterons from inelastic scattering on carbon.

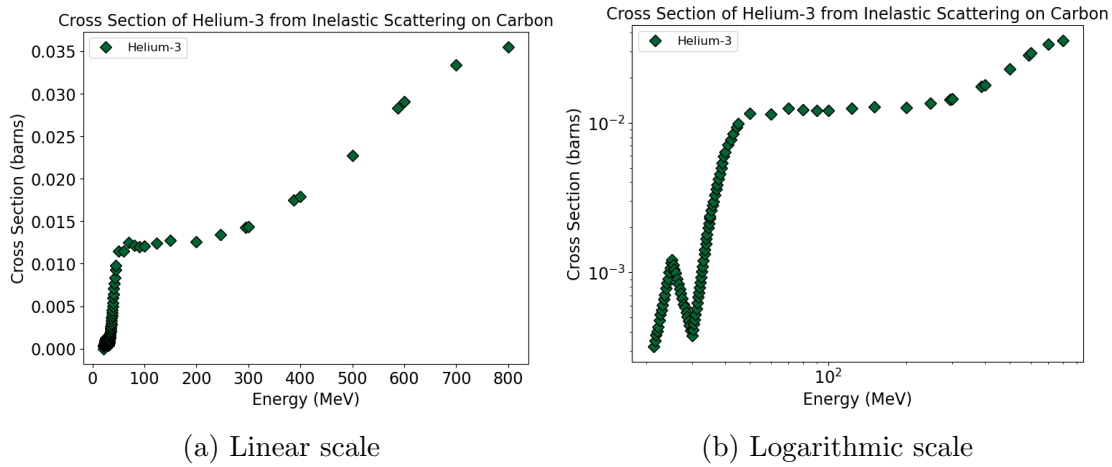


Figure C.24. Cross section as a function of kinetic energy for incoming neutrons producing outgoing  $^3\text{He}$ 's from inelastic scattering on carbon.

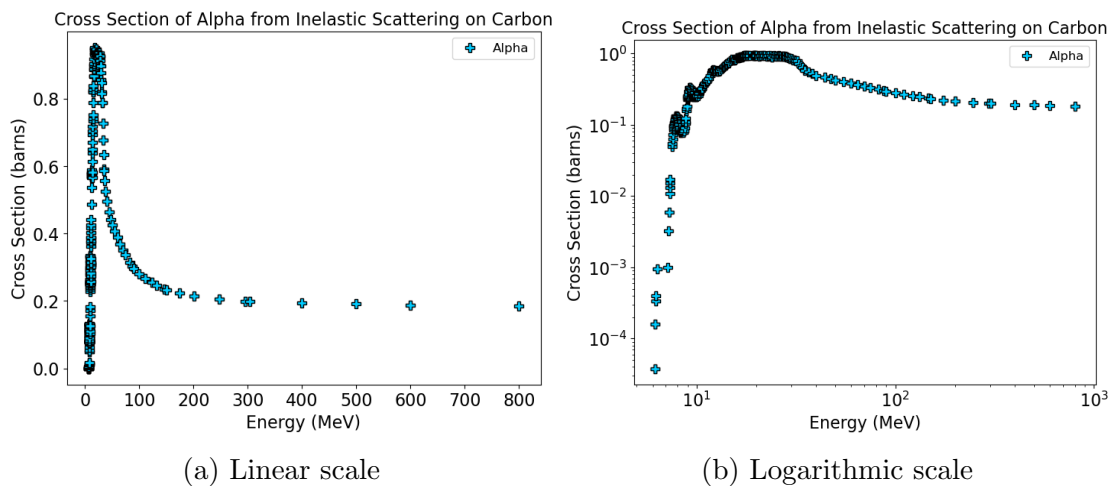


Figure C.25. Cross section as a function of kinetic energy for incoming neutrons producing outgoing  $\alpha$ 's from inelastic scattering on carbon.



# Bibliography

- [1] K. Abe et al. The T2K Experiment. *Nucl. Instrum. Meth. A*, 659:106–135, 2011.
- [2] Y. Fukuda et al. The Super-Kamiokande detector. *Nucl. Instrum. Meth. A*, 501:418–462, 2003.
- [3] A. Agarwal et al. Total neutron cross-section measurement on CH with a novel 3D-projection scintillator detector. *Phys. Lett. B*, 840:137843, 2023.
- [4] MICHAEL F. L’ANNUNZIATA. 1 - nuclear radiation, its interaction with matter and radioisotope decay. In Michael F. L’Annunziata, editor, *Handbook of Radioactivity Analysis (Second Edition)*, pages 1–121. Academic Press, San Diego, second edition edition, 2003.
- [5] D. A. Brown et al. ENDF/B-VIII.0: The 8th Major Release of the Nuclear Reaction Data Library with CIELO-project Cross Sections, New Standards and Thermal Scattering Data. *Nucl. Data Sheets*, 148:1–142, 2018.
- [6] Reference physics lists. <https://geant4.web.cern.ch/node/155>.
- [7] Zbigniew Jakubowski and Michael Kobel. A verified upgrade of the gheisha 67 simulation of particle interactions. *Nuclear Instruments and Methods in Physics Research Section A: Accelerators, Spectrometers, Detectors and Associated Equipment*, 297(1):60–86, 1990.
- [8] John Allison et al. Geant4 developments and applications. *IEEE Trans. Nucl. Sci.*, 53:270, 2006.
- [9] S. Agostinelli et al. GEANT4—a simulation toolkit. *Nucl. Instrum. Meth. A*, 506:250–303, 2003.
- [10] D.H. Wright and M.H. Kelsey. The geant4 bertini cascade. *Nuclear Instruments and Methods in Physics Research Section A: Accelerators, Spectrometers, Detectors and Associated Equipment*, 804:175–188, 2015.
- [11] All geant releases. <https://geant4.web.cern.ch/download/all>.
- [12] A Heikkinen, A Boudard, P Kaitaniemi, and G Folger. A Geant4 physics list for spallation and related nuclear physics applications based on INCL and ABLA models. *J. Phys.: Conf. Ser.*, 219:032043, 2010.
- [13] edep-sim : An energy deposition simulation. <https://github.com/ClarkMcGrew/edep-sim>.

- 
- [14] Geant4 file list. <https://apc.u-paris.fr/~franco/g4doxy/html/files.html>.
- [15] Monte carlo particle numbering scheme. <https://pdg.lbl.gov/2020/reviews/rpp2020-rev-monte-carlo-numbering.pdf>.
- [16] Neutron geant4 simulation analysis. <https://gitlab.com/neutron-lanltb-analysis/neutrong4simulationanalysis>.
- [17] Conversion & single track selection scripts. [https://git.t2k.org/sfgd\\_tools/sfgd\\_framework](https://git.t2k.org/sfgd_tools/sfgd_framework).

